NTNU
Norwegian University of
Science and Technology

Studying the chemistry of complex transition metal systems

A spectroscopic investigation of the interplay between Dy and MoS_2

Stian Ruud Schikora

Nanotechnology
Submission date: June 2017
Supervisor: Justin Wells, IFY

Norwegian University of Science and Technology
Department of Physics

“Everything we call real is made of things that cannot be regarded as real.”

Niels Bohr

Preface

This thesis is the conclusion of a five year Master of Science degree in Nanotechnology at the Norwegian University of Science and Technology (NTNU). This work is submitted as a continuation of the author's previous work in his specialisation project. The experimental work presented in this thesis was carried out in the spring semester of 2017. Experiments were conducted both at the ISA facility at Århus University, Denmark, and at Justin Wells' XPS laboratory at NTNU.

Acknowledgements

Obtaining these results was not possible by the author's work alone, and several people have contributed to the production of this thesis. I would very much like to thank my supervisor, Associate professor Justin Wells at the department of Physics. His thoughts and insights have been of great importance during data analysis and have allowed me to develop a deeper understanding in the field of condensed matter physics. Secondly, Dr. Simon Cooil has been of tremendous help performing the experiments, providing tools for data analysis and helping me understand the physical principles behind the techniques used. Additionally I would also like to thank Magnus Christiansen, Alex Schenk and Adam Götz for their valuable assistance at the NTNU lab and/or the synchrotron in Århus.

Lastly I would like to thank my friends and family for their continued support during my years at NTNU. Also, my better half, Eirin Brenna Løvheim, I could not have gone through this whitout you.

Stian Ruud Schikora
June 2017
Trondheim

Abstract

In this thesis, the interactions between MoS_2 and dysprosium have been investigated by spectroscopic and diffractive techniques. As the experimental research on dysprosium compounds is scarce, the possible applications of these could be many. Depending on the stoichiometry of the compound, it may contribute in fields such as spintronics, magneto-optics or as a semiconducting material.

Preliminary studies to introduce dysprosium as a magnetic dopant in the van der Waals gaps of the molybdenum disulphide bilayer structure revealed an interesting chemical reaction between the two compounds. As this was worth further investigation, the interplay between MoS_2 and the f-block element, dysprosium, has been investigated *in situ* by the means of X-ray photoelectron spectroscopy (XPS), low energy electron diffraction (LEED) and angle resolved photoemission spectroscopy (ARPES).

Results indicate the formation of dysprosium sulphide thin films by sulphur extraction from the MoS_2 when annealing the samples to $300^\circ\mathrm{C}$. For sufficiently thin samples in the range of 2-3 monolayers this reaction is observed to occur even at room temperature, and further propagated by heating. Using a finite element model, the layered stoichiometry of the dysprosium sulphide was extracted. In combination with the observed diffraction patterns from LEED, this supports the formation of a possible mono- or disulphide, differing from the most stable bulk formation of Dy_2S_3. Studying the electronic structure by ARPES showed a decrease of the valence band maximum of MoS_2 at the $\bar{M}$-point by 130 meV.

Oxidation experiments of the deposited dysprosium overlayer displayed different attributes dependent on whether the film had been heated before oxygen exposure or not. A film that had mildly reacted with the MoS_2 substrate showed characteristics similar to that of the sesquioxide with insulating properties, but could also be other possible oxidation states. If the overlayer was annealed to $300^\circ\mathrm{C}$ prior to oxygen exposure reactions suggesting the formation of a dysprosium oxide sulphide was observed.

The results from this work should provide a good foundation for further studies of the synthesis of dysprosium oxide and sulphide thin films. Additionally, the calculated value of the spin splitting of the Dy5p-orbital of $5.67 \pm 0.1\mathrm{eV}$ should be useful as reference for further spectroscopic studies of this material.

Sammendrag

I dette prosjektet har interaksjonene mellom MoS_2 og dysprosium blitt undersøkt ved hjelp av spektroskopi- og diffraksjonsteknikker. Ettersom det er begrenset med forskning på dysprosiumforbindelser, er applikasjonene uante. Forbindelsene foreslås å ha potensiale innen felter som spinntronikk, magneto-optikk, og som halvleder, avhengig av støkiometri.

Under tidligere forsøk på å introdusere dysprosium i van der Waals gapet i MoS_2, ble det observert en kjemisk reaksjon mellom de to forbindelsene. For å undersøke dette videre har interaksjonen mellom MoS_2 og f-blokk elementet, dysprosium, blitt analysert *in situ* ved hjelp av røntgen fotoemisjonspektroskopi (XPS), lav energi elektrondiffraksjon (LEED) og vinkeloppløst fotoemisjonspektroskopi (ARPES).

Resultatene indikerer dannelsen av dysprosiumsulfid gjennom ekstraksjon av svovel fra MoS_2 ved oppvarming til $300°\mathrm{C}$. For prøver av 2-3 monolags tykkelse er denne reaksjonen observert selv ved romtemperatur. Videre har bruk av en flerlagsmodell tillatt å modellere den lagvise støkiometrien til dysprosiumsulfidet. Sett sammen med det observerte diffraksjonsmønsteret i LEED er dannelsen av et mulig mono- eller disulfid støttet, i motsetning til den mest stabile "bulk fasen", Dy_2S_3. Ved å studere båndstrukturen gjennom ARPES ble det observert en negativ endring av valensbåndets maksima i $\bar{M}$-punktet, på 130 meV.

Under oksidasjonseksperimenter av dysprosiumlaget ble det observert forskjellige reaksjoner avhengig av om filmen var blitt varmet opp før oksygeneksponering, eller ikke. En tynnfilm som hadde gjennomgått en mild reaksjon med MoS_2-substratet, viste egenskaper som ligner sesquioxidets, men kan også være andre mulige oksidasjonstilstander. Hvis dysprosiumlaget ble varmet opp til $300°\mathrm{C}$ før eksponering av oksygen, ble det observert en reaksjon som antyder dannelsen av dysprosiumsulfid.

Resultatene fra dette arbeidet gir et stabilt fundament for videre forskning på syntese av dysprosiumoksid- og dysprosiumsulfid tynnfilmer. I tilleg vil den kalkulerte verdien av spin splittingen av Dy5p orbitalen på $5.67 \pm 0.1\mathrm{eV}$ være en nyttig referanse i fremtidige spektroskopiske studier av dette materialet.

Table of Contents

List of Tables

List of Figures

Abbreviations

AFM	Atomic force microscopy
ARPES	Angle resolved photoemission spectroscopy
ARXPS	Angle resolved X-ray photoelectron spectroscopy
FWHM	Full width at half maximum
IMFP	Inelastic mean free path
LEED	Low energy electron diffraction
PES	Photoelectron spectroscopy
PVW	Pseudo-voigt width
RHEED	Reflection high-energy electron diffraction
SEM	Scanning electron microscopy
SOC	Spin-orbit coupling
STM	Scanning tunneling microscopy
UHV	Ultrahigh vacuum
UPS	Ultraviolet photoelectron spectroscopy
VBM	Valence band maximum
XPS	X-ray photoelectron spectroscopy

Chapter 1

Introduction

Background & Motivation

The chemistry of the lanthanide and actinide elements still remains as one of the last great frontiers of the periodic table. The scope of potential applications of the various compounds could be primed for rapid expansion when these systems are further understood. Amongst the rare earth elements, the atom number 66, dysprosium, has been subject to particular interest due to its interesting magnetic properties which might prove useful as a magnetic insulator in one of its many possible oxide forms, or as an addition to the family of inner transition metal dichalcogenides. Thus, this thesis aims to expand the the understanding of such complex transition metal systems.

This thesis is a continuation of the work performed in the author's specialisation project. Previous experiments meant to introduce magnetic properties in MoS_2 by doping of dysprosium revealed interesting chemistry between the two compounds. It was hypothesized that this f-block element reacts chemically with the sulphur in the underlying substrate, thus forming a dysprosium sulphide with an unknown stoichiometric composition. From the chemistry and physical properties of dysprosium it is known that its most stable sulphide is the dysprosium sequisulfide (Dy_2S_3). Still, previous experiments have indicated the formation of a different composition. The lanthanide sulfides have attracted considerable interest as they have potential applications as solar energy conversion materials, infrared window materials and phosphor host media. However, the difficulty of controlled synthesis, as well as the increased complexity in theoretical modeling due to the nature of f-shell electrons, has limited the applications of the rare earth elements.

As stated, the rare earth elements are yet to be fully understood, hence the possibilities of these materials could be many. For instance, Von Welsbach and Robert Bunsen were

responsible of discovering that the alloy formed from Fe and Ln was pyrophoric, emitting sparks when scratched. This alloy has later been used for lighter flints [1]. The lanthanide oxides have also attracted much interest from both industry and academia for their use in catalytic applications, due to their numerous oxidation states. The more rare and less stable conformations of rare earth oxides and sulphides have also proven to exhibit interesting physics as metamagnetic transitions in $EuSe_2$ [2], and possible applications for spin filtering in graphene with interactions from europium oxide (EuO) [3].

Even though the rare earth compounds can be fascinating enough by themselves, it is also interesting to observe the interaction between such compounds and other materials. Molybdenum disulphide, which is used as the substrate in this thesis, belongs to the family of materials called transition metal dichalcogenides and exhibit peculiar spin physics as a 2D-material due to the local breaking of inversion symmetry. This material has shown to be a promising candidate for future electronic circuits [4]. The way the addition of dysprosium as a magnetic compound interacts with the MoS_2 may lead to even more interesting properties. For instance, the addition of manganese in 1D TaS_2 has shown to induce low temperature magnetic phase transitions [5], while Ni-doping has proved to increase the superconducting critical temperature in the same material [6].

Experimental Approach

The study of the chemical reaction between MoS_2 and Dy has been conducted at the University of Århus at the MATLINE synchrotron beamline for material science, as well as Justin Wells' laboratory at NTNU. Surface growth, band structure changes and the effects of annealing were studied by means of LEED, XPS, ARXPS and ARPES. Modeling the layered stoichiometry of the resulting compound was done by ARXPS and a layer model presented in chapter 3. LEED was used to determine the crystal quality and to observe if there was any change in the crystal structures, as well as to determine the crystal orientation for band structure measurements by ARPES.

Report Structure

This thesis is divided into seven main chapters. The first chapter contains an introduction to the subject as well as the motivation for the research. Chapter 2 includes the background and basic theoretical aspects regarding the materials. In chapter 3 the experimental techniques XPS, ARPES and LEED will be presented as well as important aspects regarding these. As this thesis is based on previous work in the author's specialisation project, chapters 2 and 3 will contain parts similar to this. How the experiments were performed at the different sites is presented in chapter 4, and in chapter 5 and 6 the results are displayed accompanied by a discussion and interpretation of these. Lastly, in chapter 7 a summary and conclusion is presented along with suggestions of further work.

Chapter 2

Theory

In this chapter, details regarding the substrate material will be presented, as its properties and crystal structure are relevant for understanding the experiments performed. Additionally, the principles on how a spin polarized band structure occurs, and how introducing magnetic fields may influence these, are included in this chapter. Lastly, a brief section discussing crystal growth modes and the theory behind intercalation is presented.

SECTION 2.1 MoS_2

Molybdenum disulfide is an inorganic compound that can form natural crystals of three different polymorphs; 1T, 2H and 3R [7], where the 2H form is the most abundant in nature and the material studied in this report. The HCP crystal structure of MoS_2 and its reciprocal lattice is shown in figure 2.1. We see from the figure that the unit cell has an in-plane lattice constant $a = 3.17$ Å. The unit cell consists of two trilayers including the van der Waals gaps, giving an out-of-plane constant $c = 2 \cdot (3.24 + 2.90)\text{Å} = 12.28$ Å. The reciprocal lattice is the Fourier transform of the real space lattice, and can be observed by electron diffraction techniques such as LEED. Figure 2.1 depicts the first Brillouin zone along with its high symmetry points. The distances between the reciprocal- and real space lattice points in a hexagonal structure are inversely related as $c^* = \frac{2\pi}{c}$ and $a^* = \frac{4\pi}{\sqrt{3}a}$. When using surface sensitive techniques, this results in the out-of-plane symmetry being broken, which in turn leads to a reduction of the brillouin zone dimensionality from 3D to 2D.

While the bonds between the Mo and S atoms are strongly covalent, the attraction between the sulphur in adjacent layers is caused by weaker van der Waals forces. Consequently, cleaving of the sample will mostly result in a sulphur terminated surface.

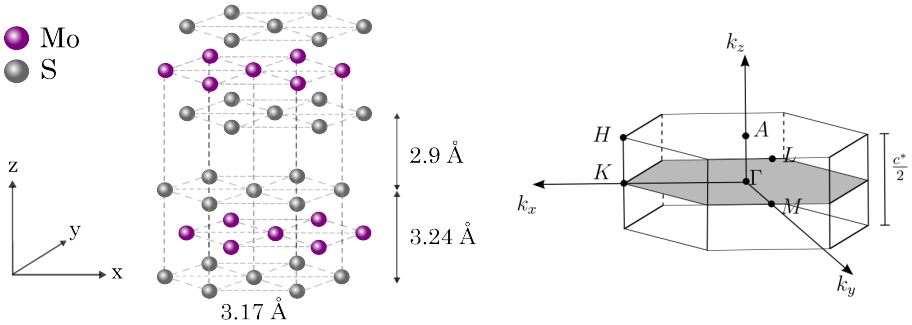

Figure 2.1: Crystal structure of MoS_2 adapted from Ref. 8 and 1st Brillouin zone of the same structure taken from Ref. 9.

SECTION 2.2 Spin Polarized Band Structures

In solids, the spin-orbit coupling makes the spin degree of freedom respond to its orbital environment. As a result, fascinating phenomena such as spin splitting of electron states in inversion-asymmetric systems can occur even at zero magnetic field [10].

In a crystalline solid, the motion of the electrons is governed by energy bands $E_n(\vec{k})$ with a band index n and a wave vector $\vec{k}$. In the presence of a magnetic field these bands may split due to the Zeeman effect, and in the presence of an electric field the bands split by the Stark effect. More intricate effects like the Rashba effect arise from asymmetry in the crystal system creating an asymmetry in the periodic potential. This can be both from bulk inversion asymmetry or structure inversion asymmetry [10].

The inversion symmetry of a system can be divided into two components; space- and time symmetry. Space symmetry in a crystal means that for every energy state E at a position $\vec{k}$ with a defined spin orientation, there will always be a counterpart at the position $-\vec{k}$. Time reversal symmetry for the same state implies that relation also holds for opposite spins, to summarize:

$$\begin{aligned} \textbf{Space inversion symmetry:} \quad & E_\uparrow(\vec{k}) = E_\uparrow(-\vec{k}) \\ \textbf{Time inversion symmetry:} \quad & E_\uparrow(\vec{k}) = E_\downarrow(-\vec{k}) \end{aligned} \tag{2.1}$$

Combinding these two then gives rise to the spin degeneracy

$$E_\uparrow(\vec{k}) = E_\downarrow(\vec{k}) \tag{2.2}$$

In systems consisting of magnetic materials, the symmetry can be broken and thus lead to splitting of the energy bands. In the case of MoS_2 the material is not magnetic, but a splitting of the energy bands can still be observed, meaning it must come from somewhere

else. In molybdenum disulphide there exists a local breaking of inversion symmetry in each layer of the material, meaning that the spin degeneracy in equation 2.2 does not hold. This makes the bands spin polarize as seen in figure 2.2. Notice that there exists a net dipole moment in each monolayer of the crystal. This means that, depending on the spin orientation, the dipole moment can increase or decrease the energy of the spin state, which is further described in section 2.3. This results in two well defined energy bands for opposite spin states. As the unit cell of MoS_2 contains two layers with opposite configuration, the resulting structure becomes spin degenerate.

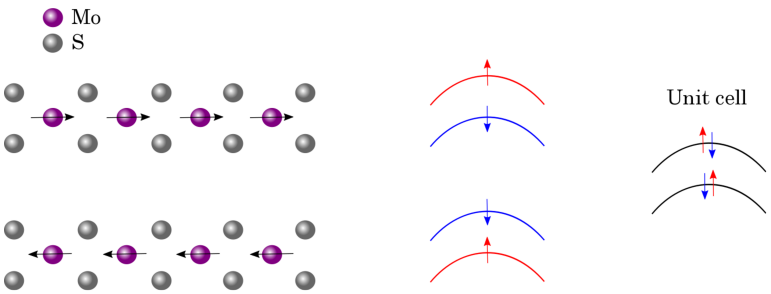

Figure 2.2: Unit cell of MoS_2 viewed from the side. Here depicting two monolayers stacked along the c-axis. Each monolayer has a net dipole moment, and if an arbitrary point in the top layer has a spin-configuration, the same point in the underlying layer has the opposite configuration. The unit cell band structure is then the average of these two, resulting in a spin degenerate bulk system.

Predicting how the bands will spin polarize involves solving the Dirac equation of the system at hand. By using a non-relativistic approximation one can derive the Pauli equation, which includes several terms to understand the system such as the Zeeman term, the Darwin term and the Pauli spin-orbit coupling term. The last one mentioned is interesting as it acts as a momemtum-dependent Zeeman energy [11]

$$\hat{H}_{SO} \sim \frac{\mu_B}{mc^2}(\vec{E} \times \vec{p}) \cdot \vec{\sigma} \tag{2.3}$$

where μ_B is the Borh magneton, m the electron mass, c the speed og light, $\vec{p}$ the electron momentum, $\vec{\sigma}$ is the vector of Pauli spin matrices and $\vec{E}$ is the electric field given by the gradient of crystal potential ($\vec{E} = -\vec{\nabla}V$).

With structural inversion symmetry broken along the direction $\vec{z}$, as it is in MoS_2, the bands are split in energy due to the Rashba effect. For a 2D system with $\vec{k} = (k_x, k_y, 0)$, this will have an electronic band dispersion according to the free electron model as

$$E(k_x, k_y) = \frac{\hbar^2}{2m_e}({k_x}^2 + {k_y}^2) + \alpha(\pm|k_x| \pm |k_y|) \tag{2.4}$$

where α is the Rashba parameter. DFT calculations of MoS_2 including spin orbit coupling can be seen in figure 2.3.

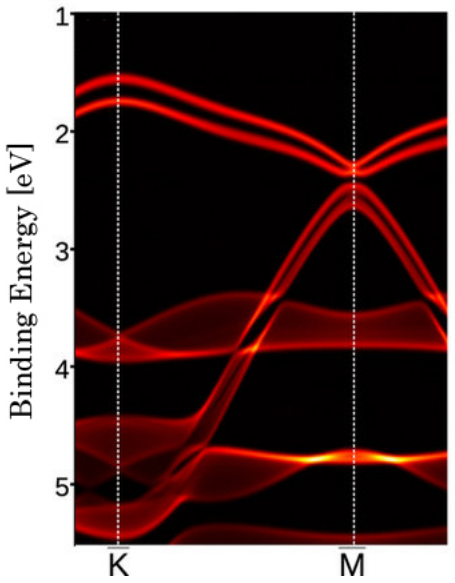

Figure 2.3: DFT band structure of 2H-MoS_2 depiting the structure between the $\bar{K}$ and $\bar{M}$ high symmetry points. Figure adapted from [12]

SECTION 2.3 Band Structure Tuning by Magnetic Fields

Introducing a magnetic field to a system will change the band structure. How the band strucure is influenced is dependent on several factors. The Zeeman effect will be able to split energy bands into spin polarized bands by breaking the time reversal symmetry of the system. Dependent on the orientation of the field it will increase the energy of one spin state and decrease the opposite state. The Zeeman magnetic interaction energy is defined as $E_Z = g^* \mu_B B$, where g^* is the effective spin g-factor, μ_B the Bohr magneton and B is the applied magnetic field. The Hamiltonian for a 2D system can be divided into two components, the in-plane component and, perpendicular component as

$$\hat{H} = \frac{g_{\|}}{2} \mu\text{–}B(B_x \sigma_x + B_y \sigma_y) + \frac{g_z}{2} \mu_B B_z \sigma_z \tag{2.5}$$

where the effective g-factors have been split into a component in the parallel direction and a component in the perpendicular direction.

How the Zeeman effect affects a system's band structure is dependent on the structure before applying a field. If a system already shows signs of a spin split band structure as for example in MoS_2, the bands with spin in the same direction as the field will have their energy increased by $\frac{g_z}{2} \mu_B B_z$ and the opposite spins will decrease by the same amount. When probing a spin degenerate system, the bands are already overlapping and an applied

magnetic field will then force these bands to split into two. In the case where parts of the band structure have spin orientation perpendicular to the applied field, these states will be unaffected.

SECTION 2.4 Thin Film Growth and Deposition Theory

2.4.1 Thin Film Growth

When depositing a thin film on a substrate, there are mainly three different growth modes possible. These are shown in figure 2.4. Which growth mode to occur on any given sample is influenced by the incoming atom flux, trapping probability, sticking coefficient and of course what is energetically most favourable.

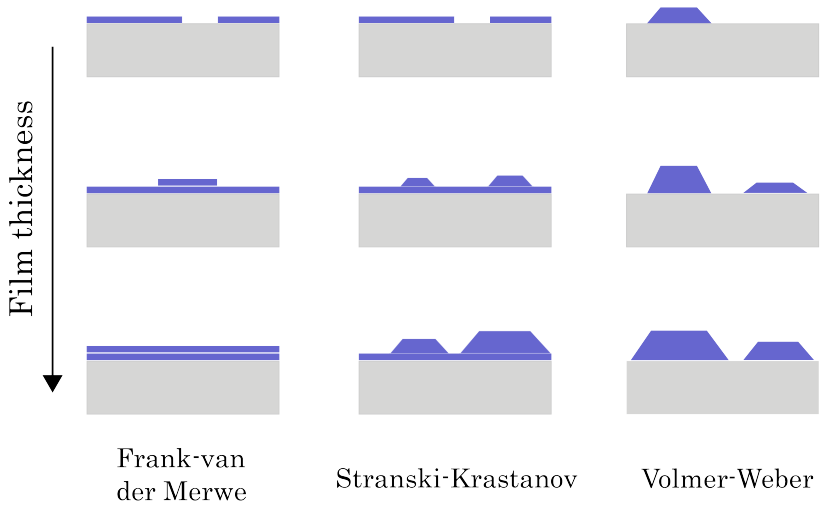

Figure 2.4: Schematic of the evolution of the three primary thin film growth modes for increasing film thickness; Frank-van der Merwe, Stranski Krastanov and Volmer-Weber.

The Frank-van der Merwe displays the characteristics of layered growth. Because the adatoms bind more strongly to the surface than to each other, this growth mode makes it possible to form complete monolayers on the surface. This growth mode is typically observed in the case of adsorbed gases [13].

The Volmer-Weber mode displays the opposite case where the adatoms rather bind to each other than to the surface. This results in small clusters nucleated onto the surface, which forms islands in the condensed phase. This mode is seen in many systems of for example metals growing on insulators [13].

The last growth mode is an intermediate case of the former two. Stranski-Krastanow displays a layer plus island growth. This can be the case when after forming a few monolayers of adsorbed material it becomes energetically unfavourable to continue this mode of growth. Depending on the deposited material, there is a number of possible explanations for the change of growth mode. Mismatch of the lattice parameters between the substrate and the bulk crystal of the deposit may cause the growth mode to change as this is not stable in the bulk formation. Symmetry of or molecuar orientation in the intermediate layer may also not be able to continue into the bulk.

2.4.2 Intercalation

Intercalation compounds can be defined as solid phases resulting from a structural change in the crystal of a solid that contains an appropriate system of accessible unoccupied lattice positions [14]. Through the course of an intercalation reaction the adatoms diffuse from the outer surface and into the bulk of the solid. These reactions proceed only at intermediate temperatures, since at higher temperature the molecular matrix of the host solid will become unstable. At low temperature, the energy barrier for diffusion of guest species in the solid will inhibit the reaction. Achieving intercalation can be done in several ways; intercalants can be added during the synthesis of the compound, introduced to the sample electrochemically or by vapour diffusion [15, 16]. In the experiments performed in this thesis, the possible intercalation happens through an annealing process where the thermal expansion of the crystal lattice might allow adatoms to intercalate into the solid's crystal structure.

Intercalation compounds can have profoundly different properties than the original solid. For instance, intercalation of tantalum in TiS_2 drastically lowers the thermal conductivity [17], and adding sodium to the FeSe structure induces high-temperature superconductivity [18].

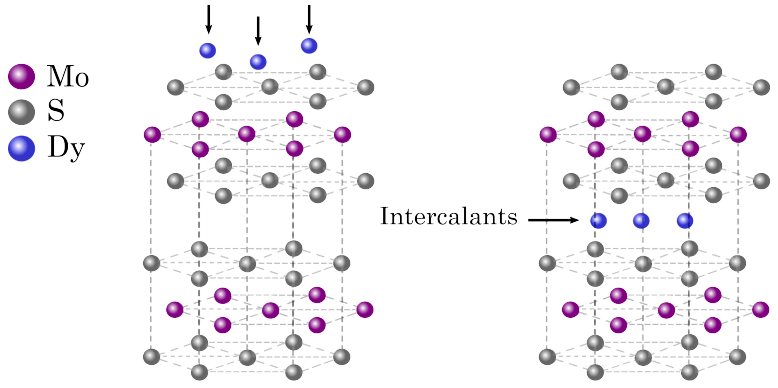

Figure 2.5: Schematic of an intercalation process. Here depicting dysprosium atoms intercalating in the van der Waals gaps between the layers in the crystal structure of MoS_2.

Chapter 3

Experimental Techniques and Requirements

In this chapter the theory behind the various experimental techniques will be presented. This will include topics as the principle of photoemission and how this can be used for X-ray photoelectron spectroscopy (XPS) and Ultraviolet photoelectron spectroscopy (UPS). The principles behind synchrotron radiation is included as it is important to understand how these influence the data quality in XPS experiments. In addition, this chapter will also cover the importance of vacuum systems and the theory and working principles of ARPES and LEED.

SECTION 3.1 Ultrahigh Vacuum, UHV

When performing photoemission and other surface science experiments it is paramount to be able to work in an UHV environment. The main reason for this is to keep the measured surface as clean as possible with a minimum amount of contamination. Sample preparation is often performed in vacuum condiditons seen as depositing a good quality thin film is dependent on the mean free path, l, of the residual gas molecules. This value should be larger than the distance between the vapor source and the substrate. Otherwise collisions between residual gas molecules and the evaporating material randomizes the vapor beam. The relation between the mean free path and vacuum conditions is emphasized in kinetic gas theory, where the mean free path is given by

$$l = \frac{k_B T}{\sqrt{2}\pi P a}, \tag{3.1}$$

where k_B is the Boltzmann constant, T is the temperature, P is the pressure and a is the molecular diameter. At room temperature and ambient pressures the mean free path for a gas molecule is on the order of nm. By reducing the pressure to around $10^{-4}\mathrm{mbar}$, the mean free path is close to 50 cm, while reducing it to UHV conditions (below $10^{-9}\mathrm{mbar}$) makes a mean free path on the scale of kilometers possible.

Secondly one can compare the incidence rate, r, of the residual gas molecules at the substrate with the incidence rate of vapor atoms. The incidence rate is related to the gas pressure by [19]

$$r = \frac{P}{\sqrt{2\pi m k_B T}} \tag{3.2}$$

where m is the molecular mass in units of the atomic mass constant. At the high-pressure limit ($\sim 10^{-4}\mathrm{mbar}$) and room temperature, the incidence rate of air impinging is about $3.8 \cdot 10^{16}\ \mathrm{molecules/cm^2 s}$ which is equivalent to 40 monolayers per second [19]. In vacuum applications, a convention widely used is a unit called Langmuir (denoted as L). Chorkendorff and Niemantsverdriet [20] defines this as $L = 10^{-6}\ \mathrm{Torr\ s}$. This is generally used as a rule of thumb saying that an exposure of $1 \cdot 10^{-6}\ \mathrm{Torr}$ for one second corresponds approximately to one monolayer of adsorbate. This is of course not entirely true as this assumes a sticking coefficient of the adatoms to be 100%, still it serves as good measure to how much time an experimentalist has before the sample has reached one monolayer of contamination. As a comparison, having a stable pressure of $2 \cdot 10^{-10}\mathrm{mbar}$ gives one around 10 hours to reach 1 Langmuir.

In order to achieve UHV conditions, several pumps have to be used. A roughing pump will be able to pump down to around $10^{-3}\mathrm{mbar}$. This kind of pump is generally used backing a turbo pump as these require quite low pressures to run. A turbo pump can potentially pump down to around $10^{-11}\mathrm{mbar}$. At around $10^{-7}\mathrm{mbar}$ an ion pump can be used to trap residual gas in the chamber and prevent it from interacting with the sample. The interested reader may read more about pump systems and their specifications in [21] and [22].

SECTION 3.2 Photoelectron Spectroscopy

In 1921, Albert Einstein was awarded the Nobel prize in physics for his description of the photoelectric effect. He discovered that when absorbing a photon, electrons are emitted from a sample with the maximum energy corresponding to

$$E_k = h\omega - \phi_s. \tag{3.3}$$

Here, $h\omega$ is the photon energy, and ϕ_s is the energy barrier the electron has to overcome to escape the material. The latter is also known as the material's *work function*. One has to note that not all the electrons that are emitted from a sample have the same kinetic energies. Due to the fact that electrons exist in different orbitals in the system, they are bound to the

material by different potentials. These energies are often referred to as binding energy and by taking this into consideration, equation 3.3 turns into

$$E_k = h\omega - E_b - \phi_s, \tag{3.4}$$

where the binding energy is referenced to the Fermi level. Characterization of a sample's electronic structure can be done by measuring the kinetic energy of the excited photoelectrons. In photoemission experiments this is done by an electron analyser. When the sample and analyser are placed in electrical contact, their fermi levels align (fig 3.1). This leads to a contact potential given by $\phi_s - \phi_a$, where ϕ_a is the analyser work function. This then leads to an off-set in the measured kinetic energy of the photoelectrons given by [8]

$$E_k = h\omega - E_b - \phi_a. \tag{3.5}$$

The technique of PES is primarily used for distinguishing the chemical composition of a material and also the surface electronic structure. PES is based on monochromatic electromagnetic waves incident on a sample. The light penetrates the surface and can thus interact with electrons in the uppermost atomic layers of the material. According to Hüfner [23], the process of photoemission can be described in three steps:

1) An electron is excited to a higher state by absorbing the incident photon's energy

2) The electron passes through the solid and to the surface

3) The electron penetrates the surface and is thus ejected into the vacuum

The three-step model has, despite its simplicity, proved to be quite useful. However, the model does not take into account that the emission process has to be described as one coherent excitation process. The *one step model* takes this into account and describes the photoemission process as a transition from an initial state ψ_i to a final state ψ_f. These transitions have a defined probability governed by *Fermi's golden rule* [24]:

$$P_{i,f} = \frac{1}{\hbar}\left|M_{i,f}\right|^2 \delta(E_f - E_i - h\nu) \tag{3.6}$$

Here the subscripts *i* and f are used to indicate the inital and final state quantities, respectively. The term $\delta(E_f - E_i - h\nu)$ comes from the energy conservation law and tells us that a transition can only occur when $h\nu = E_f - E_i$, meaning the photon energy has to match the energy difference of the two states. $M_{i,f}$ is the interaction matrix and contains information about electronic interactions in a system and is connected to the Hamiltonian as $M_{i,f} =< \psi_f|\hat{H}|\psi_i >$.

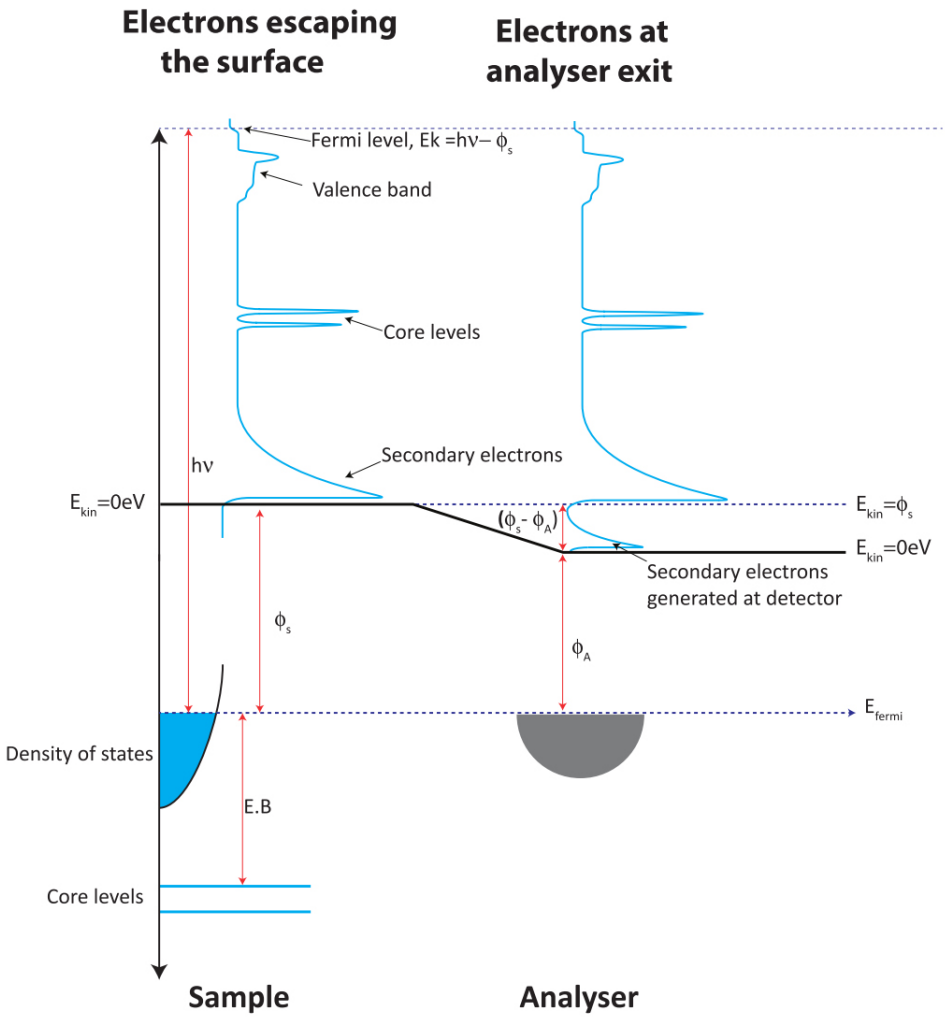

Figure 3.1: Energy diagram displaying energy alignment between the sample and electron analyser. Here depicting the difference in kinetic energy at the analyser and outside the sample. Adapted from Ref. 25.

SECTION 3.3

X-Ray Photoelectron Spectroscopy

XPS is a very powerful technique which allows you to take advantage of the photoemission process using light in the X-ray wavelength regime. The photons' energy ranges from around 100 eV (*Soft X-rays*), to more than 100 keV (*Hard X-rays*). For surface science applications, soft X-rays are typically used as probability of exciting an electron decreases with increasing photon energy.

3.3.1 Experimental Setup

Figure 3.2 illustrates the basic principles along with a schematic of a typical experimental setup. For XPS one needs means for generating photons in the X-ray regime. This is usually either done using an X-ray gun or by a synchrotron, which is further explained in section 3.7. In an X-ray gun electrons are accelerated from a heated filament towards an anode by an electric field. The energy transfer upon the electron impact may cause electrons from the inner orbitals of the anode material to be excited. Relaxation from outer orbital electrons into these available states then emits X-rays of specific energies depending on the anode material. When these X-rays hit the sample, photoelectrons are excited and accelerated towards an electron analyser using an electric field. The electrons then travel through the analyser, hitting an electron multiplier which in turn can generate a screen readout.

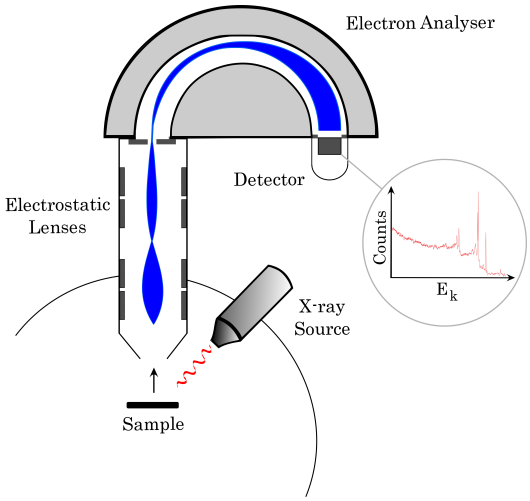

Figure 3.2: Schematic of a typical experimental setup for X-ray photoelectron spectroscopy. Here showing an X-ray source ejecting electrons from a sample that travels through an analyser and hits an electron multiplier, resulting in a screen readout.

3.3.2 XPS Spectrum Features

When analysing the XPS spectrum one should always note that there are several features other than the core level excited photoelectrons. This can be spectral features such as plasmon-loss peaks, satellites and Auger peaks. In addition, there are several loss mechanisms which result in a background noise in the spectra that need to be taken into account when analysing for example inelastic scattering, coulomb repulsion/attraction and other many-body interactions.

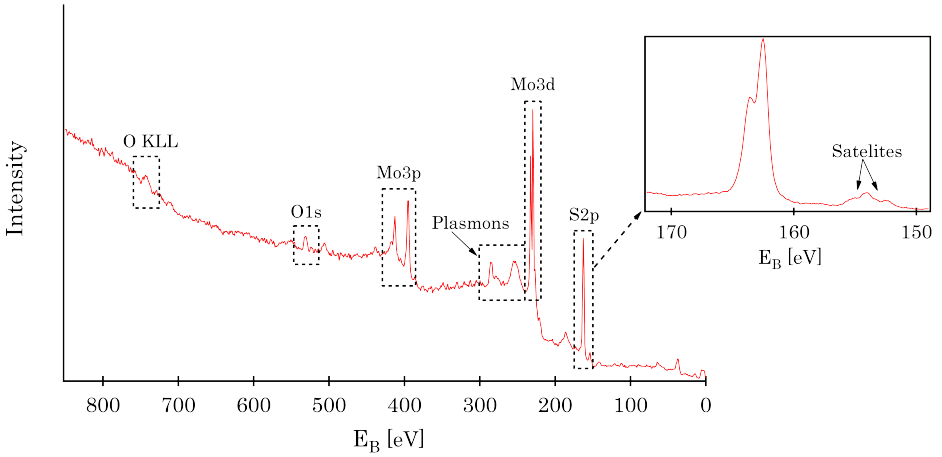

Figure 3.3: Widescan of a MoS_2 sample with minor oxygen contamination acquired with a MgKα anode. Here displaying the different features of an XPS spectrum. Core level emissions are depicted by their element and orbital of origin. The oxygen KLL auger is shown as well as the plasmon loss peaks of the Mo3d. A zoomed in scan of the S2p core level displays an example of satellites.

Satellites are a direct consequence of the non-monochromatic nature of X-rays generated by common lab sources. These sources usually use an aluminum window to attenuate the photons with unwanted energies. However, some of these photons might make it through the window and thus generate their own photoelectrons with slightly different kinetic energies. This results in replicas of the core level peaks at slightly different energies. These features can be completely removed by using close to perfectly monochromatic X-rays, like those achieved through synchrotron radiation.

Plasmon peaks arise from quantized oscillations of the valence electrons or free electrons in metals. Intrinsically this effect can occur by the coupling of the core-hole formed from a PES process and the oscillations of the valence states. As this process is happening simultaneously with the PES process, the photoelectron is ejected with lower energy. Extrinsically one can also view the possible interactions between the excited photoelectron and valence electrons as it propagates towards the materials' surface.

Auger peaks are results of a mechanism very much related to photoemission. The process

is a re-equilibriation of the materials' electronic structure after principle electron emission. A basic schematic of the Auger process can be viewed in figure 3.4. When a photoelectron is ejected it leaves a hole in its respective orbital. Then, there are two ways of renormalisation after this process:

1) An electron in a higher orbital can relax into and fill the hole left by the emitted electron, thus emitting an X-ray photon.

2) An electron in a higher orbital can relax into and fill the hole left by the emitted electron and release enough energy to knock out another electron from the same or higher orbitals into vacuum. This is defined as *Auger electrons*.

A positive trait of the Auger electrons is that they have constant kinetic energy regardless of the photon energy. Thus, they are easily distinguished when comparing two measurements with different photon energies. The spectral features at the same energies will then represent the Auger electrons.

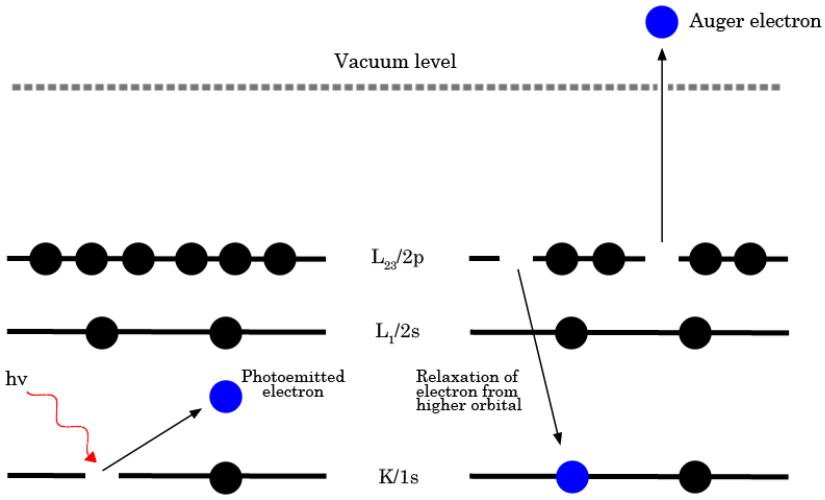

Figure 3.4: Schematic of a basic Auger emission process. Here depicting an electron being photoemitted from the K shell and the remaining hole being filled by an electron from L_{23}. The energy from this process is sufficient to knock out the auger electron.

A special case of the Auger process was presented by Koster and Cronig in Ref. 26. This is later known as a Coster-Kronig transition and is the case where the vacancy from the auger process is filled by an electron from a higher subshell of the same electron shell, meaning this can happen for the shells L and up. For the shells M and higher one can also have so-called *super Coster-Kronig transitions* where the emitted auger electron belongs to the same shell. Such transitions have an impact on the core-hole lifetime of the states and can be seen in differing widths of the spectral functions.

3.3.3 Analysis

XPS is a neat technique to both qualitatively and quantitatively analyse a sample. For qualitative measurements XPS offers a non-destructive way to probe a sample and identify its components. By comparing acquired spectrums as the one seen in figure 3.3 with various databases, the different elements in a sample can be identified. The binding energy of a sample's core level components tells a lot about the chemistry.

Depth and angular dependency of XPS signal

The depth sensitivity of XPS mesaurements will vary with the kinetic energy of the electrons under consideration. It is determined by a quantity known as the attenuation length, λ, of the electrons, which is related to the inelastic mean free path (IMFP). The attenuation length is about 10% less than the IMFP and various databases exist from which values of IMFP and attenuation length can be obtained [27].

It is paramount to understand that the measured intensity from an XPS experiment will be dependent on several variables. Some of these variables will be sample dependent and others will depend on the instrumental limitations and settings. The measured intensity from an experiment is

$$\mathrm{d}I = N_z(x,y,x)\sigma_z e^{-\frac{t}{\lambda_z \cos\theta}} \Phi_{X-ray}\Omega(E_k,x,y,z)\mathcal{E}_D \mathrm{d}x\mathrm{d}y\mathrm{d}z \tag{3.7}$$

where Φ_{X-ray} is the incident X-ray flux, $N_z(x,y,z)$ is the number of atoms/molecules in the measured volume, and $\Omega(E_k,x,y,z)$ is the acceptance solid angle of the electron analyser. σ_z is the photoelectric cross-section of the given element number z, and is discussed in more detail in section 3.5. $\mathcal{E}_D$ is the instrument detection efficiency. The last three terms in eq. 3.7 should under normal conditions remain constant as they are instrumental. Nevertheless, the instrument detection efficiency is also dependent on what is often referred to as the analyser transmission function. This is a measure of the analysers efficiency to detect electrons at varying kinetic energies and, needs to be calibrated for each system. An approximation of the transmission function for the synchrotron experiments is shown in chapter 4. If one assumes the measured sample to be homogenous, equation 3.7 can be simplified and the total intensity for a given element can be reduced to

$$I = \sum_z \rho_z \sigma_z \lambda_z K \tag{3.8}$$

where K now contains all the instrumental paramteres.

The intensity of electrons emitted at an angle to the surface normal can be derived using the *Beer-Lambert* relationship, resulting in the following relation:

$$I = I_0 e^{\frac{-t}{\lambda \cos\theta}} \tag{3.9}$$

This is the foundation of what is called angle resolved X-ray photoelectron spectroscopy ARXPS. Here *I* is the electron intensity and I_0 is the intensity measured before depositing an overlayer, and *t* is the overlayer thickness. This relationship can be used to determine the effective attenuation length by the overlayer method as described by S. Hüfner in Ref. 23. If the attenuation length of the material is known, the overlayer thickness can be determined by plotting $\ln(\frac{I_0}{I}) \cdot \lambda \cos\theta$ as a function of $\cos\theta$.

Song *et al.* have also shown how to use the idea of a finite element model to determine the layer-by-layer stoichiometry in a sample [28]. Here one assumes that the intensity from a certain core level follows the relation seen in equation 3.10.

$$I_z \propto \sum_i Q_{z,i}\sigma_z e^{\sum(\frac{-x_i}{\lambda(E_k)\cos\theta})} \tag{3.10}$$

Where *i* indexes each layer, x_i is the depth of the layer, $\lambda(E_k)$ is the electron mean free path at the appropriate kinetic energy E_k, *z* denotes which element that is considered and θ is the emission angle. σ_z is the photoionization cross section of the given element. One can then take advantage of this relation knowing that the relative quantitiy of a given element is independent of instrumental parameters.

Modelling peak shapes

As stated by Hesse *et al.* in Ref. 29, the energy distribution curves in photoelectron spectroscopy may be theoretically modelled using spectral functions. These take into account all the possible excitation processes in the sample of interest. In a perfect theoretical system, the observed peaks should be sharp delta-peaks centered at the respective binding energies of the different orbitals in the measured system. In a real system however, the peaks widen due to several contributions, whereas some are discussed in this section. The spectral shapes of the peaks are typically determined by a Lorentzian and a Gaussian contribution.

Lorentzian contribution

The Lorentzian contribution arises from the renormalization of the core hole created after a photoelectron has been emitted in the PES process. The core hole lifetime, usually denoted τ, is a measure of how long it takes for this to happen. In this process the emitted photoelectron can both recieve and lose energy by interacting with the electron refilling the core hole. A shorter lifetime thus means a faster collapse and usually leads to a larger energy change in the emitted photoelectron and a wider distribution. This change in energy is connected to the quantum mechanical transition probabilities and is often theoretically modelled to have a Lorentzian distribution given by

$$L(E, w_L) = \frac{2w_L}{4(E - E_0)^2 + {w_L}^2}. \tag{3.11}$$

Here E_0 corresponds to the centrum of the peak and w_L to the distribution's full width at half maximum (FWHM). Normalization constants and function amplitude have been left out for simplicity.

Gaussian contribution

Monochromatic X-rays, as those from a synchrotron, can be seen as a Gaussian beam. This is a beam whose field amplitudes are given by a Gaussuan function, implying that the intensity of the incoming photons have a Gaussian distribution profile. The Gaussian broadening in the measured spectra is mostly due to this fact, but also the measurement process in the spectrometer. The height-normalized Gaussian function $G(E, w_G)$ as shown in equation 3.12 is characterized by the parameters w_G and E_0, corresponding to the FWHM and the peak position, respectively

$$G(E, w_G) = e^{-4ln(2)\cdot(\frac{E-E_0}{w_G})^2}. \tag{3.12}$$

Voigt profile

The best description of the core level line shape is obtained by convoluting independent Gaussian and Lorentzian contributions [23, 29]. The convolution is called the Voigt function and is defined as

$$f(E) = f(L * G) = \int_{-\infty}^{\infty} L(E')G(E - E')\mathrm{d}E'. \tag{3.13}$$

This profile function has to be evaluated numerically, making the fitting process more time-consuming. Nevertheless, a simplification using a linear combination, or the product of the Gaussian and Lorentzian, has proven to give accurate results in many cases. This solution is often referred to as the *pseudo-Voigt function*. There has been some debate whether the product of the sum of the contributions gives the most true form of the Voigt profile [25]. In this report, the pseudo-Voigt profile will be modelled as

$$V_p(E) = I \cdot (\mu L(E, \beta) + (1 - \mu)G(E, \beta)), \tag{3.14}$$

where the parameter μ is to describe whether the signal acquired from the instrument is mostly originated from the Gaussian or the Lorentzian contribution and *I* is defined at the total area of the measured signal. The parameter β is modelled as the Pseudo-voigt width (PVW) using a suggested approximation from Ref. 30

$$\beta = [W_G^5 + 2.6927 \cdot W_G^4 W_L + 2.4284 \cdot W_G^3 W_L^2 + 4.4716 \cdot W_G^2 W_L^3 + 0.0784 \cdot W_G W_L^4 + W_L^5]^{\frac{1}{5}}. \tag{3.15}$$

Here, W_G and W_L is the width of the Gaussian and Lorentzian contribution, respectively.

Spectral Background

In addition to the peak shapes themselves there is an important contribution to the signal arising from inelastic scattering and other many-body interactions amongst the excited

electrons. All these add up to what is referred to as the spectrum's background. To extract the true peak signal of a given orbital, this background must be subtracted from the acquired data. In this, thesis the Shirley background is used to model these features, described in more detail in Ref. 31. This model assumes that the background intensity at any given binding energy is proportional to the peak area above. To approximate this, the background of a given peak is modelled using the error function

$$f_{erf}(x) = \frac{2}{\sqrt{\pi}} \int_0^x e^{-t^2} \mathrm{d}x. \tag{3.16}$$

In addition, an off-set is included to take into account contributions from peaks at higher binding energies.

Maximum Entropy Modeling

When modeling the compositional variation, one can separate the sample into partitions using the multilayer method as described earlier. Then the sample is separated into i layers, where each layer contains the a quantity of an element, Q_Z as seen in figure 3.5.

In order to model the acquired ARXPS data, a maximum entropy method can be employed [32, 33]. One has to remember that the observed spectra are the convolutions of the emission from a sample with the detector function. If deconvolution of the spectra was possible, the spectra of electrons incident on the detector could be estimated. However, there may exist more than one solution to such a deconvolution problem, and thus one will have to choose one over the other. One suggested "procedure" for doing so is based on maximizing the entropy. This quantity is a direct measure of the uncertainty in the data and a justification of this can be found in the work by Shore [34]. Structural entropy in a system, (S) is defined as

$$S = -\sum_i p_i \ln(p_i) \tag{3.17}$$

where p_i is the probability that of ith element taking its observed value. Karmeshu [35] state in his work that "of all distributions satisfying the constraints supplied by the given information, the minimally prejudiced distribution $P(S_n)$ is the one that maximizes the system's entropy". This means that in the absence of complete information, the only justifiable solution is the one with the most uncertainty. Accepting any other solution automatically implies that additional information can be gained from the data that might very well not be the case.

In this thesis a maximum entropy model has been used. To determine the quality of the fit, a Chi-squared approximation is used, defined as

$$\chi^2 = \sum_i \frac{(I_i^{calc} - I_i^{exp})^2}{\sigma_i^2} \tag{3.18}$$

where σ_k represents the standard deviation of the ith element of the spectrum. The expression minimized when performed the fit comes from combining equations 3.17 and 3.18 into

$$S - \alpha\chi^2 = -\sum_i \left(p_i \ln(p_i) - \alpha \frac{(I_i^{calc} - I_i^{exp})^2}{\sigma_i^2} \right) \tag{3.19}$$

where the parameter α has been introduced. This parameter is used to make sure the maximum amount of information is extracted from the data, whilst not over-fitting. By tuning α, one can maximise the entropy while keeping $\chi^2 = N$, where N is the number of data points. Effectively, this means that all the available information has been extracted from the data.

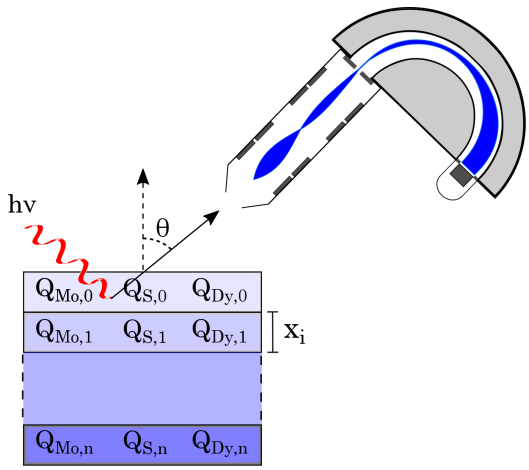

Figure 3.5: Schematic of the finite element model and measurement geometry. The sample is considered as a sum of layers of thickness x_i where each layer contains the quantity of an element $Q_{z,i}$. Here also showing the incident photon beam and the detected emission angle θ.

SECTION 3.4 Spin-orbit Splitting

The peaks in the XPS spectra, derived from orbitals whose angular momentum quantum number is greater than 0, are split into two. This is a direct result of interaction between the electron angular momentum (due to its spin) with its orbital angular momentum, or what is called *spin-orbit interaction*. As the total angular momentum of an electron is given by

$$j = |l \pm s| \tag{3.20}$$

where s is the spin quantum number $\frac{1}{2}$. A p orbital can for example take angular momentum of either $\frac{1}{2}$ or $\frac{3}{2}$. The relative intensities of the components of the doublets formed by the *Spin-orbit coupling (SOC)* are dependent upon their degeneracies given by $2j + 1$.

Using these relations one can then calculate area ratios for different SOCs as shown in table 3.1.

Table 3.1: Total angular momentum and respective area ratios for spin-orbit splitting in different orbitals.

Subshell	j	Ratio
s	$\frac{1}{2}$	n/a
p	$\frac{1}{2} \vee \frac{3}{2}$	1:2
d	$\frac{3}{2} \vee \frac{5}{2}$	2:3
f	$\frac{5}{2} \vee \frac{7}{2}$	3:4

SECTION 3.5 Photoionization Cross-section

Fermi's golden rule, as described in equation 3.6, was mentioned in section 3.2. To make quantification of XPS spectrums possible, one would need to know the physical probability of ionizing a system by electromagnetic radiation at a given energy. This probability is often called the element's *photoionization cross-section*. The amount of electrons excited is a function of the amount of incident photons and include all possible excitations of each orbital in the system being investigated. Note that Fermi's golden rule effectively describes the lifetime of a photogenerated electron hole within the given system and can be used to calculate the photoionization cross-section for different elements taking into account all the possible transitions in said system.

The calculated atomic cross-sections for photoionization can be acessed in various data tables. In this thesis, a web interface displaying data taken from J.J. Yeh and I. Lindau's work in refs. 36 and 37 has been used. The cross sections of the most relevant orbitals for this work are seen in figure 3.6.

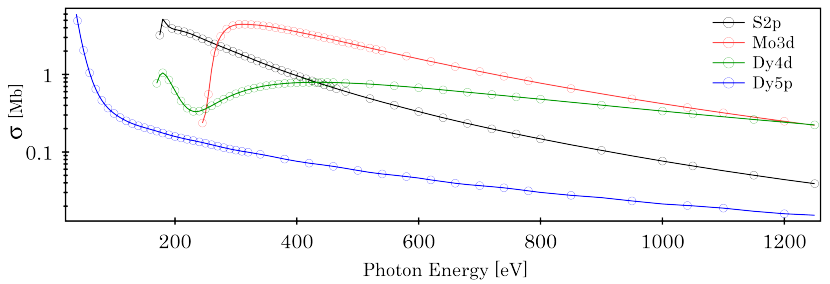

Figure 3.6: Photoionization cross-sections of S2p, Mo3d, Dy4d and Dy5p orbitals.

SECTION 3.6 Angle-Resolved Photoemission Spectroscopy

ARPES is an experimental technique that uses the photoelectric effect to probe the electronic properties of solids. This allows for the band structure of a given material to be mapped out directly as a function of the scattered angle of the electrons, which can then be mapped to crystal momentum.

3.6.1 Physical Principle

Previously, the kinematics of photoemission have been discussed, but only the energy of the excited photoelectron has been accounted for. By expanding the view to also include the electrons' momentum, $\vec{k}$, the band structure of the solid becomes obtainable. The wave vector or momentum of the electron is usually divided into two components; $\vec{k_{\parallel}} = \vec{k_x} + \vec{k_y}$ and $\vec{k_{\perp}} = \vec{k_z}$. The modulus of the wave vector is from quantum mechanics given as:

$$k = \frac{\sqrt{2m_e E_k}}{\hbar} \tag{3.21}$$

where m_e is the electron mass, E_k the kinetic energy and $\hbar$ the reduced Planck constant.

Studying the energy dispersion, $E(\vec{k})$, of the bulk states in a material, is generally much more complicated than studying a two dimensional band structure. The reason for this is that the perpendicular component of the momentum, $\vec{k_{\perp}}$, is not conserved in the photoemission process and it is not even a good quantum number as the introduction of the surface disrupts the lattice periodicity in this direction [38]. Studying two dimensional states using ARPES is not necessarily restricted to surface states as there are several classes of three dimensional solids that essentially behave as two dimensional. In this thesis the material studied is the layered MoS_2, which behaves in this manner. By measuring the parallel component of the electrons' momentum, the sample band structure similar to that of figure 2.3 can be calculated.

3.6.2 Experimental Setup

When performing ARPES measurements one has to connect the electrons' momentum to the emission direction from the samples. The momentum of an emitted electron at an angle θ and ϕ can be decomposed to

$$\vec{k_x} = \frac{\sqrt{2m_e E_k}}{\hbar}\sin\theta\cos\phi \qquad \vec{k_y} = \frac{\sqrt{2m_e E_k}}{\hbar}\sin\theta\sin\phi \qquad \vec{k_z} = \frac{\sqrt{2m_e E_k}}{\hbar}\cos\theta \tag{3.22}$$

where the relevant angles are depicted in figure 3.7. The electron analyzer detects emitted electrons at a finite acceptance angle. By preserving the electron momentum, the angular dispersion detected by the CCD camera is directly related to the electron's momentum. As the electrons' momentum components are both functions of the energy and the angular orientation of the sample, a procedure known as "k-warping" needs to be done to map the acquired data to reciprocal space.

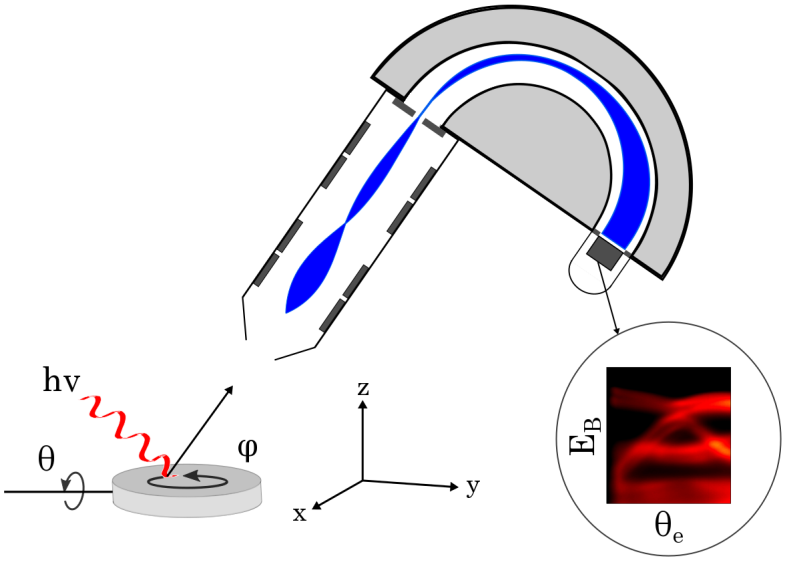

Figure 3.7: Schematic setup of an ARPES experiment. Electrons excited from the sample are transferred through the analyser at a given acceptance angle. The momentum is conserved through the hemispherical analyser and the electrons hitting the CCD screen displays a dispersion in both energy and angle. Notice that depending on the instrument setup, the scan is done through either slices of k_x or k_y depending on the analyser orientation. This means every scan if done with one of these components fixed and can be changed through sample rotation. Screen readout depicts the band structure of MoS_2 around the $\bar{M}$-point.

Notice that as the CCD screen displays energy dispersion along one axis and angular dispersion along the other. This means that only one direction in momentum space can be probed at a given time. In the case of the instrument at NTNU, the detector is set up in a manner such that the maximum acceptance angle of the analyser of $\pm 15^\circ$ yields an effective scanning range of $k_x = \pm 0.14\sqrt{E_k}$. The unit of k_x is Å^{-1}.

SECTION 3.7 Synchrotron Radiation as a Lightsource

As mentioned in section 3.3.2, unwanted features, such as satellites, originate from not having monochromatic X-rays. These features can be removed by using light from a synchrotron source.

When electrons are travelling at relativistic speeds and forced to change their direction of motion due to a magnetic field they will emit electromagnetic radiation known as synchrotron radiation. The closer this speed gets to the speed of light, the more focused the light will be in the tangential direction to the travelled path as can be seen schematically in figure 3.8.

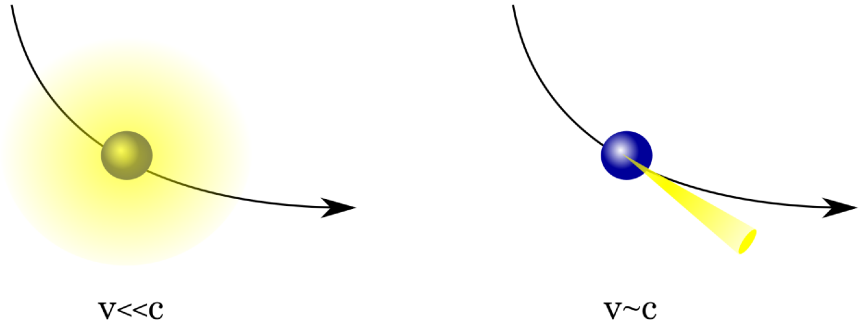

Figure 3.8: Electromagnetic radiation emitted by accelerating electrons. Adapted from Ref. 39.

Willmatt [39] states that a synchrotron consits of five main components (a schematic can be viewed in figure 3.9).

1) A source of electrons; normally generated by thermionic emission from a hot filament in an electron gun.

2) A booster ring into which the electrons are injected from a linear accelerator (linac), which typically is a series of oscillating electric potentials along a linear beamline. In the booster ring the electrons are further accelerated to match the energy of the storage ring. They are then periodically injected into the storage ring, so that the specified storage ring current is maintained.

3) The storage ring contains the electrons and maintains them on a closed path by the use of an array of magnets, commonly referred to as the 'magnet lattice' of the ring. The magnets are most commonly of three types: dipole- or bending magnets cause the electrons to change their path and thereby follow a closed path; quadrupole magnets are used to focus the electron beam and compensate for Coulomb repulsion between the electrons; and sextupole magnets correct for chromatic aberrations that arise from the focusing by the quadrupoles.

4) A radio frequency (RF) supply is used to supply the electrons with energy every time they pass through to replenish the lost energy after emitting radiation.

5) The beamlines run off tangentially to the storage ring, along the axes of the insertion devices (presented in more detail in the next paragraph), and tangentially at bending magnets. The beams are then normally focused and/or monochromated in the optics hutch before it enters the experimental hutch.

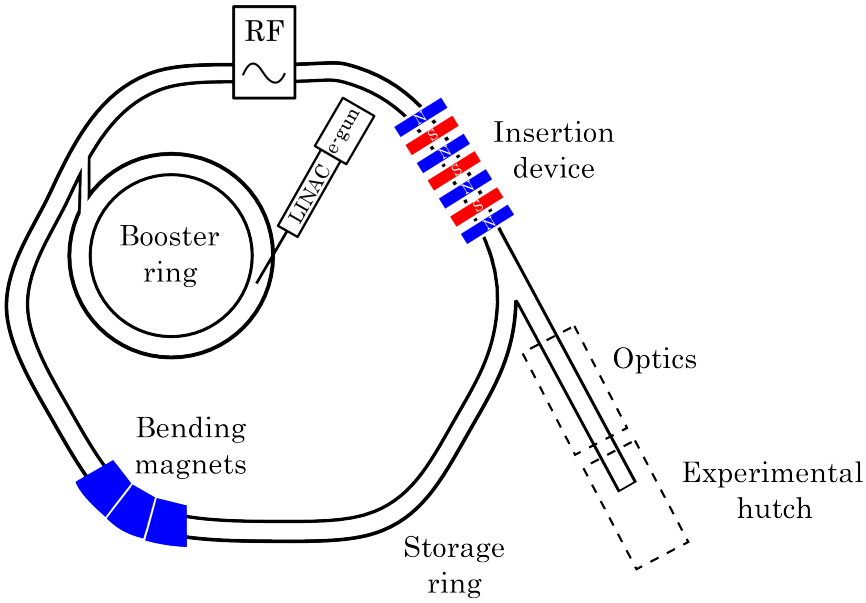

Figure 3.9: Schematic containing the most important components in a synchrotron setup. Here we see electrons from a source accelerated in a linear accelerator into a booster ring to undergo further acceleration. When the desired energy is reached, they are injected into the storage ring. The beamlines then use the radiation emitted from the insertion devices (wigglers or undulators), and from the bending magnets. Adapted from Ref. 39.

3.7.1 Insertion devices

To further increase the quality of the generated synchrotron light, insertion devices (IDs) are used. Such devices consist of magnets in periodic arrays. By alternating the magnetic poles in such an array one can force the electrons' trajectory to oscillate perpendiculary to their direction of motion and therefore emit radiation during each individual oscillation as seen in figure 3.10. The wavelength of the resulting synchrotron light is then dependent on the parameters of the insertion device, as the period of the magnetic array and the effective magnetic field. Kapadia [40] defines the primary effects of the IDs as:

- Increasing the intensity of the emitted radiation

- Increasing the spectral brightness[1] due to the small cross section of the photon beam and low divergence of the radiation

There are two types of insertion devices; *wigglers* and *undulators*. These are distinguished from one another by the degree to which the electrons are forced to deviate from a straight path. For large enough angle excursions, the radiation cones from each "wiggle" do not overlap and therefore the intensities are added and the ID is referred to as a wiggler. For smaller excursions the ID is called an undulator. Here the radiation cones overlap and interfere with one another. In this case the field amplitudes are added vectorically and the sum is squared to calculate the intensity.

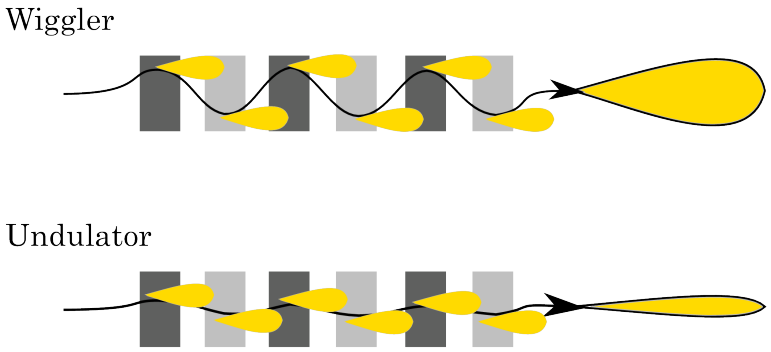

Figure 3.10: Working concept of a wiggler and an undulator. Schematically showing the electrons divergence from the straight path. Adapted from Ref. 39.

3.7.2 Monochromator

To further narrow down the spectral distribution of the synchrotron light and achieve a well defined photon energy, a monochromator is often used. The monochromatisation of light is usually achieved by the principle of diffraction. There are several ways to achieve this, but commonly diffraction gratings with angular variation or crystals are used. By diffraction of several objects in an array one can effectively filter out unwanted wavelengths. One has to remember that from the Bragg conditions

$$n\lambda = d\sin\theta, \tag{3.23}$$

higher order wavelengths are also diffracted in the process, but with decreasing intensity. This has to be kept in mind when regarding spectral features from synchrotron light as there is always some intensity from light of higher order wavelengths which can give rise to the observation of signals at higher kinetic energies than the set wavelength, as is discussed in chapter 4.

[1] Defined as the number of photons emitted per second in a spectral bandwidth $\frac{\Delta E}{E} = 0.1\%$ in a unit source area and per unit of solid angle [40]. Notice that brightness is proportional to intensity.

SECTION 3.8

Low Energy Electron Diffraction

LEED is a technique that can be used to determine the crystal structure of a material's surface. It takes advantage of the diffraction occuring when directing a beam of low energy electrons towards a surface. These diffracted electrons are then detected using a fluorescent screen. A typical experimental setup is shown in figure 3.12.

This experimental technique proves very powerful in i.e. observation of surface reconstruction of a sample and also in determining the crystal symmetry of a sample. In addition, LEED is useful for measurements by angle resolved photoemission spectroscopy when used to align the sample in high symmetry directions. In this thesis, however, the usage of this technique is focused on determining both the crystalline reconstruction of an adsorbate layer on a substrate and the quality of an overlayer on a surface, as a disordered overlayer would obscure the diffraction pattern.

Working principle

By using sufficiently low electron energies, the penetration depth of the electrons becomes so short that they can only interact with top few atomic layers of the sample. By simplification one can then regard this as a two dimensional material, and there will be no diffraction condition in the perpendicular direction. The conditions for diffraction is still governed by the Laue conditions given by

$$\mathbf{k}_\mathbf{s}^{\parallel} - \mathbf{k}_\mathbf{i}^{\parallel} = \mathbf{G}_\mathbf{hk} \tag{3.24}$$

where $\mathbf{k}_\mathbf{s}^{\parallel}$ and $\mathbf{k}_\mathbf{i}^{\parallel}$ are the components of the scattered and incident electron wave vectors parallel to the surface, respectively, and $\mathbf{G}_\mathbf{hk}$ is a surface reciprocal lattice vector.

The *Ewald sphere* is a geometric construction of which one can observe the relation between the wavevector of incident and diffracted beams. As opposed to when regarding a 3D material when constructing the Ewald sphere one would now replace the discrete lattice points by rods perpendicular to the surface. This is justified by arguing that the real-space periodicity in the third dimension is infinite, which means that the reciprocal lattice points have to be infinitely close to each other, thus rods are formed [38]. In this case one would expect constructive interference whenever a rod intersects the Ewald sphere as depicted in figure 3.11.

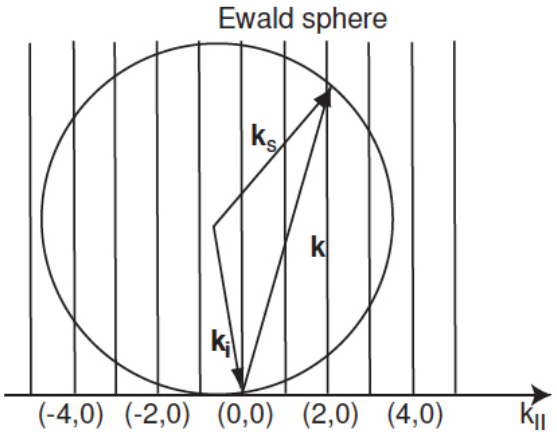

Figure 3.11: Eswald construction for the two dimensional lattice case. Adapted from Ref. 38.

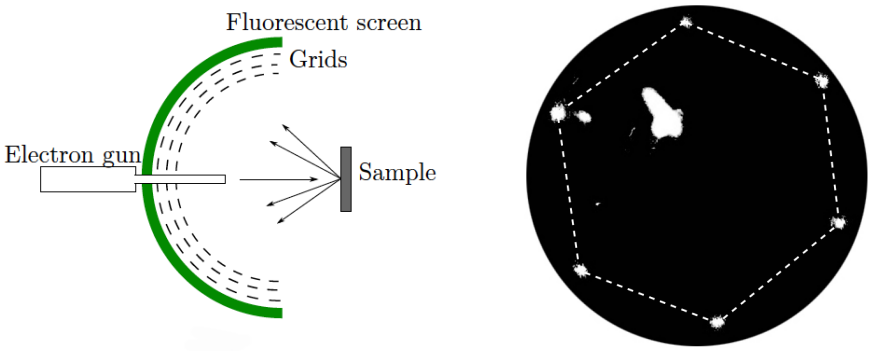

Figure 3.12: LEED schematic adapted from Ref. 9, and diffraction pattern generated by elastically scattered electrons hitting the fluorescent screen from of a cleaved MoS_2 crystal at 104 eV. The smaller spots originate from high symmetry points in the reciprocal lattice. Also seen is the electron gun covering some of the screen.

Chapter 4

Materials & Method

SECTION 4.1 Sample Preparation

Before introducing the samples to the vacuum chamber, they were cleaved by applying a layer of scotch tape on the surface and tearing it off as shown in figure 4.1. This is done in order to produce a new and cleaner surface. If the cleave is done properly, it should also be possible to create a surface of high crystallographic quality. The MoS_2 was then loaded onto a tantalum plate with tantalum clips. Tantalum is an inert transition metal with a high melting point and good thermal conductivity, making it suitable as a sample holder. When loading a new sample, a scan for regular contaminants such as C, O and Fe was done to ensure the sample quality. If the sample quality was not sufficient, an annealing process at $300°C$ was done to remove surface impurities. This is to ensure that the annealing after deposition releases as few impurities from the bulk MoS_2 as possible into the measured surface layers, which is important as available contaminants might lead to unwanted chemical reactions.

For measurements using angle resolved photoemission spectroscopy, it was necessary to perform low energy electron diffraction as the samples have an unknown crystal orientation. In addition to finding the crystal orientation, LEED also allows for observation of the crystal quality. A poor quality LEED pattern would most likely mean that acquiring ARPES data would be very difficult. As the system at NTNU did not have a ϕ-drive, there was no way to correct for the crystal orientation other than withdrawing the sample from the chamber and rotating it manually.

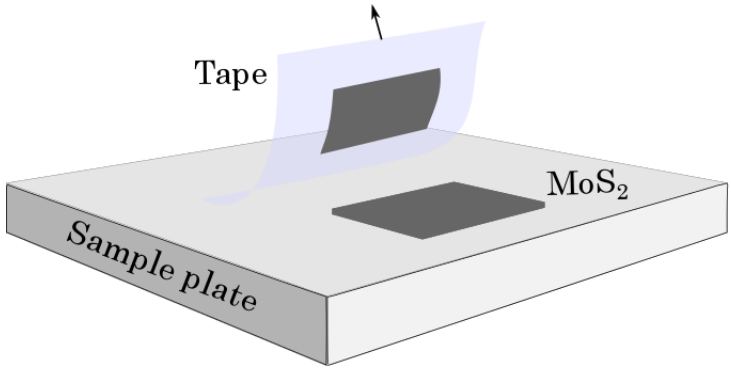

Figure 4.1: Schematic of the scotch tape sample cleaving method. The tape is adhered to the sample surface and cleaves the MoS_2, revealing a new surface layer.

SECTION 4.2 Evaporator Build & Deposition

The evaporators used for deposition of dysprosium in Århus, and in the XPS lab at NTNU, were made in a similar manner. The evaporators are based on thermal evaporation. Dysprosium was packed inside a tantalum foil, which has a melting point at around 3000°C in atmospheric pressure conditions. The ends of this foil were spot welded onto two separate electrodes that allow a current to flow through. A hole was made in the foil to define the direction of evaporation. By adjusting the current through the tantalum, the dysprosium is heated up and eventually evaporates in the direction of the sample. This method is somewhat less controllable than for example e-beam evaporation, but with proper calibration, overlayers of good quality can be made. A schematic of the evaporation procedure is illustrated in figure 4.2.

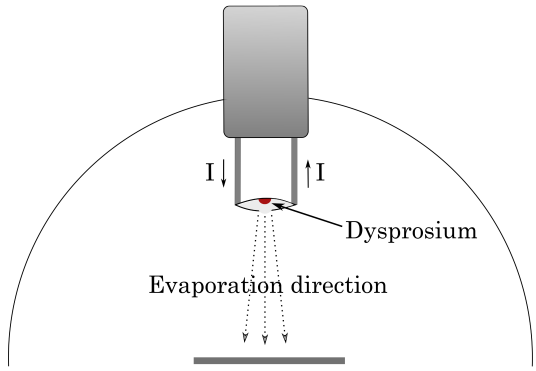

Figure 4.2: Schematic of the evaporator used in the experiments. Here showing a piece of dysprosium inside a conductive foil with a current running through. The Dy heats up until it starts to evaporate out of the hole in the foil and towards the sample.

SECTION 4.3 Thermal Treatments

The experiments conducted in Århus required the sample manipulator to be cooled down to liquid nitrogen temperature to observe the propagation of the chemical reaction between sulphur and dysprosium. This was done by pouring nitrogen through an inner tube on the manipulator arm. The arm had to be refilled every half an hour as the nitrogen evaporates quite rapidly. A disadvantage when cooling to such low temperatures is that the sample becomes more prone to contamination. Lowering the sample temperature decreases the energy of the system. This in turn makes the sample a site where it is energetically favourable for contaminants such as C and O to adhere on the surface. As long as the goal of the experiments was to observe the changes in the sulphur spectrum, this was not an issue.

To achieve more stable heating when measuring a series of temperatures, with steps of approximately 50 $^{\circ}\mathrm{C}$, the sample was heated against the liquid nitrogen cooling. By doing so one can decrease the probability of overheating due to thermal delays in the heating mechanism. Having liquid nitrogen in the system while heating helps to ensure that the sample is left in the chemical state of the highest achieved temperature as the heating subsides. The measurements were then performed for temperatures from -140$^{\circ}\mathrm{C}$ up to 350$^{\circ}\mathrm{C}$.

SECTION 4.4 Oxygen Exposure

To observe how different films of dysprosium react in an oxygen environment, a stable O_2-pressure of $10^{-6}\mathrm{mbar}$ was introdcued to the vacuum chamber for a total duration of 10 minutes. It was then observed how a sample with a dysprosium overlayer of 2-3 nm with no prior annealing treatment reacted to the oxygen by the means of XPS. The sample was then subjected to two subsequent anneals of 150$^{\circ}\mathrm{C}$ and 300$^{\circ}\mathrm{C}$. The same procedure was done on a sample of thickness 2-3 monolayers which was annealed to 300$^{\circ}\mathrm{C}$ prior to the oxygen exposure. This sample was then followed by a secondary anneal at 300$^{\circ}\mathrm{C}$ after exposure to observe possible chemical reactions.

SECTION 4.5

Transmission Function Approximation

To reduce the uncertainty when modeling the stoichiometry of the sample, one needs to account for various factors. In section 3.3.3 the analyzer transmission function was mentioned. In most instruments made for research this is accounted for in the software, but at MATLINE in ASTRID-2, it is not. To approximate the transmission function, spectra was acquired at three different photon energies (230, 400 and 450 eV) from a clean silicon carbide sample. As the decay of the transmission function should be close to exponential [41, 42], the data was modeled as a negative exponential function. The Si2p core level was measured at the previously mentioned photon energies and modeled with binding energy 99.42 eV and a spin splitting of 0.4 eV [43]. In the model, the Lorentzian component was kept constant as the change in the core level in this case mostly is governed by the change of the incoming radiation [29]. In figure 4.3 the total intensity from the Si2p is displayed as a function of the excited electrons' kinetic energy.

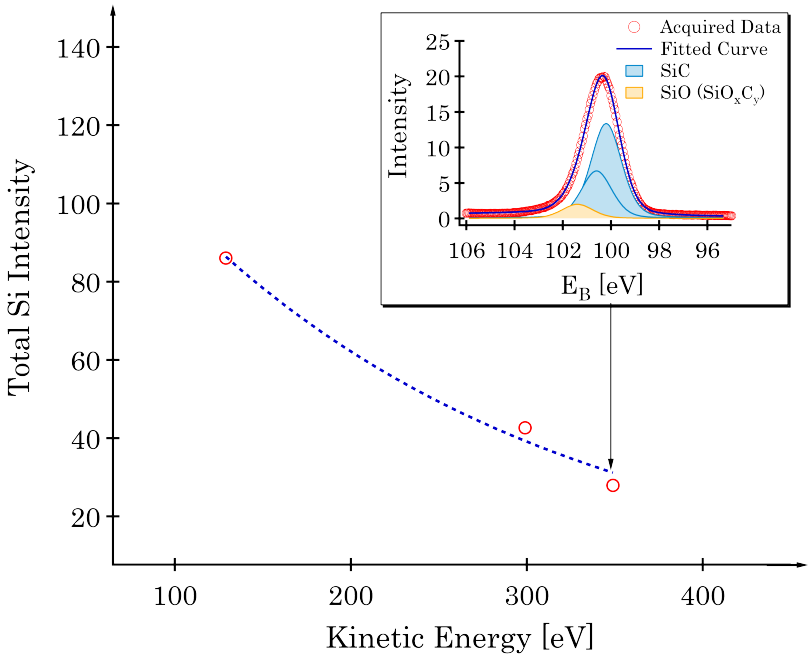

Figure 4.3: Si2p intensities as a function of kinetic energy. Red circles are the raw data and the dotted blue line is the exponential fitted curve $T(E)$. The window contains the Si2p XPS scan at $h\nu = 450\text{eV}$ and includes the deconvoluted SiC signal in addition to a SiO component which will be present if there is oxygen on the sample [44, 45]. Measurements were done using photon energies of 230, 400 and 450 eV.

Fitting the data was done using an exponential model on the form $T(E) = Ae^{\frac{-(x-x_0)}{\tau}}$.

Further work with this relation was done using the transmission relative to the kinetic energy of 129eV such that a scaling factor can be calculated as

$$t(E) = \frac{A}{T(E)} = e^{\frac{x-x_0}{\tau}} \tag{4.1}$$

where in this case $\tau = 215.05$ and $x_0 = 129$. This relation is used to correctly normalize the ARXPS data from the experiments conducted at the MATLINE beamline in Århus.

SECTION 4.6 Calculating Deposition Thickness

When caluclating the thickness of the deposited dysprosium overlayer, equation 3.9 is used. In the measurements done in Århus, the calibration was performed on a "dummy" MoS_2 sample and the molybdenum 3d core levels was acquired using XPS before and after deposition as shown in figure 4.4. The sulphur core level could not be used for this intention, as segregation towards the material surface has been observed and would give the impression of a thinner dysprosium overlayer. Using the NIST EAL database [46], one can estimate the attenuation length of the given material and calculate the overlayer thickness as $t = \lambda \ln(\frac{I_0}{I})$ at normal emission.

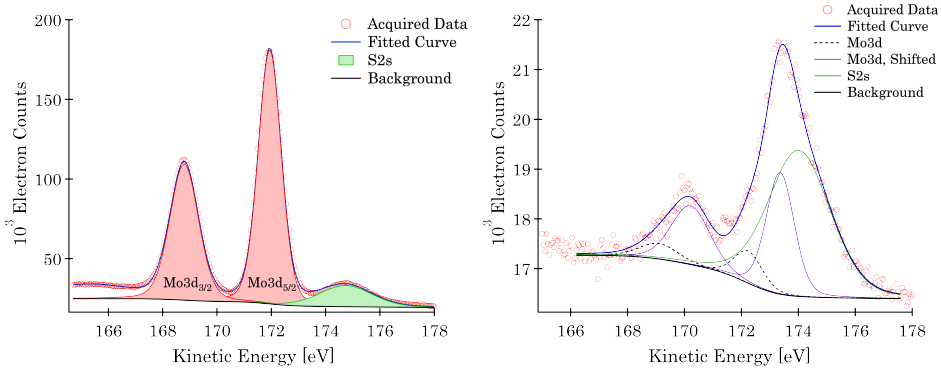

Figure 4.4: Measured Mo3d core level before and after deposition of dysprosium. Clearly depicting the strong attenuation of the Mo3d signal. Notice how the attenuation of the S2s core level is significantly. Measurements were done using a photon energy at $h\nu = 400$ eV to maximize the photoionization cross-section.

For the ARPES measurements done in the lab at NTNU, the amount of samples was limited. Hence the calibration of the dysprosium evaporator was done using a Au (100) single crystal and measuring the attenuation of the Au4f orbital as seen in figure 4.5. This is a method that is often used for calibrating such experiments as clean single crystal makes it easier to calculate the electron attenuation length in the material. The attenuation length of Au4f measured with a MgKα anode is experimentally known to be in the range of 1.8-2.2 nm [47, 48].

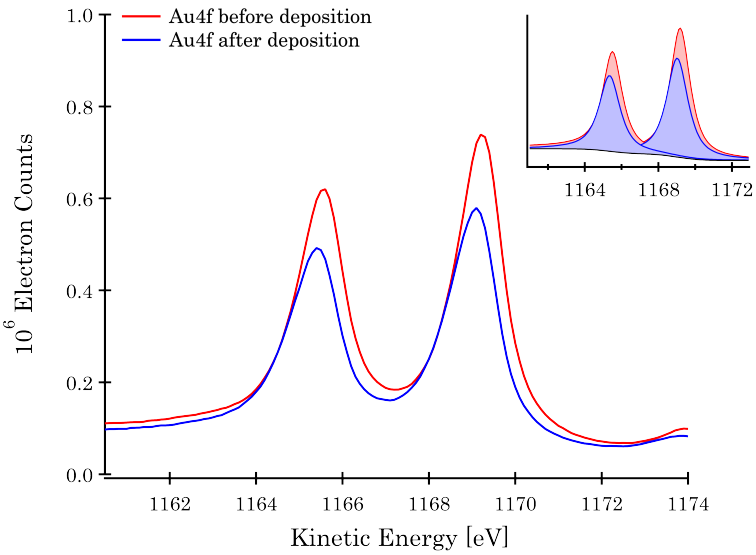

Figure 4.5: Mesured Au4f core level before and after dyrsporsium deposition, red and blue line is before and after deposition, respectively. The graph in the top right corner depicts the deconvoluted spectra for closer area comparison. Measurements were done using a MgKα anode ($h\nu = 1253.6$ eV).

SECTION 4.7 Monochromator Energy Correction

Even though the insertion devices in a synchrotron help to narrow the spectral distribution of the radiation, a monochromator is usually used to achieve a well defined photon energy. At the ISA synchrotron facility, the setup consists of a diffraction grating with a motor adjusting the grating's angle relative to an exit slit. By accurately adjusting this angle, the instrument can filter out the selected photon energy desired for the current experiment. As the adjustment of this diffraction grating is mechanical, there will always be a slight error in the set photon energy. To correct for this, it has been assumed that, to a first approxiamtion, this error is linearly dependent on the set photon energy.

To approximate the dependency, the observation of a peak at a substantially higher photon energy than the set value was used, as seen in figure 4.6. This is a signal that originates from higher order light in the diffraction process, explained in section 3.7.2. In figure 4.6, the set photon energy on the instrument was 230 eV. It is seen that there are signals at 231.7 eV and 234.6 eV. These are actually the peaks from the $Mo3d_{5/2}$ orbital and the S2s. By assuming the actual photon energy to have a linear dependence with the set energy on the form $h\nu = \epsilon h\nu_{set} + c$, the energy correction factor, ϵ, can be calculated. c is a possible constant energy off-set. By observing the shifts in the energy centers of the $Mo3d_{5/2}$ when changing the photon energy one can estimate the correction factor.

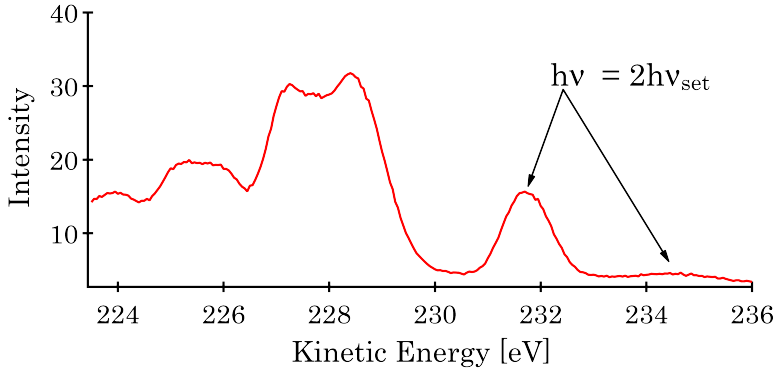

Figure 4.6: Measured spectra close to the fermi edge with a photon energy of 230eV. Two peaks well above this is from the $Mo3d_{5/2}$ and S2s excited from second order light in the diffraction process (460eV).

The observed kinetic energy center of the $Mo3d_{5/2}$ signal in figure 4.6, is 231.7 eV. From a measured spectrum at a set photon energy of 400 eV the same signal appears at an energy of 171.9 eV. The binding energy referenced for this core level in literature is 227.9 eV [43]. This yields an effective deviation from the reference energy of 0.4 eV and 0.2 eV at the two respective photon energies. From this one can derive the two relations

$$229.6\text{eV} = \epsilon \times 230\text{eV} + c \qquad 399.8\text{eV} = \epsilon \times 400\text{eV} + c. \tag{4.2}$$

By solving this a linear approximation to the effective photon energy is found to be

$$h\nu = 1.001176 \times h\nu_{set} - 0.67. \tag{4.3}$$

SECTION 4.8 k-space orientation

As stated in section 5.2.2, the 2D detector on the instrument at NTNU allowed a scan range of $k_x = \pm 0.14\sqrt{E_k}$. The experiments were conducted using a HeI_α emission line producing a photon energy of 21.22 eV. This results in a scan range of $\pm 0.58\text{Å}^{-1}$ at the fermi level, and decreases with increasing binding energy in the probed system.

Figure 4.7 shows a LEED image from one of the experiments conducted in the lab at NTNU. The hexagonal lattice structure is self dual, meaning the symmetry in reciprocal space and real space are the same. As a result it is easy to believe that the observed hexagonal structure is the actual brillouin zone of the sample. This is not the case as this is the reciprocal space projection of the crystal lattice. The real brillouin zone can be found from this by constructing the area closer to the origin of the reciprocal lattice than they

are to any other reciprocal lattice points. The high symmetry points are then located on the corner and edges of this area. Notice from figure 4.7 that the sample is oriented with a slight angular off-set. As the analyzer disperses in the $\vec{k_x}$ momentum direction, the sample can be rotated to reach a point where the slice aligns with the M-point. The rotation angle needed can be calculated by solving

$$\theta = \sin^{-1}(\frac{k_y\hbar}{\sqrt{2m_eE_k}}) \tag{4.4}$$

where, in the case when the UV-source energy is 21.22 eV and the recriprocal distance being $\Gamma M = 1.14\text{Å}^{-1}$, the sample rotation needed is approximately 30°.

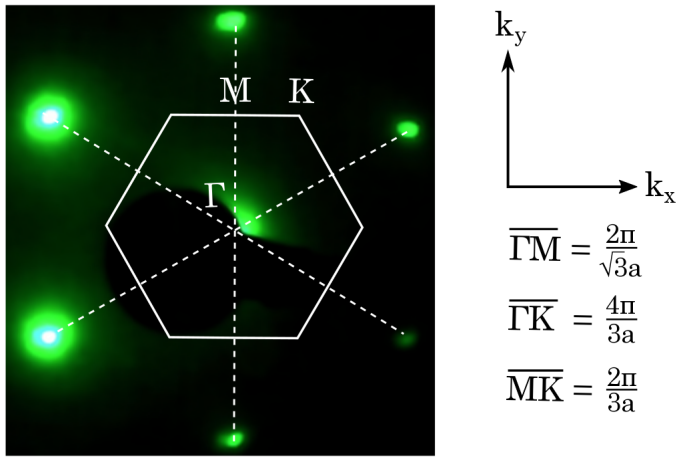

Figure 4.7: Constructed HCP brillouin zone from the observed crystal lattice on a LEED image. The brillouin zone is constructed as the area closest to a given center (Γ-point). Here also depicted with the distances between the high symmetry points. a is the lattice constant, which for MoS_2 is 3.17Å.

SECTION 4.9 Data Modeling

Fitting models to the acquired XPS raw data was done using Igor Pro version 6.37. Six algorithms were made to fit the data from the six scenarios of interest:

1) Molybdenum before dysprosium deposition

2) Molybdenum after dysprosium deposition

3) Sulphur before dysprosium deposition

4) Sulphur after dysprosium deposition

5) Dysprosium 4d

6) Dysprosium 5p

For molybdenum before and after deposition, measurements were done at binding energies ranging from 223.5eV to 236.5eV with a photon energy of 400eV for maximizing the photoionization cross-section. In this energy range, reference literature indicates that three signals will be present; $Mo3d_{\frac{5}{2}}$, $Mo3d_{\frac{3}{2}}$ and S2s. When doing curve fitting iterations, the model presented in section 3.3.3 is used with binding energy from literature as a starting point for the center of the peak. Taking into account that the Mo3d peaks are spin-coupled, the area ratio between them is set to 2:3 along with the energy splitting of 3.2eV [43] as a restriction in the model. The Mo3d peaks are allowed to have different Lorentzian widths as crystal field theory in addition to possible super Coster-Kronig transitions states that there is a difference in the core-hole lifetime in the two different orbitals. As a result the, Lorentzian width of $Mo3d_{\frac{5}{2}}$ should always be narrower than of $Mo3d_{\frac{3}{2}}$.

After deposition of dysprosium, a new model is adapted since the change in the chemical environment could induce the presence of a new molybdenum component with a shift in binding energy. This is modelled with a new set of Mo3d peaks, still restricted by the 2:3 ratio and the SOC-splitting, but with a new peak center/binding energy. According to Hesse *et al.* [29]; chemical, structural and electronic inhomogenities in the surroundings of the emitting atom may contribute to Gaussian broadening. The Gaussian component is therefore allowed to vary slightly in this case. Inspection of the acquired spectra after deposition usually gives a good indication of whether the shift is to lower or higher binding energies, and a qualified estimate is used as a starting point when modeling.

For sulphur before and after deposition, measurements were done at binding energies ranging from 157.5 eV to 170.5 eV to measure the S2p doublet. A photon energy of 230 eV was chosen to maximize the photoionization cross-section. In this energy range, reference literature indicates that two signals will be present; $S2p_{\frac{3}{2}}$, $S2p_{\frac{1}{2}}$. As for the molybdenum modeling, binding energies from reference literature is used as a starting point for the model allowing for some small deviations as the presence of contaminants migth give rise to a chemical shift. The p-orbital is also affected by SOC and the area ratio of the two peaks is restricted to 1:2 with a SOC-splitting of 1.1 eV[43]. From section 3.3.2 one should think the possible Coster-Kronig transitions could effect the Lorentzian contribution. D. Coster and R. Kronig suggest in Ref. 26 that the effect should be very small for elements below Z=40. Nevertheless, Nyholm *et al.* [49] have observed Coster-Kronig broadening for elements Z=20-30, but no literature found supports the existence of this effect in sulphur. In the modeling it is therefore assumed that the Lorentzian contribution to the sulphur signal should be the same for both peaks.

Same as for molybdenum, after dysprosium deposition the new model includes a new set of shifted sulphur signals still restricted by the split of 1.1 eV and ratio 1:2. In addition

to this, reference spectra for Dy [50] suggest there could be signals appearing around the middle of the S2p doublet, but this is disregarded in the Århus measurements as the deposited film is only a few monolayers, in addition to the fact that the cross-section of the Dy4d minimal at the photon energy used. In measurements at NTNU it is included with the restrictions from before for the other peaks, and the parameters for the dysprosium component is allowed to float (Except for μ and Gaussian width) to increase the quality of the fit.

Modeling the dysprosium signals is more of a challenge as there are several spectral features present due to various loss mechanisms. Figure 4.8 depicts the Dy4d core level measured on a sample where dysprosium was deposited until all other signals were completely attenuated. This scan should thus be similar to that of bulk dysprosium. The region extending from 165-145 eV was then modeled as four separate components, all contributing to the total Dy4d signal used in the layer modeling. As there are shortcomings in the available literature regarding dysprosiums XPS spectra, the components have unknown values for the spin splitting. Thus, when modeling the 4d spectrum all of the components are treated independently.

The Dy5p orbital was only acquired at the XPS lab at NTNU. As there is no recorded spin splitting for this core level, it was allowed to float within reasonable boundaries. The X-ray data booklet [43] states that the binding energy of the 5p orbital is 26.3eV. An additional component was found in the measured 5p spectrum and was modeled as an independent component that was assumed to be either a chemically shifted O2s component or a plasmon loss peak of the 5p itself.

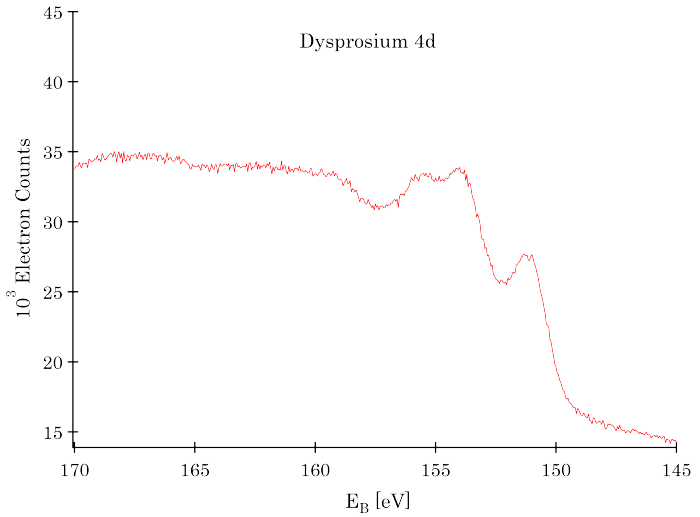

Figure 4.8: Measured Dy4d orbital on a MoS_2 sample after deposition until total attenuation of all other signals. Used as reference of a clean bulk dysprosium signal. Signal was modeled as four individual components.

The background from each peak is modelled as a Shirley background. In fitting algorithms, one usually separates between a static and an active background. In active backgrounds the intensity is optimized during the fitting process, simultaniously as the peaks are assessed. The static method refers to subtraction of the background from the original data before performing curve fitting algorithms [51]. A static approach might yield a simpler curve fitting process, but at the risk of losing important spectral information about the peaks, thus an active approach was chosen in this case.

Chapter 5

Results

The following chapter presents the results from the experiments conducted at the ISA synchrotron facility at the University of Århus, Denmark, and results from the XPS lab at NTNU. As the results are presented, an interpretation is included of the results independently. In chapter six, the scope is widened with the results being compared in more detail. The synchrotron experiments are further divided into three subsections where firstly the temperature dependency of the sulphur content is assessed for two samples with different overlayer thickness. The next section presents ARXPS data obtained from a sample deposited with 2-3 monolayers of dysprosium and a resulting modelled stoichiometry. Lastly, the samples' reaction to oxygen exposure are presented. The measurements done at NTNU are divided into two parts whereas the first contains the results from ARXPS on a sample with a thicker overlayer and the final section presents the band structure change by means of ARPES.

SECTION 5.1 Synchrotron Experiments

5.1.1 Sulphur Content Temperature Dependence

The experiment was divided into two parts. One where the goal was to observe the sulphur reaction with dysprosium on a relatively thin film of a few monolayers of dysprosium ($\approx$ 0.6 nm), and the other on a film thickness between 2 and 3 nm. As there is uncertainty as to what temperature is required for this reaction to happen, the sulphur intensity was measured as a function of temperature. The sample manipulator was cooled down with liquid nitrogen and subsequently heated in tempreature steps of $\sim 50^{\circ}\mathrm{C}$.

Thick Film

Figure 5.1 shows the measured spectra of the molybdenum 3d and sulphur 2p core levels before and after deposition of dysprosium. As there was no measureable signal from either after deposition, a steady evaporation rate of $0.15 \pm 0.2^{\mathrm{nm}}/_{\mathrm{min}}$ was assumed, calculated from the calibration sample. The thickness of the deposited film in this experiment should then be between 2.6 and 3.4 nm thick.

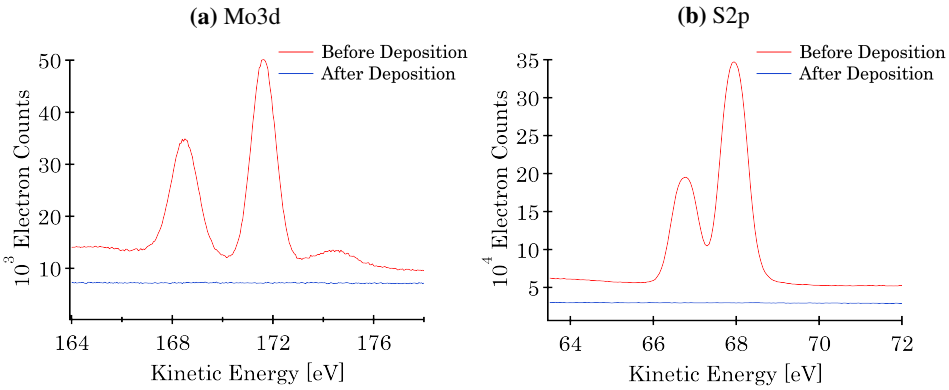

Figure 5.1: Measured Mo3d and S2p signals before and after deposition of ∼3 nm dysprosium. Spectra acquired at $h\nu = 230$ and 400eV for the S2p and Mo3d, respectively. Deposition was performed at a sample temperature of $-146°\mathrm{C}$. Previously calculated deposition rate suggests an overlayer thickness of around 3nm.

Figure 5.2 displays the experimental results of the measured S2p core level by XPS at different sample temperature stages. The strong increase of the signal as the temperature rises is a clear indication of the sulphur segregating towards the material surface. Appendix B shows the Mo3d, Dy4d and C1s spectra at different temperatures and none of these shows similar traits to that of the sulphur. One might notice the increasing carbon signal that can come from the increased contamination as the sample was kept at low temperature over a longer period. It is also a known trait that contaminats in natural crystal samples might segregate towards the sample surface as a result of a heat treatment. Furthermore, the S2p was modelled and the total intensity coming from the sulphur was plotted as a function of the sample temperature. This can be seen in figure 5.3. As depicted, the chemical reaction has not reached saturation at 350°C, meaning there is still a question wether or not this is a self-limiting process. Nevertheless, it has been shown that deposition of certain material overlayers can mediate certain growth mechanisms and yield epitaxial growth of interesting strucures [52, 53]. Results from previous experiments however indicate that rather than mediating a form of sulphur growth, the deposited dysprosium reacts chemically and potentially forming a sulfide structure. Amongst the possible sulfides (DyS_2, Dy_2S_3, Dy_3S_4 and DyS [54]), the sesquisulfide has proven to be the most stable and therefore the more experimentally researched material [55, 56].

If the observed chemical reaction is indeed the process of making a dysprosium sulphide,

one can presume that when depositing a thick film exhibiting bulk-like properties, then the reaction should saturate when the Dy_2S_3 is formed as this is the most stable compound.

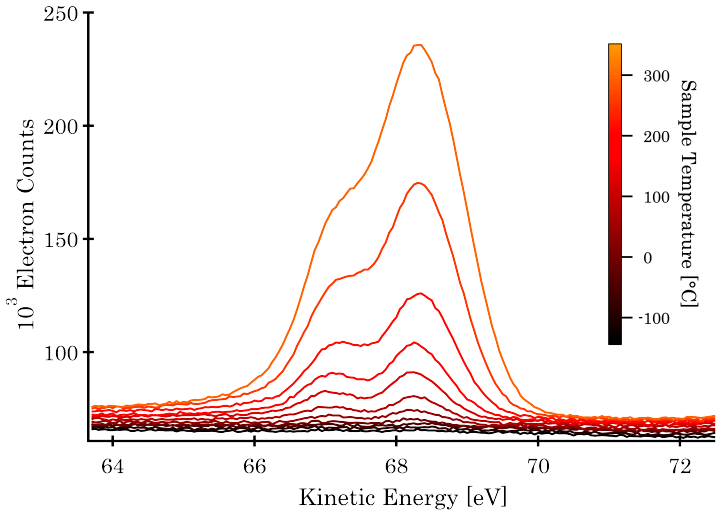

Figure 5.2: Measured S2p spectra at sample temperatures from -146°C to 350°C. After deposition at -146°C the sulphur has been completely attenuated, which is to be suspected given the high surface sensitivity of the instrument. The signal then starts to increase rapidly from 50°C and onwards.

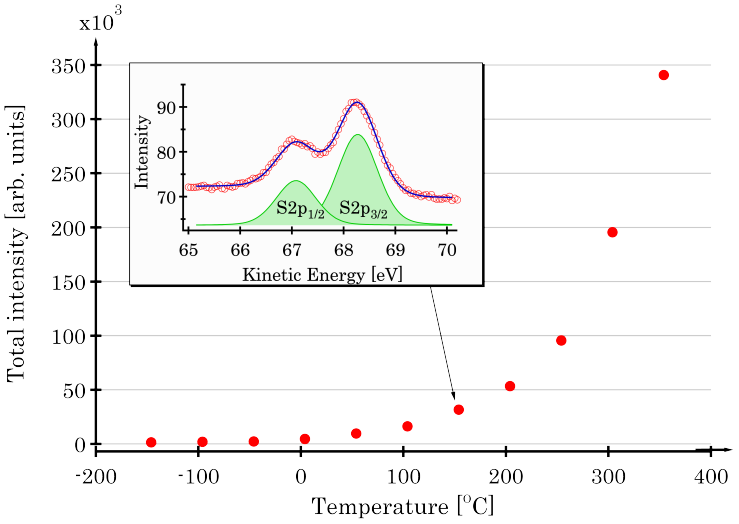

Figure 5.3: Total S2p intensity measured as a function of sample temperature. Maximum temperature was kept below 400°C as a broadening of the lorentzian contribution of S2p have been observed at higher temperatures, which might suggest a second chemical reaction. The inset frame displays the deconvoluted S2p spectra, resulting in the calculated total intensity.

Thin Film

Figure 5.4 contains the measured Mo3d and S2p spectra after deposition of approximately 0.6nm of dysprosium on the sample. As opposed to the thicker film, the sulphur in the sample with this thin overlayer does not exhibit the same steady increase with temperature. In figures 5.5 and 5.6 the acquired S2p spectra at different sample temperatures and the total intensities from the deconvolution are presented. An interesting feature is seen at a sample temperature of 150°C where the total sulphur amount drops and then proceeds to increase gradually. In figure 5.5 this is seen as the point where the left shoulder of the S2p spectrum that was gradually decreasing, suddenly starts to reappear at higher temperatures. This could be an indication of reemerging S2p signal from the S-Mo bonds that could be increasing as a result of dysprosium intercalation into the MoS_2 structure, or a possible secondary chemical reaction. The first theory is further supported by the gradually increasing molybdenum signal and the subtle, but noticeable, decrease of dysprosium as can be seen in appendix B. There is also a noticeable increase of carbon on the sample as the temperature increases, and this would also explain the screening of both sulphur and dysprosium, but not the reemerging molybdenum.

Another possible explanation might also be surface reconstruction as a result of the sample being annealed to higher temperatures, as has been seen in other rare earth films containing Lanthanum or Erbium [57, 58]. There was no recorded LEED images from this experiment to further support this theory, but indications of this have been seen in previuous experiments [59]. In addition, an example of surface reconstruction as a result of annealing on a similar sample can be seen in section 5.2.2.

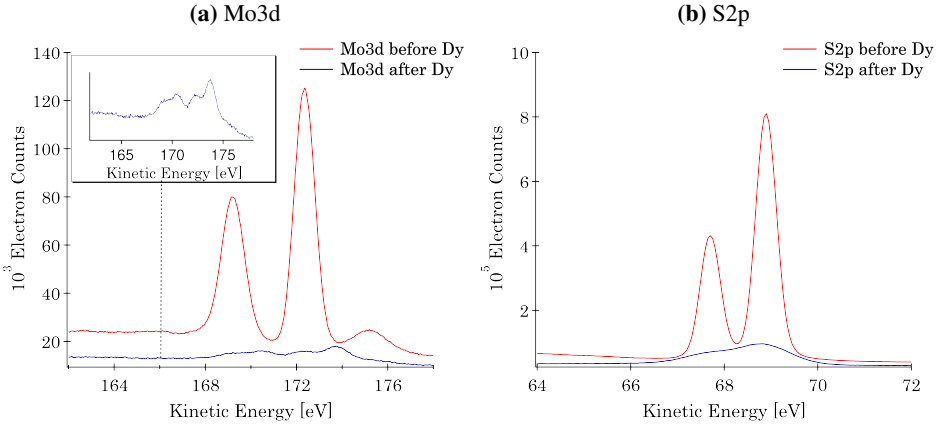

Figure 5.4: Measured Mo3d and S2p singals before and after deposition of ≈0.6 nm dysprosium. Spectra acquired at $h\nu = 230$ and 400eV for the S2p and Mo3d, respectively. A zoomed in window of the Mo3d after deposition is added to better depict the spectral features. Deposition was performed at a sample temperature of -134°C.

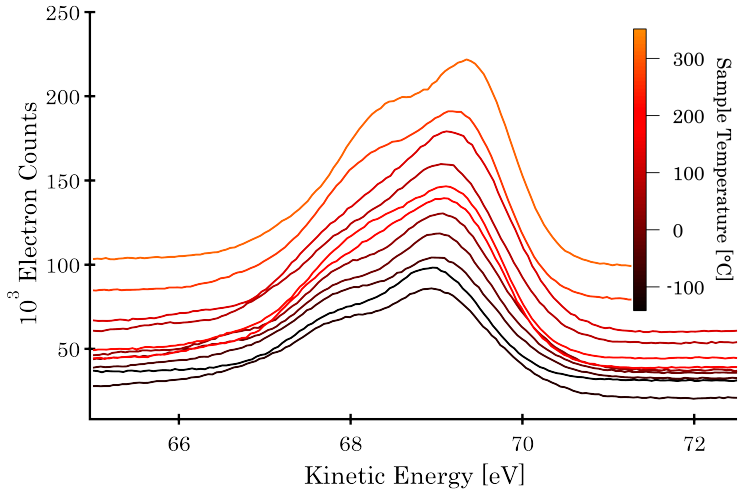

Figure 5.5: Total S2p intensity measured as a function of sample temperature. Maximum temperature was kept below 400°C as it had been previously observed a broadening of the lorentzian contribution of S2p at higher temperatures, which might suggest a second chemical reaction. It is noted that the left shoulder of the S2p is decreasing as the sulphur shifts toward the S-Dy bonding.

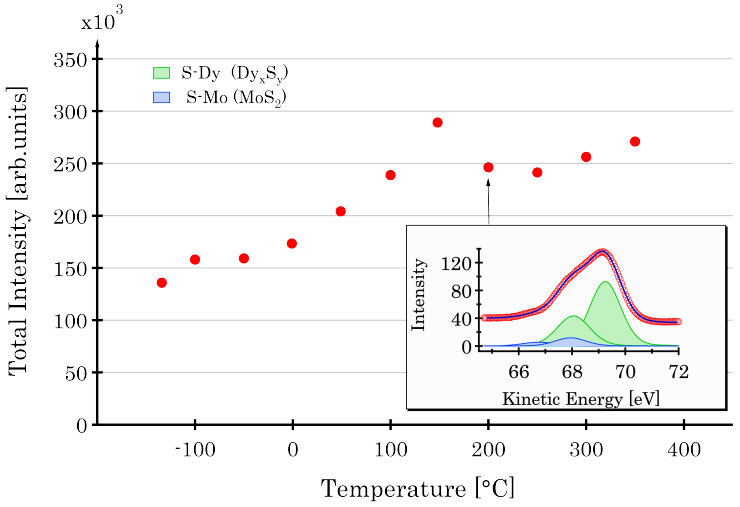

Figure 5.6: Total S2p intensity measured as a function of sample temperature. Maximum temperature was kept below 400°C as it had been previously observed a broadening of the lorentzian contribution of S2p at higher temperatures, which might suggest a second chemical reaction. Notice the irregularity at 150°C which is also the temperature at which the left shoulder starts to reappear in the S2p signal. This might indicate dysprosium intercalation which is further supported by the slightly reappearing molybdenum signal as seen in appendix B.

5.1.2 ARXPS and Layer Modeling

Previous experiments had shown indications of surface reconstruction into hexagonal symmetry in the dysprosium sulfide after heating the sample to 300-350°C. This was however only observed if the deposited Dy film was sufficiently thin (2-4 monolayers) [59]. It may be the case that with thicker dysprosium layers the sesquisulfide conformation is preferred as this is known to be the most stable in bulk. As Dy_2S_3 has been proven to exist in three different crystal structures (Orthorombic, monoclinic and cubic) [60], and most monochalcogenides of the f-block adopt the NaCl structure [54], it is believed that the dysprosium sulphide is of an other character, such as DyS or DyS_2.

Figure 5.8 shows the evolution of the Mo3d, S2p and Dy4d spectra at different emission angles. The slight deviations at -5 and 10 degrees emission might indicate a non uniform overlayer or a surface artifact. A possibility is also that what is believed to be normal emission is not really at true zero. Modeling the layer stoichiometry was done by propagating the models depicted in appendix C through the angle series to obtain the total signal for the respective elements. After normalizing the spectra for their respective photoionization cross-sections, number of scans done and the approximated transmission function, the relative intensities of the three elements could be extracted.

The two S2p components, suggested to arise from Mo-S and Dy-S bonds, are plotted relative the total signal in figure 5.7. Also included, are the simulated relatives of the Mo and Dy. One can observe a general agreement in the increase of the Dy-S and simulated Dy, and the decrease of Mo-S and simulated Mo, for higher angles. Still, the ratio between Mo and the sulphur component from the Mo-S bond, well exceeds 2. Thus, indicating that separating the components is not trivial.

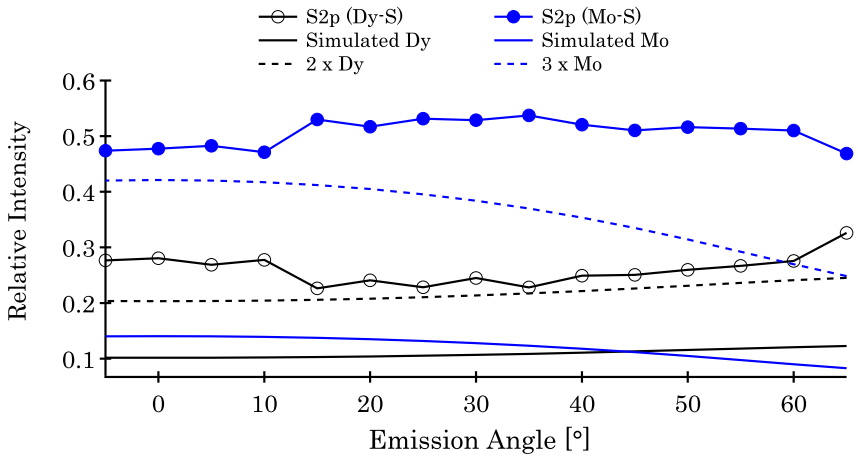

Figure 5.7: Extracted S2p components from the fitting process. Here comparing the relative Mo-S and Dy-S component to the simulated Mo and Dy from the layer model. The dotted lines indicate the simulated values multiplied for easier comparison of ratio.

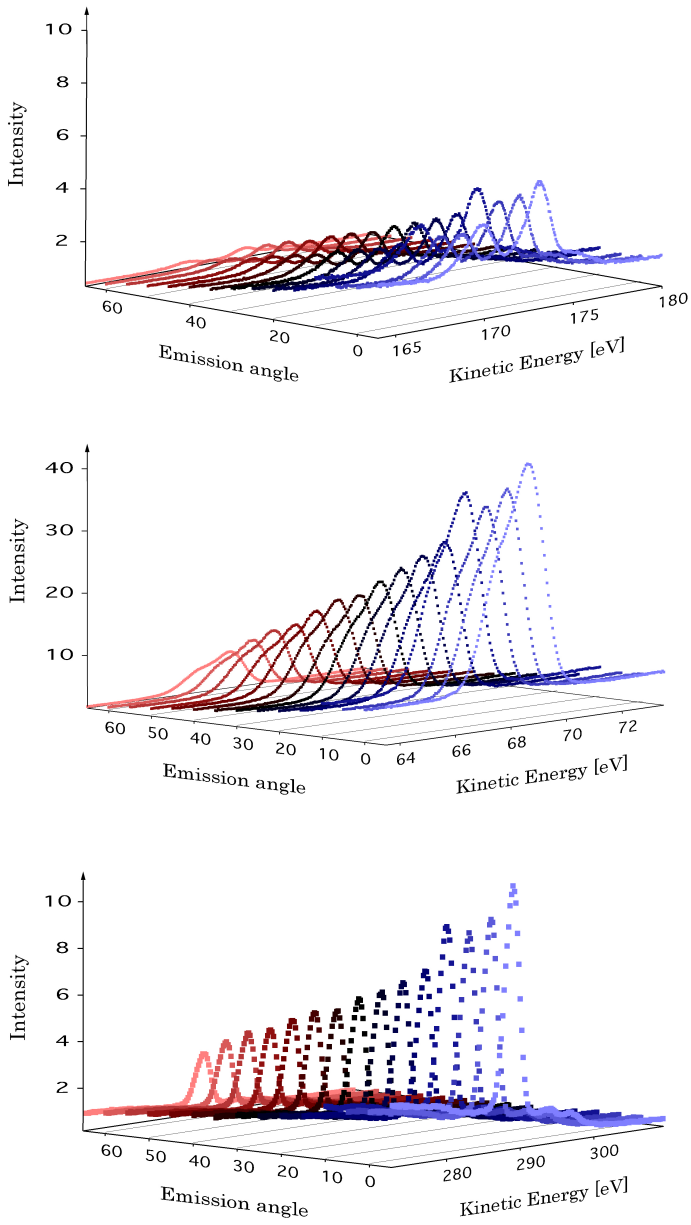

Figure 5.8: Acquired ARXPS data for the Mo3d, S2p and Dy4d core levels from top to bottom. Measurements were done at emission angles from -5° to 65°. Notice the deviations at -5° and 10° indicating that maybe normal emission is not at true zero, or that the deposited layer is not uniform.

In figure 5.9, the relative intensities can be seen as a function of incoming emission angle including the simulated relatives coming from the layer model seen in figure 5.10. Modeling the stoichiometry was done using the finite layer model along with the principle of maximum entropy presented in section 3.3.3. The layer thickness in the model was chosen to be half of the MoS_2 unit cell with four layers included in the model. The layer thickness is in this case not a critical parameter as the surface-sensitivity to the deeper-lying layers is small due to the short electron mean free path. The layer model (fig. 5.10) reveals that the surface is sulphur rich. The fact that there is a small molybdenum signal in the first layer, indicates that the deposited amount of dysprosium should be sub 0.6 nm. As for the relative abundance, the calculated values are shown in table 5.1 and indicate almost half the amount of molybdenum compared to dysprosium in the first layer. The amount of sulphur signal in the first layer that comes from the MoS_2, is twice this amount. The rest should then belong to the dysprosium sulphide compound. This roughly yields a ratio Dy:S of 1:5.

Table 5.1: Relative concentration of elements in each layer in the layer model presented in figure 5.10, C_i.

Element	C_1	C_2	C_3	C_4
Mo	0.07	0.32	0.26	0.26
Dy	0.13	≈ 0	≈ 0	≈ 0
S	0.80	0.67	0.74	0.74

As to why this ratio favours the sulphur to this extent can come from several factors. Still, it is believed that the model for the Dy4d core level is undermining the dysprosium, and that some of the spectral features assigned to sulphur in reality contains Dy. It is seen from the included standard deviations from the curve fitting procedure that the error from the Dy4d model is quite large compared to the other two core levels modelled, and should thus be regarded as a critical source of uncertainty in these calculations. The complexity of the Dy4d combined with the sulphur reactivity suggest that this orbital may not be the best suited for achieving proper quantification. Also, the measurements were all done at quite low electron energies, where the decay in the transmission function is steepest, which should be regarded as a source of error in these estimations.

Even though there is a substantial degree of uncertainty regarding the calculated relative concentrations, the results strongly indicate that for sufficiently thin films, as the one deposited here, the reaction between sulphur and dysprosium occurs even without a subsequent anneal after deposition. This is also supported by the findings in section 5.1.1, where quite a large increase in the sulphur signal occurs as the sample temperature is increased from -134°C towards room temperature. Another observation is that the model includes small Dy concentrations in the lower layers of the sample. One could regard these as intercalants of dysprosium, but as these concentrations are defined from the third decimal, it is well within the uncertainty of the model. Thus, it should not be regarded as solid proof of intercalation. Nevertheless, when observing this together with the findings in 5.1.1, it is possible that some intercalation is taking place in the sample.

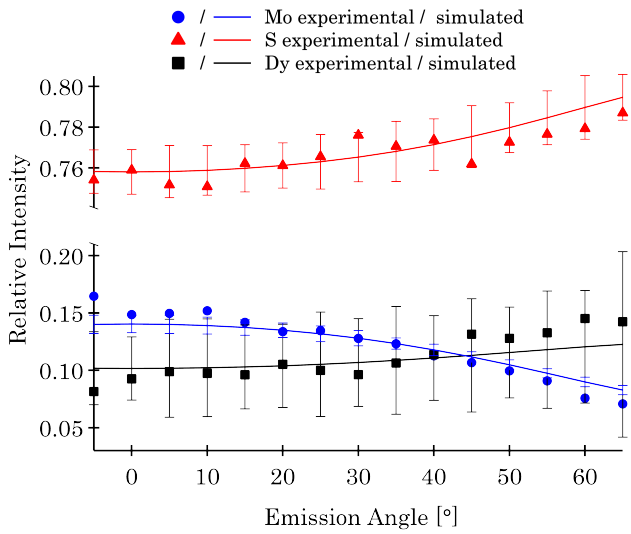

Figure 5.9: Normalized intensities of the Dy, Mo and S core levels (black, blue and red data points) as a function of emission angle. Simulated intensities from the layer model are included as solid lines of matching colors. The error bars show the standard deviations from the modelled intensities.

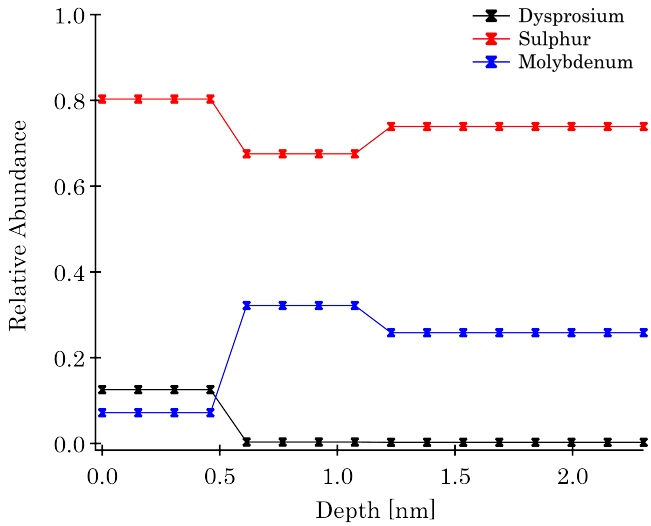

Figure 5.10: Modeled layer-by-layer stoichiometry of a depth corresponding to 2 unit cells of molydenum disulphide. Dy(black), Mo(blue) and S(red) quantities are normalized such that the sum at any sample depth equals to unity. Attenuation lengths of the respective core levels has been chosen as $\lambda_{Dy5p} = 0.55\text{nm}$, $\lambda_{Mo3d} = 0.45\text{nm}$ and $\lambda_{S2p} = 0.35\text{nm}$.

5.1.3 Oxidation and Chemical Stability

Dysprosium is known to oxidize very easily. Interesting results are seen of its reactivity depending on the current chemical environment. In figure 5.11, the Dy4d region is measured for both a film of thickness 2-3 nm and 2-3 monolayers. The thick film was not annealed after deposition and it was believed that a possible sulphur reaction will only occur at the interface between the substrate and the overlayer. The thinner film was annealed to 300°C, and thus believed to have formed a sulphide compound. The most interesting trait seen in the Dy4d peak for the thicker, unreacted film, is the shift towards higher binding energy after introducing oxygen into the vacuum. The appearance of a weak signal around 182 eV binding energy is also noted. Both these observations are consistent with the findings in the XPS analysis done by Barreca *et al.* [61] on Dy_2O_3, meaning there is reason to believe that a dysprosium oxide is forming. On the thinner film the dysprosium signal is relatively weak, but a slight shift towards lower binding energy is still seen, suggesting a completely different reaction.

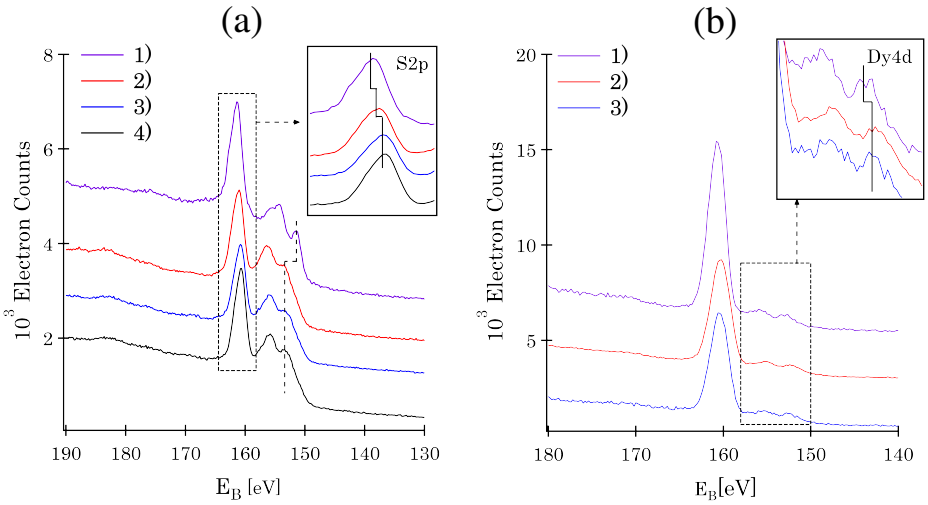

Figure 5.11: Measured Dy4d core level during an oxygen treatment of two different samples. **(a)** depicts a sample with dysprosium overlayer thickness of 2-3nm in four steps: **1)** As deposited at room temperature, **2)** After oxygen dosing for 10 minutes, **3)** 150°C annealing and **4)** 300°C annealing. **(b)** depicts a sample with an overlayer of 2-3 monolayers in three steps: **1)** As deposited and annealed to 300°C, **2)** After oxygen dosing for 10 minutes and **3)** secondary anneal at 300°C. The spectra have been given an intensity off-set for better comparison.

The formation of an oxide in the thick film is further supported by the observations in figure 5.12, which shows the measured oxygen-1s core level before and after heat treatments. In 5.12 (a), the measured spectra for the oxygen on the thicker film suggests oxygen in two different environments. The deconvolution yields one component at $E_B = 531.7$eV and another one at $E_B = 529.2$eV. Oxygen-1s signals around the binding energy first mentioned are commonly attributed to O-H and O-C bonds, which may be present on the sample surface. In Ref. 61 a peak at 591.1eV was assigned to lattice oxygen in Dy(III) ox-

ide, which is consistent with the observations here. However, literature is controversial, as both higher [62] and lower [63] values of the binding energy compared to the present one have been observed. An interesting trait seen is that when annealing the sample at 150°C and 300°C, almost all the oxygen shifts towards the binding assigned to the dysprosium oxide. After the last anneal, the total oxygen amount has decreased by 11% and the rest has all been shifted to lattice oxygen of Dy(III) oxide.

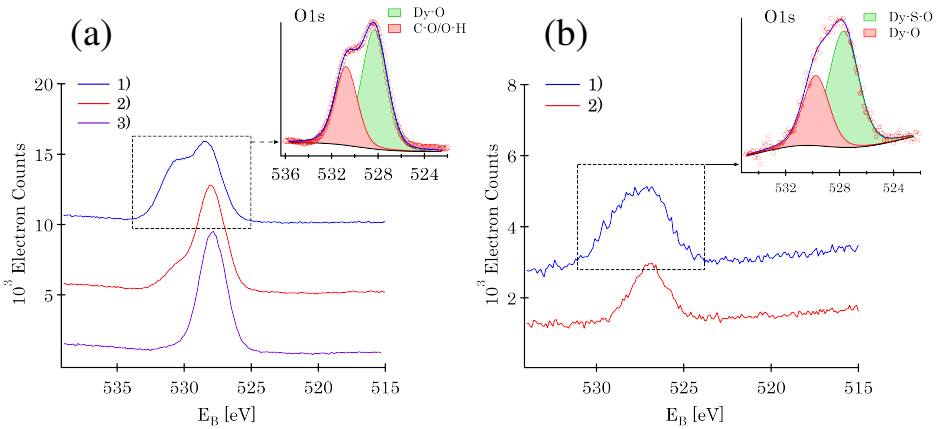

Figure 5.12: Measured O1s core level during an oxygen treatment of two different samples. **(a)** depicts a sample with a non annealed dysprosium overlayer thickness of 2-3nm in three steps: **1)** After oxygen dosing for 10 minutes, **2)** 150°C annealing and **3)** 300°C annealing. **(b)** depicts a sample with an overlayer of 2-3 monolayers that was annealed before treating with oxygen. The two steps depicts the specturm: **1)** After oxygen dosing for 10 minutes and **2)** After annealing at 300°C. The spectra have ben given an intensity off-set for better comparison. The upper right corner in each figure shows the fitted and deconvoluted O1s spectra after oxygen exposure.

The oxygen-1s core levels on the sample with the thinner overlayer also contain two components. These are found to be at binding energies 529.8eV and 527.7eV. The chemical nature of these two components could be a range of combinations, but it is suggested that one component arises from a dysprosium oxide bonding, possibly from surface oxidation. The other component is believed to be that of a dysprosium oxide sulphide (Dy-S-O). In Ref. 64 the preparation of dysprosium oxide sulphides is shown to happen by, for example, mixing the sesquioxide and sesquisulphide followed by heat treatments in the range of 1300-1600 °C. This reaction results in a mixture with the general formula $Dy_2O_{2\pm x}S_{1\mp x}$. Also, the oxidation of a dysprosium sulphide has proven to produce oxide sulphides with the pure sesquioxide as a by-product. Similar to the case of the thick film, a shift of the oxygen towards the lower binding energy component is observed after annealing at 300°C. The oxygen amount after this process is then reduced by 52%. This might suggest a reaction similar to that in Ref. 64, here on the form

$$Dy_xS_y + O_2 \xrightarrow{300^\circ C} Dy_xO_zS_y + \text{side products} \tag{5.1}$$

The S2p core level shown in figure 5.13 also indicates different reactions occuring in the

two samples. In both samples the sulphur separates into two separate components after the oxygen treatment. After Dy deposition, the sample with the thicker film displays two peaks seemingly from the Mo-S bonds in the substrate and possibly a component slightly shifted due to the change of chemical environment. The proceeding oxygen treatment then forces a shift of both components towards lower binding energy, which is believed to be the response of the change in chemical environment due to the starting oxidation of dysprosium. Further annealing then increases the part of the signal originating from the Mo-S bonds. In the thick film, similar traits are observed, but after annealing the sample at 300°C. The S2p divides into two different signals with binding energies for the $S2p_{3/2}$ at 159.9eV and 161eV from the proposed dysprosium sulphide and dysprosium oxide sulphide. A subsequent anneal at 300°C produces an increase of the oxide sulphide component, but still a substantial amount of the pure sulphide signal seems to be intact, which may be an indication that higher temperatures are needed for a full reaction.

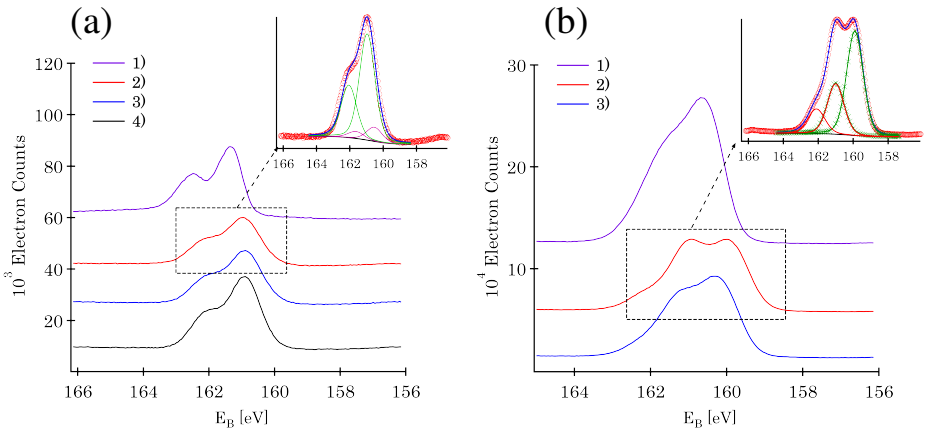

Figure 5.13: Measured S2p core level during an oxygen treatment of two different samples. **(a)** depicts a sample with dysprosium overlayer thickness of 2-3nm in four steps: **1)** As deposited at room temperature, **2)** After oxygen dosing for 10 minutes, **3)** 150°C annealing and **4)** 300°C annealing. **(b)** depicts a sample with an overlayer of 2-3 monolayers in three steps: **1)** As deposited and annealed to 300°C, **2)** After oxygen dosing for 10 minutes and **3)** secondary anneal at 300°C. The spectra have ben given an intensity off-set for better comparison. The upper right corner in each figure shows the fitted and deconvoluted S2p spectra after oxygen exposure.

Lastly, XPS measurements of the valence band edges for the two samples are shown in figure 5.14. Here, the subsequent annealing treatments do not appear to change the electronic structure in any of the samples. The small shifts in the valence edge are most likely due to movements in the monochromator between the different measurements. Still, the two scans show differing characteristics, but one has to keep in mind that the measurements here are done at different photon energies. The edge in the sample with possible pure dysprosium oxide is observed to be close to 2 eV binding energy, suggesting a wide gap with possible insulating properties. The referenced binding energies of the dysprosium 4f-orbitals for a pure sample is 4.3 eV and 8.0 eV. These will surely affect the observed band edges, meaning the energy of the edge should not be observed uncritically. This is

perhaps clearer in figure 5.14 (b), where two tangents are drawn on the spectral shape to depict the range where the valence band edge is suggested to be. By extracting a possible Dy4f component in the 4.3 eV area, the observed tangent intersecting around 2 eV will become more shallow and favour lower binding energies. There is also the observation of the shoulder around 2.3 eV with unknown origin; the possibility of orbital components here will favour a steeper valence band edge.

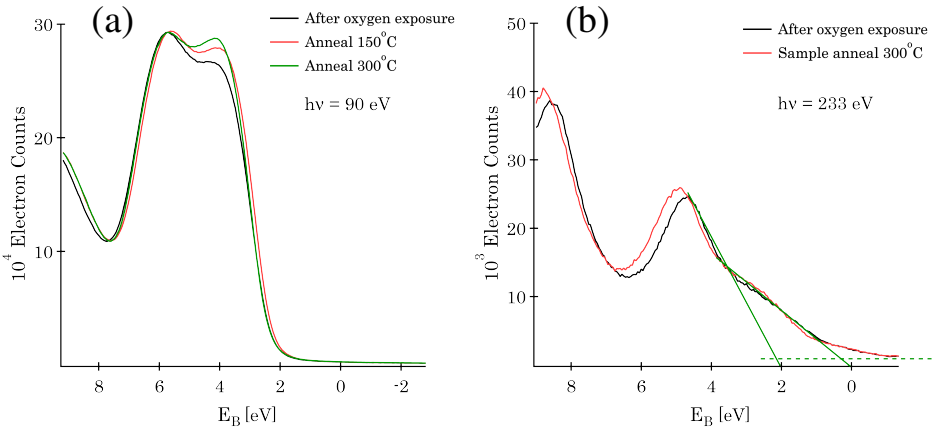

Figure 5.14: Measured valence band during an oxygen treatment of two different samples. **(a)** depicts a sample with dysprosium overlayer thickness of 2-3nm in three steps: **1)** After oxygen dosing for 10 minutes, **2)** 150°C annealing and **3)** 300°C annealing. **(b)** depicts a sample with an overlayer of 2-3 monolayers after annealing and oxygen exposure in **1)**, and after a subsequent anneal to 300°C in **2)**

SECTION 5.2

NTNU XPS-lab Experiments

5.2.1 ARXPS Dy Thick Film Deposition

A similar experiment to the one presented in 5.1.2 was performed on the XPS instrument at NTNU. In this case, the dysprosium overlayer was substantially thicker, and the layered stoichiometry was modeled before and after an annealing treatment of 300°C.

Before annealing, the molybdenum intensity was very weak and was neglected from the layer model. After annealing, on the other hand, the Mo signal became more prominent and was thus included after this step. The models used can be seen in appendix E. Note that in comparison to the thin film experiment in section 5.1, the Dy5p core level is used for the quantification. The layer model is similarily to the thin film experiment, modeled using half the unit cell height of MoS_2. The normalized simulated and experimental intensities are as shown in figure 5.15, and the modeled layer stoichiometry can be seen in figure 5.17.

The model concurs with the fact the deposited dysprosium overlayer was calculated to be between 2 and 3 nm. One notices that the model includes a non-zero dysprosium concentration in the first four layers before the anneal, and after there is also Dy in the fifth layer. This indicates intercalation in the MoS_2, leaving it slightly dysprosium doped. Also note the strong increase in sulphur concentration in the top 2 nm of the sample in combination with the sulphur decrease from the sample's deeper levels. The dysprosium is forcing the sulphur from the molybdenum disulphide to segregate towards the surface.

Table 5.2: Relative concentration of elements in each layer from the model in figure 5.17, C_i after sample annealing at 300°C.

Element	C_1	C_2	C_3	C_4	C_5	C_6	$C_7 \rightarrow$
Mo	0	0	0	0.31	0.33	0.41	0.3
Dy	0.60	0.47	0.42	0.35	0.14	0	0
S	0.40	0.53	0.58	0.34	0.53	59	0.7

Table 5.2 contains the modeled elemental concentrations in each layer. It is observed that the ratio varies between 1:1 and 3:2 in the first three layers. As the transmission function of the instruments is known in this case, this should be less of an error compared to previous experiments. Also, the increased simplicity of the Dy5p compared to the Dy4d should increase the quality of the quantification. Still, as the crystallographic nature of the compound is unknown it is quite possible that the modeled layer thickness results in a ratio that does not depict the actual compound created. For instance, if the compound had a unit cell as large as 3 times x_{layer}, the ratio would be modeled as very close to 1:1. Also the choice of electron attenuation length of the different compounds is an obvious source of error in this case. Nevertheless, LEED images from Ref. 59 and results in section 5.2.2 indicate the possible formation of a hexagonal lattice structure that cannot be the sesquisulfide. This may therefore indicate the formation of a binary dysprosium sulfide.

As seen in figure 5.16, a shift in binding energy of the $Dy5p_{3/2}$ from 23.6 eV to 24.6 eV is observed. As there is little to no literature about the observed binding energy of the possible Dy_2S_3, it is hard to exclude this as an option. Even so, the observed shift of 1eV is a clear indication of a chemical reaction rather than a binding energy shift due to change in chemical environment. Also the final binding energy of the peak i shifted by 1.7eV from the referenced binding energy of the pure bulk Dy binding at 26.3eV [43]. Additionally, the consecutive measurements made it possible to obtain enough scans of the Dy5p core level to approximate the spin splitting, where the calculated values from a series of measurements can be seen in figure 5.16. This splitting is not found to be referenced in literature but analysis of the results suggest a spin splitting of $5.67 \pm 0.01\mathrm{eV}$, where the splitting from measurement 12 has been regarded as an extremal and thus, disregarded in the approximation. The error is the standard deviation calculated from the fitting algorithm so the true error should also account for energy resolution of the measurements and other factors, meaning the true error can be closer to 50-100meV.

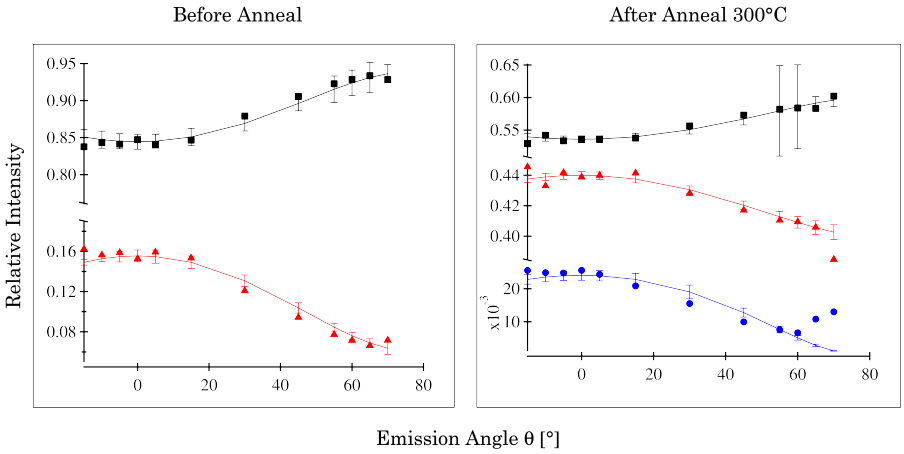

Figure 5.15: Normalized intensities of the Dy, Mo and S core levels before and after annealing at 300°C (black, blue and red data points respectively) as a function of emission angle. Simulated intensities from the layer model are included as solid line of matching colors. The error bars show the standard deviations from the modelled intensities.

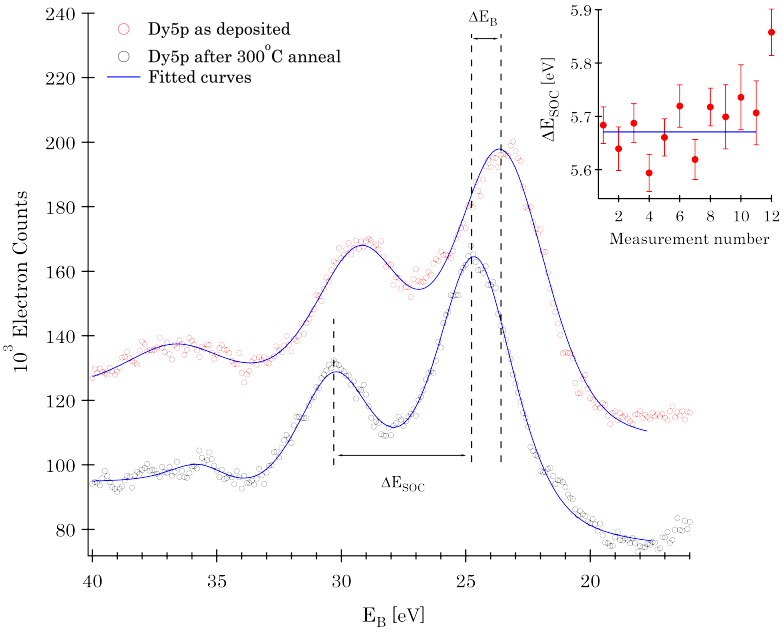

Figure 5.16: Measured Dy5p core level with MgKα anode as deposited and after annealing at 300°C. Acquired data before and after annealing are the red and black circles respectively. Blue lines indicate the fitted curves. The top right corner depicts the extracted SOC split values (red circles) from the Dy5p fitting along with a linear fit (blue line).

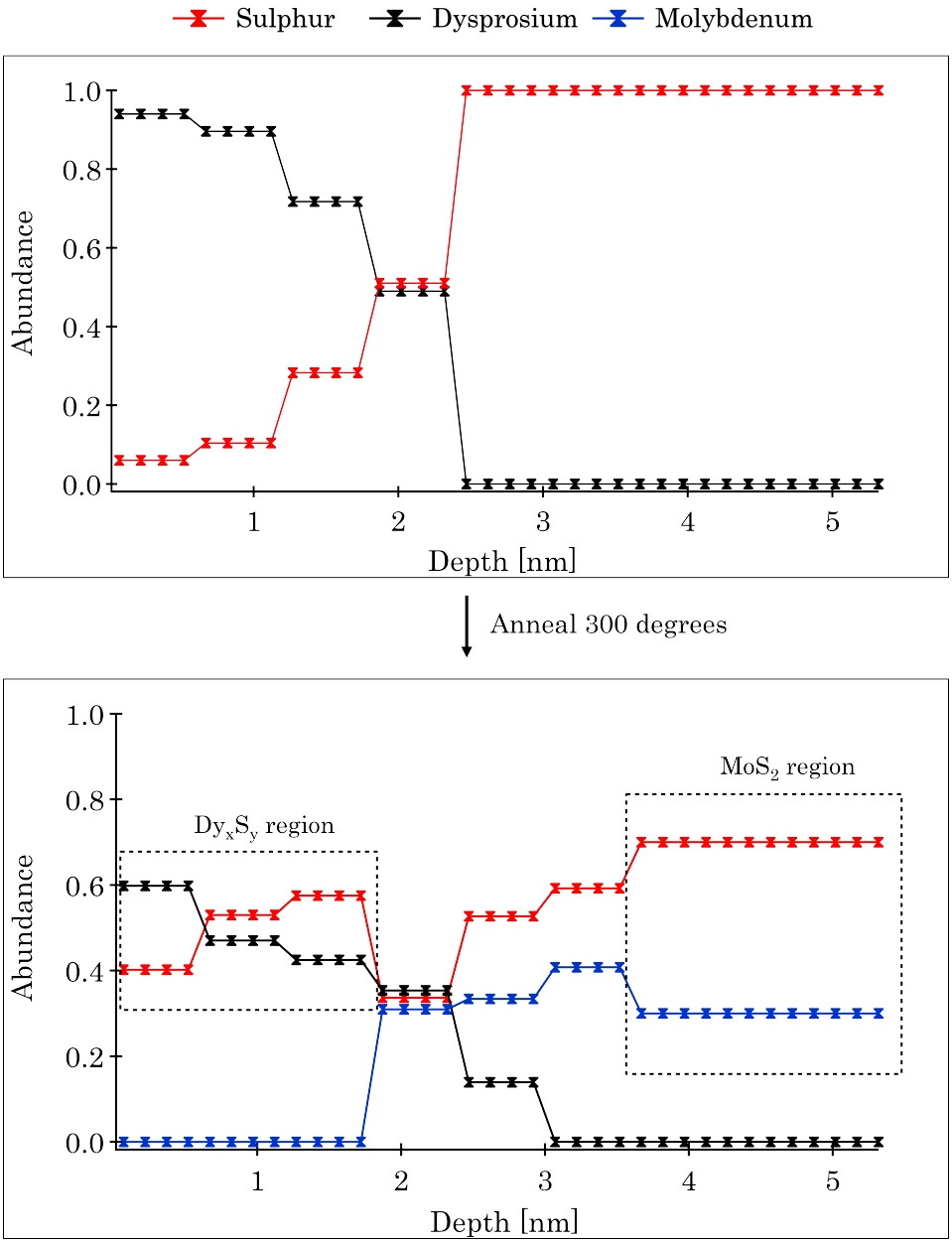

Figure 5.17: Modeled layer stoichiometry before and after annealing at 300°C. Deposited dysprosium layer was calculated to be between 2 and 3nm. Each layer is model with the thickness of half a MoS_2 unit cell. Attenuation lengths of the respective core levels has been chosen as $\lambda_{Dy5p} = 0.95\text{nm}$, $\lambda_{Mo3d} = 0.8\text{nm}$ and $\lambda_{S2p} = 0.75\text{nm}$.

5.2.2 ARPES Band Structure Measurements

The acquired ARPES data from the $\bar{M}$-point towards $\bar{K}$ of MoS_2 before deposition of Dy, is depicted in figure 5.18. This spectra conforms quite well with the DFT calculations seen in section 2.1. Due to the limitations of the UV-source's energy, the scanned range does not extend all the way $\bar{K}$. Still, one can see the distinct spin orbit coupled splitting in the band structure close to $\bar{K}$.

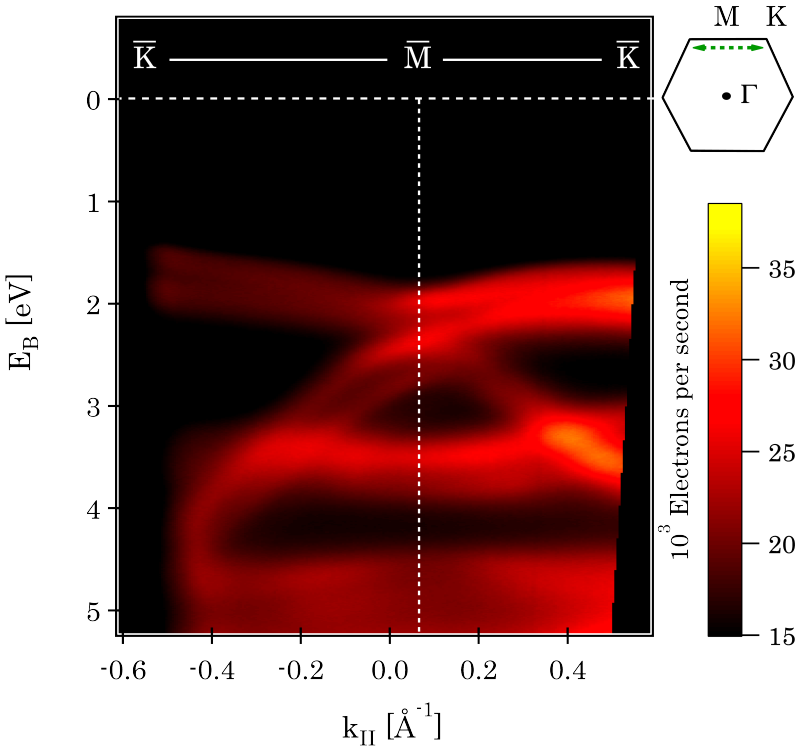

Figure 5.18: Acquired valence bandstructure of 2H-MoS_2 before deposition. Recorded along $\bar{M} - \bar{K}$ (indicated by green line on the hexagon in the upper right corner) with photon energy $h\nu = 21.2$eV. The dotted white line indicates the high symmetry point, $\bar{M}$.

Figures 5.19 and 5.20 show the extracted intensity profiles at the $\bar{M}$-point and two sizes are defined; ΔE_{MM}, and ΔE_S. The first denotes the energy gap between the VBM and the maxima of the negative parabolic band. The second defines the energy splitting of the negative parabolic band that may arise from spin polarization. The two bands that should cross at $\bar{M}$ is seen here as one, and is not apparent in the intensity profile. This is assumed to arise from a combination of lack in energy resolution of the instrument, and also band broadening due to many-body interactions, forcing the bands to appear as overlapping. After deposition, the signal of the structure weakens as a result of the strong

peaks appearing around 4.5 eV binding energy, which effectively dilutes the underlying band structure. This is presumed to be from the Dy4f states. It is also noted that the $\bar{M}$-point shifts slightly towards the center in $k_{\|}$, which could indicate a rotation of the crystal lattice. Still, a more probable explanation is the slight movement of the sample due to sample transfers between deposition and measurement, and also that the manipulator position may change slightly.

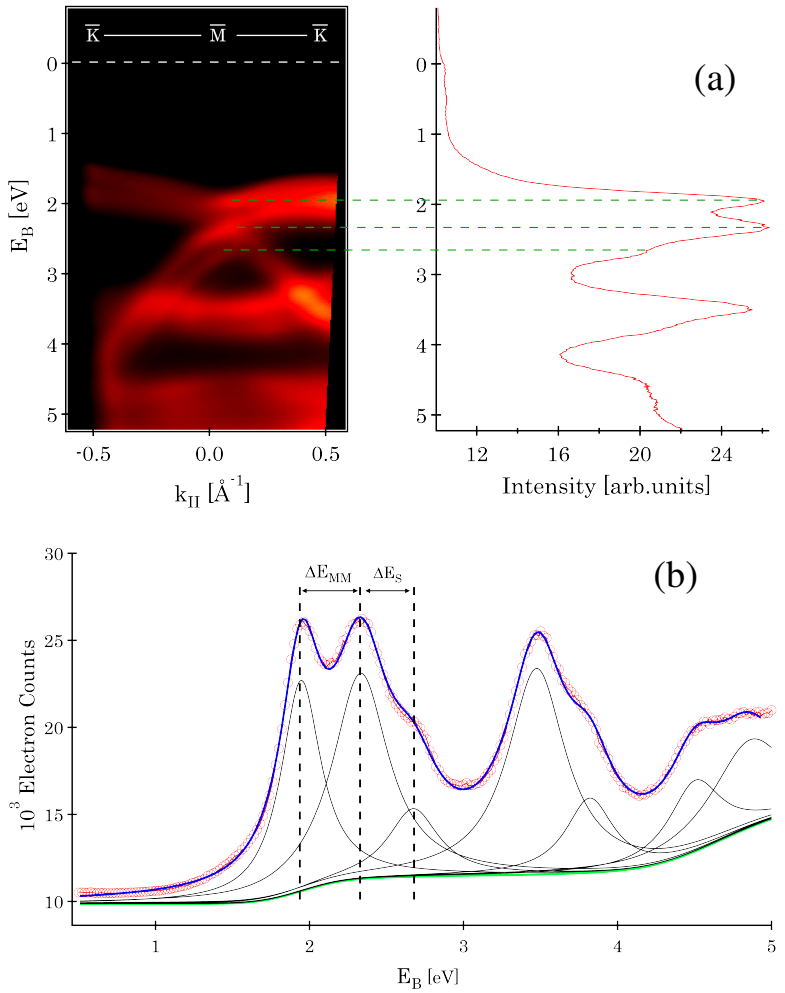

Figure 5.19: **(a)** Figure depicting the intensity profile along the M-point. Dotted green lines link the intensity peaks to the respective bands in the ARPES data. **(b)** Analysed intensity profile along M. Red circles are the experimental data and the blue line is the fitted curve. The green and black solid lines are the background and the deconvoluted peaks respectively. ΔE_{MM} is the energy gaps between the VBM and the negative parabolic band, and ΔE_S the energy splitting seen in the negative parabolic band.

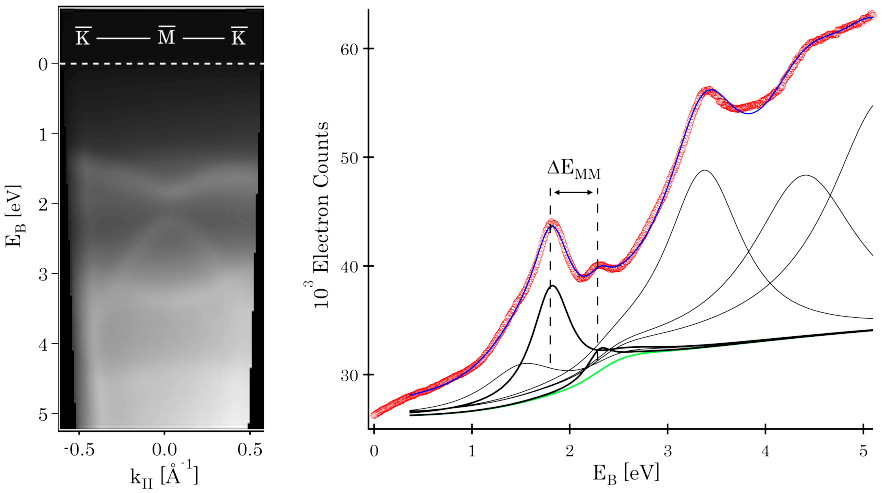

Figure 5.20: Measured $\bar{M}$-point and intensity profile after deposition of dysprosium. Red circles are the experimental data and the blue line is the fitted curve. The green and black solid lines are the background and the deconvoluted peaks, respectively. As the features are weaker after the deposition, the intensity profile is aquired by averaging profiles ± 10 points of $k_{\|}$ around what is believed to be true $\bar{M}$.

Energy values of the valence band and the negative parabolic band at different values of $k_{\|}$ including a parabolic fit, are shown in figure 5.21. The irregularity in figure 5.21 c) resulting in a non-parabolic nature, arises from the observed overlap between the valence band and the negative parabolic at around 0.2Å^{-1}. The splitting of the negative parabolic is easier distinguised at negative values of $k_{\|}$, and due to the broadening of the bands they seem to merge above 0.2Å^{-1}. Due to this, the parabolic curve fitting was done in the range that was believed to be the parabolic part of the band, and then further extrapolated.

Three substantial changes are observed after deposition of Dy. The first is the significant decrease of the VBM from 1.95eV to 1.82eV giving a ΔVBM of 130meV. Secondly, the observed splitting in the negative parabolic band seems to disappear after the deposition. Before deposition, the size of this splitting is found to be $\Delta E_S = 320\text{meV}$, and after, the band maximum of the negative parabola is at the same energy, meaning that the change in ΔE_{MM} equals the change in the VBM position. Lastly one should note the obvious change in the sharpness of the parabola in 5.21 (a) and (b). The curvature of the energy bands is related to the electrons' effective mass in a system as

$$m^* = \frac{\hbar^2}{\partial^2 E / \partial k^2}. \tag{5.2}$$

The curvature after deposition has become smaller, meaning the effective mass has increased. This could be an effect from a change in the spin polarization of the system. Enhanced effective mass in dilute 2D electron systems in silicon has been observed to be spin-independent [65], so other explanations are also possible.

It is hard to say wether this is solely caused by the reaction of the MoS_2 band structure to dysprosium doping, or if the signal originates from two sets of band structures. One from the proposed dysprosium sulphide and one from the underlying MoS_2. A third option is that the observed change in the band structure is just a proximity effect from a dysprosium sulphide with too poor crystalline quality to observe its electronic structure. As the deposited overlayer is of the size of a few monolayers and previous experiments support the formation of a dysprosium sulphide, one of the last two is assumed to be the most probable.

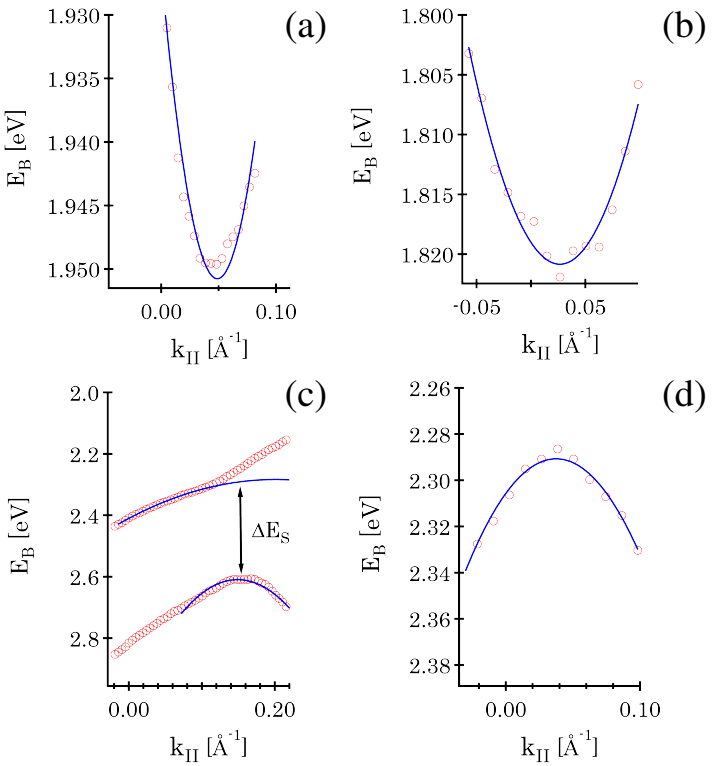

Figure 5.21: Band energies as a function of $k_{||}$ of the: **(a)** Valence band before deposition of Dy. **(b)** Valence band after deposition of Dy. **(c)** Negative parabolic band (w/split) before deposition of Dy. **(d)** Negative parabolic band after deposition Dy. Red circles are the acquired data and the blue lines indicate a parabolic fit.

Calculation of the lattice constant after deposition was done by defining the length of $2a_{MoS_2}$ in pixels from the LEED pattern from the clean molybdenum disulphide as seen in figure 5.22. By using the same scaling on the pattern after deposition and defining the ratio of the lattice constants by the bragg relation; $\frac{a_{MoS_2}}{a_{Dy_xS_y}} = \frac{\lambda(E_{bef})}{\lambda(E_aft)}$, the restructured lattice constant can be calculated. Here, $\lambda(E)$ is approximated as the de Broglie wavelength of the electron given by $\lambda(E) = \frac{h}{\sqrt{2m_eE}}$.

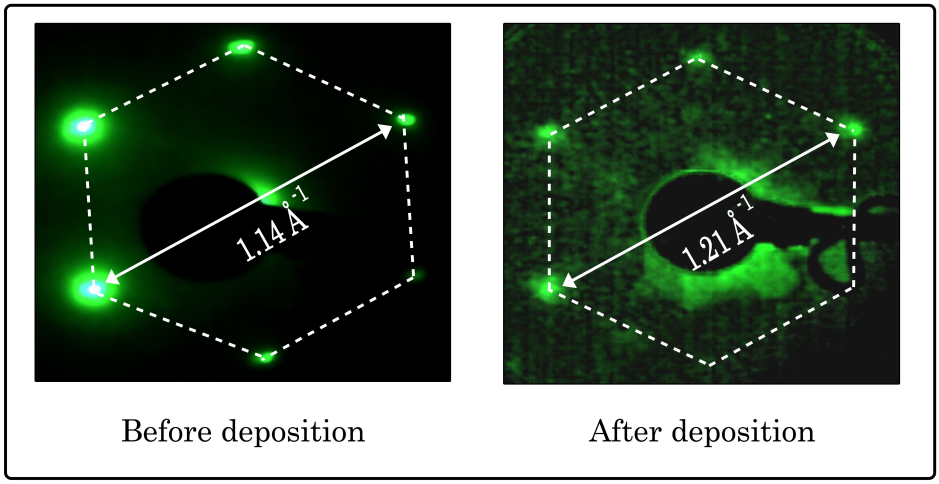

Figure 5.22: Acquired LEED images before and after dysprosium deposition (at $E_k = 93.6$ and 100.3eV, respectively) with constructed hexagonal structure. The figure includes the calculated lengths of the reciprocal lattice constant. Images have been optimized through bacground subtraction and adjustment of brightness/contrast.

There was no visible LEED pattern after deposition, but structure reappeared after annealing the sample. Analysis of the LEED patterns indicate a slight increase of the reciprocal lattice size after deposition of Dy. This is consistent with the fact that the sample rotation to reach the M-point in the ARPES measurement after deposition, meaning the size of the brillouin zone, increased. However, the subtle change from $a = 3.17$Å to $a = 3.10$Å is within the error of the measurement. Thus, the size of the lattice should be regarded as constant. Lattice mismatch of a deposited material and the substrate will often lead to a rotation of the crystal lattice to minimize the strain of the system. As this effect does not have a preferred rotational direction, one would normally observe elongated diffraction spots from such small angles of rotation. The change in angle to reach $\bar{M}$ could be due to non uniformities in the deposition process, in addition to the slight crystal rotation which effectively raises the $\bar{M}$-point in k_y. It is also noticed that only four lattice points are visible after deposition, further supporting that the deposited overlayer is not of good enough quality. Lacroix *et al.* [66] state that orbital degrees of freedom boost the tendency to form disordered states or even valence-bond phases. As the f-orbitals have a high degree of freedom it is probable that to minimize the frustration in the system, the dysprosium sulfide stabilises with a similar crystal structure upon deposition of a few monolayers. Yet there is still the probability that most of the acquired image originates from electrons scattered from the underlying MoS_2 and is just screened by the overlying dysprosium compound.

Chapter 6

Discussion

SECTION 6.1 Surface Growth

As no microscopy or real space probing has been done to charatcerize the growth of dysprosium on the surface, it is difficult to conclude whether or not the overlayer is of good quality or if the dysprosium clusters on the surface (Volmer-Weber). Still, the fact that for sufficiently thin overlayers LEED patterns are observed, supports that a Stranski-Krastanov growth mode is more likely. The LEED pattern becomes more clear after annealing the sample, which has been suggested to be a result from surface reconstruction. The fact that ARPES measurements are able to reveal band structure after deposition is also a clear indiaction that the overlayer has some crystalline quality. One has to note that the LEED pattern after deposition does only exhibit 4 spots oriented in such a way that seems likely to be of HCP structure. Still, optimization of the growth process should be done to find the optimal conditions for the dysprosium compound to show a full LEED pattern.

In addition, the ARXPS data both from the thin and thick deposited film thicknesses exhibit traits of steadily decreasing signals for higher sample angles. If indeed a Volmer-Weber mode was the case, it should have been reflected in this data as a more irregular intensity change at different angles. Still, the deviations at certain angles also indicate a non uniform surface, but if that is due to the deposited overlayer or if one is probing a part of the sample surface with flaking, is uncertain. One should also be careful to make these assumptions from this data, as the signal in the ARXPS data also depends on many other variables in the system.

SECTION 6.2 Chemical Reaction and Stoichiometry

There is indeed an interesting chemical reaction occuring upon the deposition of dysprosium on the molybdenum disulphide. Similar to previous experiments, the core levels of both sulphur and molybdenum exhibit shifts in peak binding energy after the deposition of dysprosium. These are clear indiactors of the samples' reaction to change in the chemical environment. As for the shift observed for the Dy5p core level of around 1.7 eV after annealing from referenced bulk binding energy, it is believed to be too large for a possible doping shift and is regarded as a shift due to bonding between the dysprosium and sulphur. The binding energy shift of Dy5p of around 1eV due to the annealing process is an interesting trait as it further supports the claim of a changing chemical composition of the dysprosium.

In the temperature series, there is quite a difference between the total measured intensities of the S2p core level. On the sample with a few monolayers of Dy, the Sulphur intensity increases by roughly a factor 2 over the whole range whilst in the case of the film of thickness between 2-3 nm, the intensity increase by almost a factor of 250. Intuitively, as the amount of dysprosium increases, it also requires increased amount of sulphur to undergo this reaction. Thus, such observations are to be expected. In the case of the thicker film, the S2p component from the Mo-S configuration is not observed as the deposited overlayer screens out the molybdenum signal. On the thinner film one can observe this signal and in figure 5.5 and 5.6, the line shape of the S2p signal of the Dy-S suddenly changes around 150°C. At the same time, the left shoulder becomes more apparent and the intensity drops above this temperature. As stated earlier this could be a sign of dysprosium intercalating in the MoS_2 structure.

Martín-Concepción *et al.* [67] state that the ARXPS technique is very much dependent of the surface roughness as well as the thin film morphology. To reliably determine the accurate layered stoichiometry of nanometre thin films, one need to know about the surface roughness and the distribution of islands (if any). Without this, the uncertainty is very large. Still, van der Waals materials like MoS_2 are known to make smooth surfaces, thus it is unlikely to be rough after cleaving. While the measurements in Århus on a thin film suggest a sulphur rich surface, the measurement of a thicker film reveals a more even distribution of the dysprosium and sulphur. From this, one should be careful to conclude with an exact stoichiometric relation. On the film with 2-3 monolayers of dysprosium, a LEED pattern was observed with seemingly hexagonal symmetry. This is hypothesized to arise from one of three reactions: Dysprosium intercalation will increase the quality of the LEED pattern from the underlying MoS_2. This does not, however, explain the irregular increase of the sulphur core level. Reevaporation of Dy, however unlikely, will have a similar effect on the observed signal. The last solution is the formation of a dysprosium compound of hexagonal crystal symmetry as a result of reconstruction. Theoretical calculations could reveal which stochiometric relation for the dysprosium sulphide that favours such a crystal structure.

When introducing one reacted and one unreacted dysprosium film, interesting chemistry is observed. The thickest film clearly exhibits traits similar to that observed for Dy_2O_3, as previously mentioned. This proves to be a possible way of synthesizing dysprosium oxide thin film for potential use in spintronics by taking advantage of the compound's effects as a magnetic insulator. Still, the quality of the film has to be asessed before proper device applications can be discussed. As for the thinner film that had been annealed before being exposed to an oxygen environment, a totally different reaction seems to take place. After oxidation, two O1s components are observed, but this is reduced to a single component after annealing the sample to 300°C. This, in combination with observing a shift in the Dy4d orbital towards lower E_B, and the appearance of a second set of peaks in the S2p region, might suggest the formation of a dysprosium oxide sulphide. There are still two components in the S2p region, but one is slightly shifted. This indicates a reaction, but still the component belonging to the dysprosium sulphide is quite prominent, suggesting maybe higher temperatures are needed for it to fully react. The valence band shown for these different compounds further supports that these two have very different electronic properties. The dysprosium oxide clearly shows what seems to be insulating behaviour with a band edge below 2 eV, while the oxide sulphide indicates more of a semiconducting nature.

SECTION 6.3 Electronic Structure Change

The observed decrease in the ARPES measurements of the VBM at $\bar{M}$ of 130meV is of such size that it is regarded as a real energy shift. Due to the uncertain nature of the deposited overlayer, it is difficult to say whether this is the effect of introducing a magnetic field in the sample originating from the dysprosium sulphide, or from the general interactions between the electronic structure of the two materials. If the observed change in band structure arises from magnetic effects, it would be interesting to observe how this changes with an external magnetic field. As the LEED patterns before and after deposition of dysprosium show little to no change in the size of the crystal lattice, the observed diffraction spots most probably originate from the underlying MoS_2 structure. Still, the fact that before the sample was annealed no pattern was observed, indicates restructuring of the deposited overlayer. Thus a more thorough study can be done to determine the possibility of achieving overlayers of better crystalline quality.

Also, the observed difference in the valence band edges when exposing two different dysprosium films to oxygen is very interesting, as it suggests the formation of compounds with possibly different properties. How the dysprosium oxide film affects the MoS_2-substrate might be interesting, as calculations on for example europium oxide (EuO) proving its possible applications in future spin processing techniques have been shown [3]. This compound might also be worth further investigation for the field of magnetic insulators. The oxide sulphide formation of dysprosium and of other rare earths are not widely researched, but for example lanthanum oxide sulphide activated with Nb, Er, Tm and Yb are highly

effective anti-Stokes phosphors which have been suggested for use in low-threshold microlasers and unified light diodes.

SECTION 6.4 Model Improvements

Modeling of these complex systems demands several approximations. XPS signals are said to be the convolution of a Gaussian and Lorentzian contribution. Still, this convolution can not be solved analytically, meaning a numerical solution has to be found. To decrease the computational time an approximation of the true Voigt function, the pseudo-Voigt has been used. As long as the signals exhibit symmetric relations this is usually a quite good approximation. As for the complexity of the Dy4d orbital, the asymmetric pseudo-Voigt presented by Schmid *et al.* [68] might improve the data analysis. The choice of background has also been questioned as revisions and comparative studies of the shirley background has weakened its position [69, 70, 71]. In these cases the Tougaard method is described as the superior choice for quantification purposes.

As for the quantification through ARXPS, the choice of attenuation length, and layer thickness in the model is questioned. For dysprosium, approximating λ_{Dy} includes a high degree of uncertainty, as the nature of the resulting compound is unknown. For the same reason, the choice of x_{layer} will give a wide variation in the modelled stoichiometry. Calculating the possible crystal structures of the various compounds will prove useful, as it can give a more reasonable choice of the layer thickness when modeling.

Chapter 7

Conclusion

SECTION 7.1 Concluding Remarks

This thesis has focused on the study of chemical reactions upon deposition of dysprosium on a molybdenum disulphide substrate. The results indicate that for sufficiently thin films (2-4 monolayers), the proposed Dy_xS_y overlayer is of quite good quality and a surface reconstruction is proposed to occur when annealing the sample at $300^{\circ}\mathrm{C}$. Interesting observations were made about how the compound affects the substrate and its electronic structure. The presence of this compound along with dysprosium's strong magnetic properties seems to influence the spin-coupled environment in the underlying MoS_2. Thus, could potentially allow for spin manipulation in the system. Another exciting trait is the new compound itself, which seemingly is not the sesquisulfide. It is interesting if this can extend the library of chalcogenide materials for electronic applications. As rare earth elements forming chalcogenides can display a variety of physical properties due to mixed valence effects [54], it can also have potential applications in thermoelectric materials, magneto-optical materials and even spintronics, suggesting that this compound is worth further investigation.

The measurements carried out by the means of XPS, LEED and ARPES in the XPS laboratory show promising indication that the dysprosium sulphide grows fairly smooth on the substrate. A reappearance of a LEED pattern with hexagonal symmetry is regarded as evidence of sample reconstruction, but it is uncertain whether it originates from the substrate or if some of the diffraction pattern is from the overlayer structure. Some signs of intercalation are also seen in the measurements, but are less prominent. Probing the band structure by ARPES showed some fascinating changes. The addition of dysprosium and the resulting chemical reaction resulted in a decrease of the VBM at the $\bar{M}$-point by 130meV and the splitting in the negative parabolic band to disappear. The observations

were proposed to be the effect of either two bandstructures superimposed on top of each other, or the magnetic interaction with the underlying MoS_2 structure.

Additionally, the results from oxidizing the dysprosium thin films proved that the chemical reaction occuring is strongly dependent on whether the deposited overlayer has been annealed prior to the introduction of oxygen. On an unreacted Dy film of 2-3 nm, the results support the formation of a dysprosium oxide which is further reacted by subsequent annealing of 150°C and 300°C. Such a thin film of magnetic oxide might show exciting applications in the field of magnetic insulators, and the way it affects the MoS_2 could also prove to yield interesting effects on the spin-polarization in the band structure. By exposing an even thinner film of 2-4 monolayers, which had been previously annealed, to oxygen, a different reaction is observed. This is suggest to be the formation of a dysprosium oxide sulphide with possible applications in the technology of phosphors.

SECTION 7.2 Potential Directions

Through the work in this thesis, further understanding of the chemical and physical interactions between molybdenum disulphide and dysprosium has been achieved. Still, several questions remains. From a theoretic point of view it might be interesting to investigate the possibilities and physical properties of dysprosium sulphides by, for example, density functional theory (DFT). Theoretical studies might also prove useful to determine the chemical composition of the created compounds and the applications for the different possible compounds.

Experimentally it would be interesting to learn more about the growth of the deposited overlayer and to see if the crystalline quality can be enhanced, and even if epitaxially grown layers is possible. As the deposited overlayer needs to be quite thin, reflection high-energy electron diffraction (RHEED) will give valuable information about the crystal structure with lower probability of observing a superimposed structure. Microscopic techniques such as AFM, STM and SEM will provide helpful information through real space proping of the sample. If the dysprosium favours growth around surface defects, this will be revealed, thus proving that a surface of higher quality is needed. To further help determine the stochiometric relation of the dysprosium-sulphur compound, the samples can be investigated by the means of secondary ion mass spectrometry.

In addition to this it is proposed to further study the band structures by ARPES. This can be done both to learn more about the dysprosium sulphide, but one can also investigate the interplay between the molybdenum disulphide and dysprosium oxide thin film in addition to the oxide sulphide. To increase the quality of these measurements these experiments should be conducted at a synchrotron facility for higher energy resolution. The measurements could also be done with the sample cooled to decrease the amount of band broadening.

Bibliography

[1] H.C. Aspinall. *Chemistry of the f-Block Elements*. Advanced chemistry texts. Taylor & Francis, 2001. ISBN 9789056993337.

[2] J A Aitken, J A Cowen, and M G Kanatzidis. Metamagnetic transition in $EuSe_2$: A new, metastable binary rare-earth polychalcogenide. *Chem. Mater.*, 10(12):3928–3935, 1998. ISSN 0897-4756.

[3] H. X. Yang, A. Hallal, D. Terrade, X. Waintal, S. Roche, and M. Chshiev. Proximity effects induced in graphene by magnetic insulators: First-principles calculations on spin filtering and exchange-splitting gaps. *Physical Review Letters*, 110(4):1–5, 2013. ISSN 00319007. doi: 10.1103/PhysRevLett.110.046603.

[4] Stefan Wachter, Dmitry K. Polyushkin, Ole Bethge, and Thomas Mueller. A microprocessor based on a two-dimensional semiconductor. *Nature Communications*, 8: 14948, 2017. ISSN 2041-1723. doi: 10.1038/ncomms14948.

[5] Timothy E. Kidd, Aaron O'Shea, Zach Griffith, Stroh Leslie, Paul M. Shand, Kayla R. Boyle, and Laura H. Strauss. Synthesis of magnetic 1D dichalcogenide nanostructures. *Journal of Nanoparticle Research*, 14(6):1–10, 2012. ISSN 13880764. doi: 10.1007/s11051-012-0903-8.

[6] L. J. Li, X. D. Zhu, Y. P. Sun, H. C. Lei, B. S. Wang, S. B. Zhang, X. B. Zhu, Z. R. Yang, and W. H. Song. Superconductivity of Ni-doping 2H-TaS_2. *Physica C: Superconductivity and its Applications*, 470(5-6):313–317, 2010. ISSN 09214534. doi: 10.1016/j.physc.2010.01.042.

[7] I. Song, C. Park, and H. C Choi. Synthesis and properties of molybdenum disulphide: from bulk to atomic layers. *RSC Adv.*, 5(10):7495–7514, 2015. ISSN 2046-2069. doi: 10.1039/C4RA11852A.

[8] J. Vinje. Photochemistry of a Nucleobase Relevant to the Formation of Malignant Melanoma. (June), 2016.

[9] K. W. Hunvik. A Spectroscopic Study of in situ Magnetic Doping of Novel Layered Materials for Spintronics. (June), 2016.

[10] R. Winkler. *Spin Orbit Coupling Effects in Two-Dimensional Electron and Hole Systems*. 2003. ISBN 3540011870. doi: 10.1007/b13586.

[11] A. Manchon, H. C. Koo, J. Nitta, S. M. Frolov, and R. A. Duine. New perspectives for Rashba spin–orbit coupling. *Nature Materials*, 14(9):871–882, 2015. ISSN 1476-1122. doi: 10.1038/nmat4360.

[12] Mathias Gehlmann, Gustav Bihlmayer, Irene Aguilera, Ewa Mlynczak, Markus Eschbach, Sven Döring, Pika Gospodaric, Stefan Cramm, Beata Kardynal, Lukasz Plucinski, Stefan Blügel, and Claus M. Schneider. Quasi 2D electronic states with high spin-polarization in centrosymmetric MoS_2 bulk crystals. *arXiv preprint*, (June 2015):arXiv:1510.04101, 2015. ISSN 20452322. doi: 10.1038/srep26197.

[13] Home Search, Collections Journals, About Contact, My Iopscience, I P Address, J A Venables, G D T Spiller, and M Hanbucken. Nucleation and growth of thin films. *Reports on Progress in Physics*, 47(4):399, 1984. ISSN 0034-4885. doi: 10.1088/0034-4885/47/4/002.

[14] R. Schöllhorn. Intercalation chemistry. *Physica B+C*, 99(1-4):89–99, 1980. ISSN 03784363. doi: 10.1016/0378-4363(80)90215-6.

[15] Linxiao Geng, Guocheng Lv, Xuebing Xing, and Juchen Guo. Reversible Electrochemical Intercalation of Aluminum in Mo_6S_8. *Chemistry of Materials*, 27(14): 4926–4929, 2015. ISSN 15205002. doi: 10.1021/acs.chemmater.5b01918.

[16] Nele Isabell Schwarzburger, Robert Knobel, Harald Behrens, Michael Binnewies, Ingo Horn, Andreas Pelster, Heinrich F. Arlinghaus, Lars Dörrer, and Harald Schmidt. Kinetics of Lithium Intercalation in Titanium Disulfide Single Crystals. *Zeitschrift für Physikalische Chemie*, 226(5-6):461–489, 2012. ISSN 0942-9352. doi: 10.1524/zpch.2012.0227.

[17] Ramzy Daou, Hidefumi Takahashi, Sylvie Hébert, Marine Beaumale, Emmanuel Guilmeau, and Antoine Maignan. Intrinsic effects of substitution and intercalation on thermal transport in two-dimensional TiS_2 single crystals. *Journal of Applied Physics*, 117(16):165101, 2015. ISSN 0021-8979. doi: 10.1063/1.4919078.

[18] Tetsuya Kajita, Takayuki Kawamata, Takashi Noji, Takehiro Hatakeda, Masatsune Kato, Yoji Koike, and Takashi Itoh. Electrochemical Na-intercalation-induced high-temperature superconductivity in FeSe. *Physica C: Superconductivity and its Applications*, 519:104–107, 2015. ISSN 09214534. doi: 10.1016/j.physc.2015.09.005.

[19] J. Matthews. *Epitaxial Growth*. Number poeng 1. Elsevier Science, 2012. ISBN 9780323152129.

[20] I. Chorkendorff and J.W. Niemantsverdriet. *Concepts of Modern Catalysis and Kinetics*. Wiley, 2006. ISBN 9783527605644.

[21] Michael Quirk and Julian Serda. *Semiconductor manufacturing technology*. Prentice Hall, USA, 1 edition, 2001.

[22] Nagamitsu Yoshimura. *Vacuum technology: Practice for scientific instruments*. Springer, Tokyo, 2008. ISBN 9783540744320. doi: 10.1007/978-3-540-74433-7.

[23] S. Hüfner. *Photoelectron Spectroscopy Springer-Verlag Berlin Heidelberg GmbH*. 2003. ISBN 9783642075209.

[24] F. Mazzola. *Photoemission spectroscopies and their application in solid state and material physics*, volume 2. 2016. ISBN 9788232615322.

[25] S. P. Cooil. Controlling the Epitaxial Growth of Graphene On Diamond Surfaces. 2014.

[26] D. Coster and R. De L. Kronig. New type of auger effect and its influence on the x-ray spectrum. *Physica*, 2:13–24, 1935. ISSN 00318914. doi: 10.1016/S0031-8914(35)90060-X.

[27] J. F. Watts and J. Wolstenholme. *An Introduction to Surface Analysis by XPS and AES*. John Wiley & Sons Ltd., 2003. ISBN 0470847123.

[28] F. Song, Å. F. Monsen, Z. S. Li, J. W. Wells, and E. Wahlström. The layer-by-layer stoichiometry of $La_{0.7}Sr_{0.3}MnO_3/SrTiO_3$ thin films and interfaces. *Surface and Interface Analysis*, 45(7):1144–1147, 2013. ISSN 01422421. doi: 10.1002/sia.5240.

[29] R. Hesse, T. Chassé, and R. Szargan. Peak shape analysis of core level photoelectron spectra using UNIFIT for WINDOWS. *Fresenius' Journal of Analytical Chemistry*, 365:48–54, 1999. ISSN 0937-0633. doi: 10.1007/s002160051443.

[30] P. Thompson, D. E. Cox, and J. B. Hastings. Rietveld Refinement of Debye-Scherrer Synchrotron X-ray Data from Al_2O_3. *Journal of Applied Crystallography*, 20(2):79–83, 1987. ISSN 00218898. doi: 10.1107/S0021889887087090.

[31] János Végh. The analytical form of the Shirley-type background. *Journal of Electron Spectroscopy and Related Phenomena*, 46(2):411–417, 1988. ISSN 03682048. doi: 10.1016/0368-2048(88)85038-2.

[32] A. K. Livesey and G. C. Smith. The determination of depth profiles from angle-dependent XPS using maximum entropy data analysis. *Journal of Electron Spectroscopy and Related Phenomena*, 67(3):439–461, 1994. ISSN 03682048. doi: 10.1016/0368-2048(93)02035-K.

[33] Justin W. Wells and Keith Birkinshaw. A matrix approach to resolution enhancement of XPS spectra by a modified maximum entropy method. *Journal of Electron Spectroscopy and Related Phenomena*, 152(1-2):37–43, 2006. ISSN 03682048. doi: 10.1016/j.elspec.2006.03.003.

[34] J E Shore. Relative Entropy, Probabilistic Inference, and AI. *Uncertainty in Artificial Intelligence*, (4):211–215, 1986.

[35] Karmeshu, editor. *Entropy Measures, Maximum Entropy Principle and Emerging Applications*. Studies in Fuzziness and Soft Computing. Springer Berlin Heidelberg, 2012. ISBN 9783540362128.

[36] J. J. Yeh. *Atomic Calculation of Photoionization Cross-Sections and Asymmetry Parameters*. Gordon and Breach Science Publishers, Langhorne, PE (USA), 1993.

[37] J. J. Yeh and I. Lindau. Atomic Data and Nuclear Data Tables. 32:1–155, 1985.

[38] P. Hofmann. *Surface Physics: An Introduction*. Number 1.3. Philip Hofmann, 2014. ISBN 9788799609000.

[39] P. Willmatt. *An Introduction to Synchrotron Radiation*. John Wiley & Sons Ltd., 2011. ISBN 9780470745793.

[40] P. Kapadia. *Synchrotron Radiation*, volume 36. 2004. ISBN 978-3-642-55314-1. doi: 10.1016/j.optlastec.2004.02.010.

[41] L. Zommer. Determination of the spectrometer transmission function for XPS quantitative analysis. *Vacuum*, 46(5-6):617–620, 1995. ISSN 0042207X. doi: 10.1016/0042-207X(94)00143-X.

[42] K. Richter and B. Peplinski. Determination of Relative Transmission Function of Two Scanning Modes of an Electrostatic Hemispherical Analyser with a Lens System. *Surface and Interface Analysis*, 2(4):161–163, 1980. ISSN 01422421.

[43] W.P. Gwyn. Electron Binding Energies. In *X-Ray Data Booklet*, chapter 1.1. Lawrence Berkeley National Laboratory, 2 edition, 2001.

[44] M. Sreemany, T. B. Ghosh, B. C. Pai, and M. Chakraborty. XPS Studies on the Oxidation Behavior of SiC Particles. *Materials Research Bulletin*, 33(2):189–198, 1998. ISSN 0025-5408. doi: 10.1016/S0025-5408(97)00222-5.

[45] B. Lanfant, Y. Leconte, G. Bonnefont, V. Garnier, Y. Jorand, S. Le Gallet, M. Pinault, N. Herlin-Boime, F. Bernard, and G. Fantozzi. Effects of carbon and oxygen on the spark plasma sintering additive-free densification and on the mechanical properties of nanostructured SiC ceramics. *Journal of the European Ceramic Society*, 35(13): 3369–3379, 2015. ISSN 1873619X. doi: 10.1016/j.jeurceramsoc.2015.05.014.

[46] National Institute of Standards and Technology. NIST Standard Reference Database 82, 2010.

[47] Yves Baer, Per Filip Hedén, Jan Hedman, Martin Klasson, and Carl Nordling. Determination of the electron escape depth in gold by means of ESCA. *Solid State Communications*, 8(18):1479–1481, 1970. ISSN 00381098. doi: 10.1016/0038-1098(70)90724-6.

[48] M. Klasson, J. Hedman, A. Berndtsson, R. Nilsson, C. Nordling, and P. Melnik. Escape Depths of X-ray Excited Electrons. *Physica Scripta*, 5(1-2):93–95, 1972. ISSN 0031-8949. doi: 10.1088/0031-8949/5/1-2/015.

[49] R. Nyholm, N. Mårtensson, a. Lebugle, and U. Axelsson. Auger and Coster-Kronig broadening effects in the 2p and 3p photoelectron spectra from the metals 22Ti-30Zn. *Journal of Physics F: Metal Physics*, 11:1727, 1981. ISSN 0305-4608. doi: 10.1088/0305-4608/11/8/025.

[50] J.F. Moulder, W.F. Stickle, P.E. Sobol, and K.D. Bomben. *Handbook of X Ray Photoelectron Spectroscopy: A Reference Book of Standard Spectra for Identification and Interpretation of Xps Data*. Physical Electronics, Minnesota, 1995.

[51] Unidad Querétaro and Alberto Herrera-gomez. The Peak-Shirley Background. 2012.

[52] S. P. Cooil, F. Song, G. T. Williams, O. R. Roberts, D. P. Langstaff, B. Jørgensen, K. Høydalsvik, D. W. Breiby, E. Wahlström, D. A. Evans, and J. W. Wells. Iron-mediated growth of epitaxial graphene on SiC and diamond. *Carbon*, 50(14):5099–5105, 2012. ISSN 00086223. doi: 10.1016/j.carbon.2012.06.050.

[53] F. K. Tutu, J. Wu, P. Lam, M. Tang, N. Miyashita, Y. Okada, J. Wilson, R. Allison, and H. Liu. Antimony mediated growth of high-density InAs quantum dots for photovoltaic cells. *Applied Physics Letters*, 103(4), 2013. ISSN 00036951. doi: 10.1063/1.4816503.

[54] Mirtat Bouroushian. Electrochemistry of Metal Chalcogenides. *Monographs in electrochemistry*, 2010. ISSN 0002-7863. doi: 10.1007/978-3-642-03967-6.

[55] Haibin YUAN, Jianhui ZHANG, Ruijin YU, and Qiang SU. Synthesis of rare earth sulfides and their UV-vis absorption spectra. *Journal of Rare Earths*, 27(2):308–311, 2009. ISSN 10020721. doi: 10.1016/S1002-0721(08)60239-2.

[56] J. R. Henderson, M. Muramoto, E. Loh, and John B. Gruber. Electronic Structure of Rare-Earth Sesquisulfide Crystals. *The Journal of Chemical Physics*, 47(9):3347–3356, 1967. ISSN 0021-9606. doi: 10.1063/1.1712397.

[57] D. Kienzle, P. Koirala, and L. D. Marks. Lanthanum aluminate (110) 3 x 1 surface reconstruction. *Surface Science*, 633:60–67, 2015. ISSN 00396028. doi: 10.1016/j.susc.2014.11.016.

[58] Gang Chen, Jun Wan, Jianshu Yang, Xunming Ding, Ling Ye, and Xun Wang. Surface structures of erbium silicide ultra-thin films formed by solid phase epitaxy on Si(100). *Surf. Sci.*, 513:203–210, 2002. ISSN 00396028. doi: 10.1016/S0039-6028(02)01705-3.

[59] Stian Ruud Schikora. A Spectroscopic Study of Dysprosium Doping for Energy Band Splitting in MoS_2. Technical report, NTNU - Department of Physics, Trondheim, 2016.

[60] O. Madelung, U. Rössler, and M. Schulz, editors. *Dy_2S_3: crystal structure, physical properties*, pages 1–16. Springer Berlin Heidelberg, Berlin, Heidelberg, 2000. ISBN 978-3-540-31361-8. doi: 10.1007/10681735_621.

[61] Davide Barreca, Alberto Gasparotto, Andrian Milanov, Eugenio Tondello, Anjana Devi, and Roland A. Fischer. Nanostructured Dy_2O_3 films: An XPS Investigation. *Surface Science Spectra*, 14(1):52–59, 2007. ISSN 1055-5269. doi: 10.1116/11.20080702.

[62] Sanghun Jeon and Hyunsang Hwang. Effect of hygroscopic nature on the electrical characteristics of lanthanide oxides (Pr_2O_3, Sm_2O_3, Gd_2O_3, and Dy_2O_3). *Journal of Applied Physics*, 93(10 1):6393–6395, 2003. ISSN 00218979. doi: 10.1063/1.1569028.

[63] H. S. Craft, R. Collazo, Z. Sitar, and J. P. Maria. Molecular beam epitaxy of Sm_2O_3, Dy_2O_3, and Ho_2O_3 on Si (111). *Journal of Vacuum Science & Technology B: Microelectronics and Nanometer Structures*, 24(4):2105, 2006. ISSN 10711023. doi: 10.1116/1.2216721.

[64] Yu L Suponitskii, G M Kuz'micheva, and Andrei A Eliseev. Lanthanide Oxide Sulphides. *Russian Chemical Reviews*, 57(3):209–220, 1988. ISSN 14684837. doi: 10.1070/RC1988v057n03ABEH003345.

[65] A. A. Shashkin, Maryam Rahimi, S Anissimova, S V Kravchenko, V T Dolgopolov, and T M Klapwijk. Spin-independent origin of the strongly enhanced effective mass in a dilute 2D electron system. *Physical review letters*, 91(4):046403, 2003. ISSN 0031-9007. doi: 10.1103/PhysRevLett.91.046403.

[66] Claudine Lacroix, Philippe Mendels, and Frédéric Mila, editors. *Introduction to Frustrated Magnetism*, volume 164. Springer, 2011. ISBN 978-3-642-10588-3. doi: 10.1007/978-3-642-10589-0.

[67] A. I. Martín-Concepción, F. Yubero, J. P. Espinós, and S. Tougaard. Surface roughness and island formation effects in ARXPS quantification. *Surface and Interface Analysis*, 36(8):788–792, 2004. ISSN 01422421. doi: 10.1002/sia.1765.

[68] Martin Schmid, Hans Peter Steinrück, and J. Michael Gottfried. A new asymmetric Pseudo-Voigt function for more efficient fitting of XPS lines. *Surface and Interface Analysis*, 46(8):505–511, 2014. ISSN 10969918. doi: 10.1002/sia.5521.

[69] János Végh. The Shirley background revised. *Journal of Electron Spectroscopy and Related Phenomena*, 151(3):159–164, 2006. ISSN 03682048. doi: 10.1016/j.elspec.2005.12.002.

[70] R. Hesse, M. Weiß, R. Szargan, P. Streubel, and R. Denecke. Improved peak-fit procedure for XPS measurements of inhomogeneous samples - Development of the advanced Tougaard background method. *Journal of Electron Spectroscopy and Related Phenomena*, 205:29–51, 2015. ISSN 03682048. doi: 10.1016/j.elspec.2015.06.013.

[71] R. Hesse, M. Weiß, R. Szargan, P. Streubel, and R. Denecke. Comparative study of the modelling of the spectral background of photoelectron spectra with the Shirley and improved Tougaard methods. *Journal of Electron Spectroscopy and Related Phenomena*, 186(1):44–53, 2013. ISSN 03682048. doi: 10.1016/j.elspec.2013.01.020.

Appendix A

MATLINE XPS scan parameters

Table A.1: Relevant scan parameters from XPS measurements at MATLINE. E_p is the pass energy, ΔE the energy step and $h\nu$ the photon energy.

Region	E_p [eV]	$h\nu$ $[eV]$	Dwell time [s]	ΔE [eV]
Mo3d	20	400	0.5	0.05
S2p	20	230	0.5	0.05
Dy4d	20	450	0.5	0.2
C1s	20	370	0.5	0.05
O1s	75	610	0.5	0.1

Appendix B

Core level temperature dependence

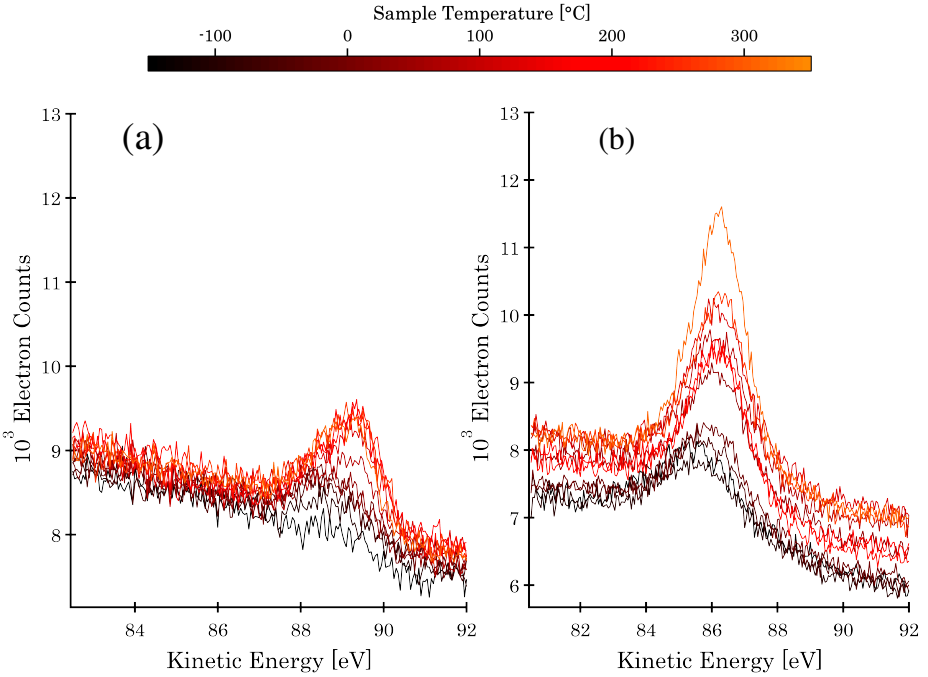

Figure B.1: Temperature dependence of C1s on a sample with a dysprosium overlayer thickness of: **(a)** ∼3 nm, and **(b)** 2-3 monolayers.

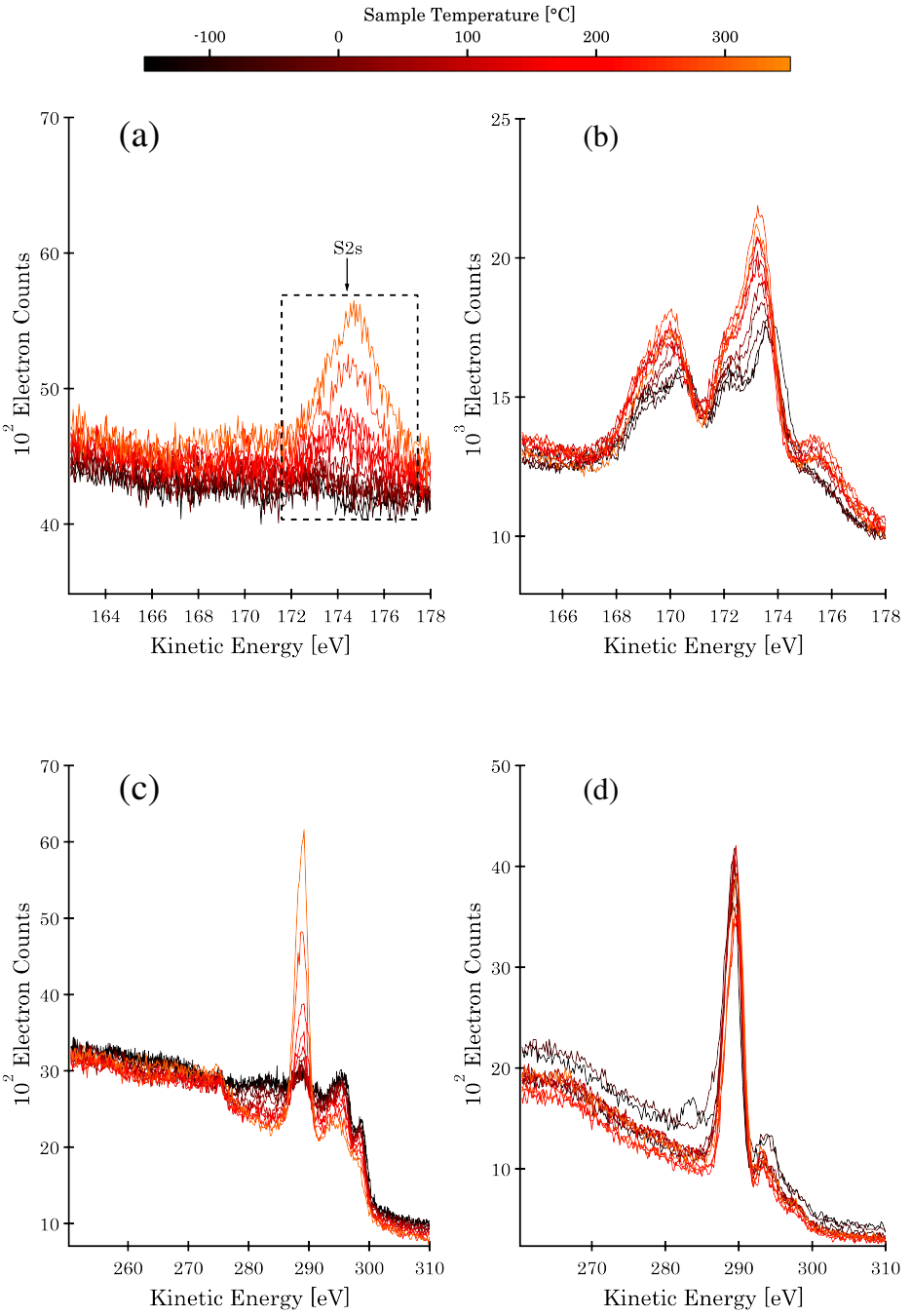

Figure B.2: Temperature dependence of Mo3d, **(a)** & **(b)**, and Dy4d, **(c)** & **(d)**. The figures on left are from a sample with ∼3 nm overlayer Dy. The right side corresponds to a sample with a thickness of 2-3 monolayers.

Appendix C

Synchrotron ARXPS propagation models

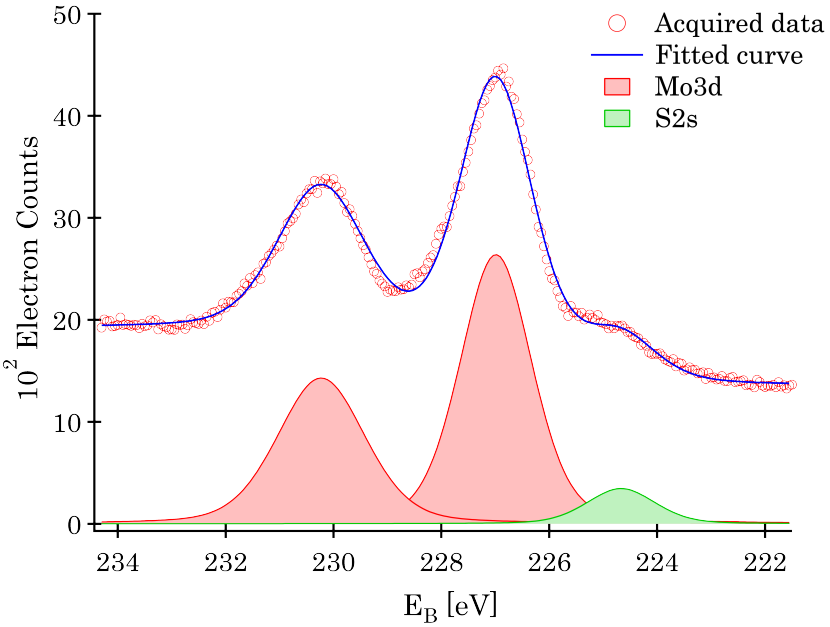

Figure C.1: Model developed for the Mo3d spectrum to be propagated through the core levels measured at emission angles from -5° to 65° with angle steps of 5 degrees.

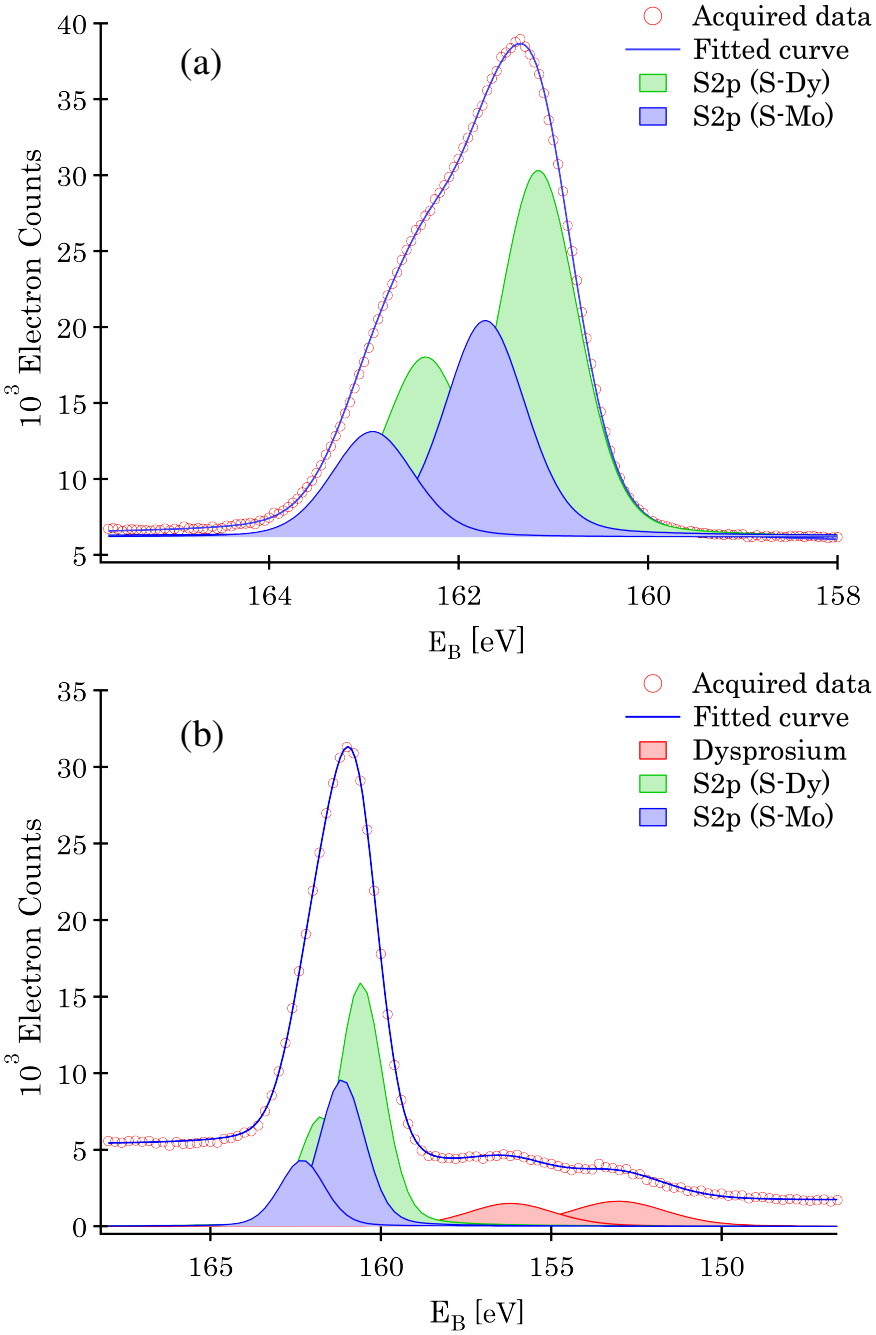

Figure C.2: Models developed for the S2p **(a)** and Dy4d **(b)** spectra to be propagated through the core levels measured at emission angles from -5° to 65° with angle steps of 5 degrees.

Appendix D

NTNU XPS scan parameters

Table D.1: Relevant scan parameters from XPS measurements at NTNU. E_p is the pass energy, ΔE the energy step. All scans were done in fixed analyser transmission mode.

Region	E_p [eV]	Dwell time [s]	ΔE [eV]
Widescan	100	0.5	1
Mo3d	40	0.5	0.1
S2p	40	0.5	0.1
Dy4d	40	0.5	0.1
Dy5p	40	0.5	0.1

Appendix E

NTNU ARXPS propagation models

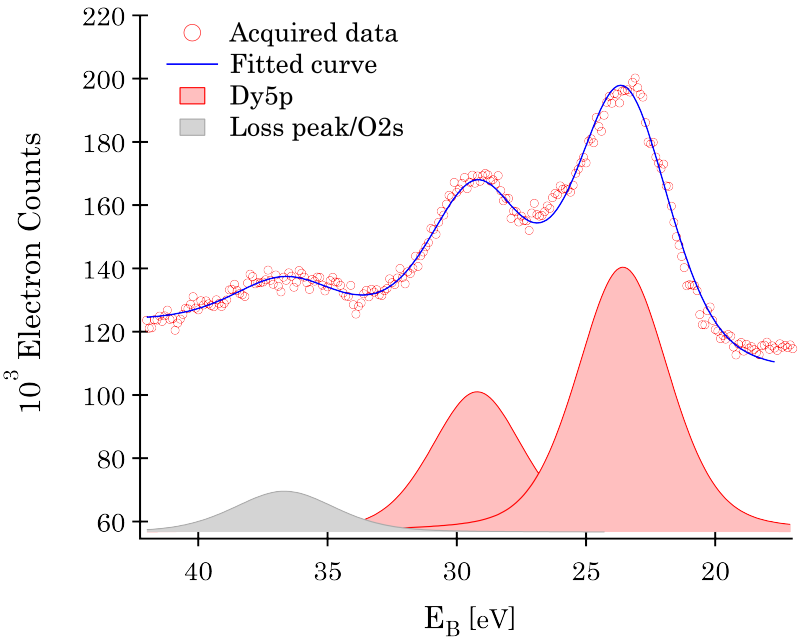

Figure E.1: Model developed for the Dy5p spectrum to be propagated through the core levels measured at emission angles from -5° to 65° with angle steps of 5 degrees.

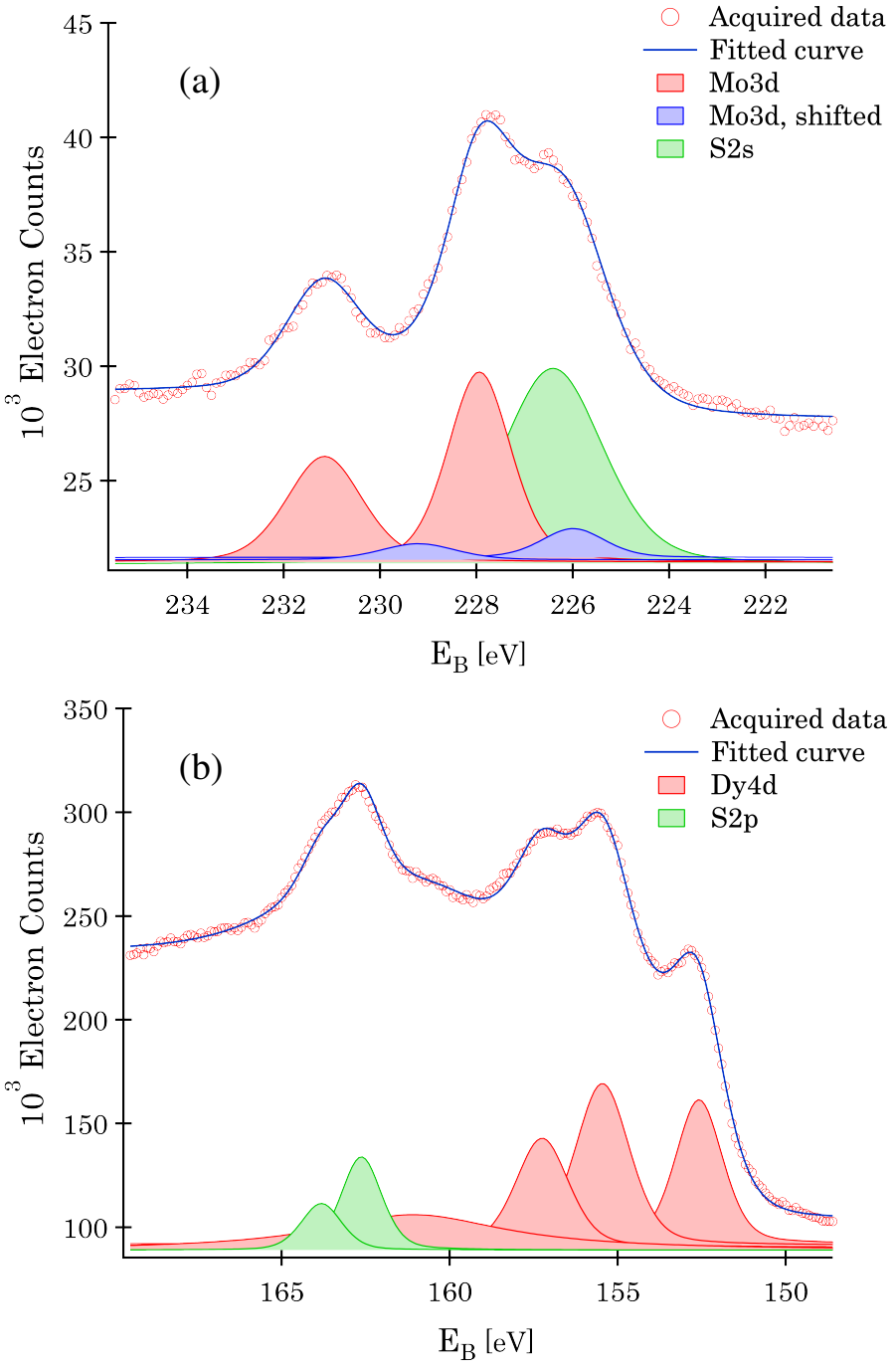

Figure E.2: Models developed for the Mo3d **(a)** and S2p **(b)** spectra to be propagated through the core levels measured at emission angles from -15° to 70°.